Transverse instability mitigation in hadron synchrotrons using electron lenses

TECHNISCHE
UNIVERSITÄT
DARMSTADT

**Fachbereich Elektrotechnik
und Informationstechnik
Institut für Teilchenbeschleunigung
und Elektromagnetische Felder**

Transverse instability mitigation in hadron synchrotrons using electron lenses
Bedämpfung der transversalen Instabilitäten in Hadron-Synchrotrons mithilfe Elektronenlinsen

Genehmigte Dissertation von Vadim Gubaidulin aus Petropawl/Kasachstan

1. Gutachten: Prof. Dr. Oliver Boine-Frankenheim
2. Gutachten: Dr. Elias Métral

Tag der Einreichung: 18.09.2022
Tag der Prüfung: 30.01.2023
Jahr der Veröffentlichung der Dissertation auf TUprints: 2023

Darmstadt, Technische Universität Darmstadt

Erklärung zur Dissertation gemäß der Promotionsordnung der TU Darmstadt

§ 8 Abs. 1 lit. c PromO
Ich versichere hiermit, dass die elektronische Version meiner Dissertation mit der schriftlichen Version übereinstimmt.

§ 8 Abs. 1 lit. d PromO
Ich versichere hiermit, dass zu einem vorherigen Zeitpunkt noch keine Promotion versucht wurde.

§ 9 Abs. 1 PromO
Ich versichere hiermit, dass die vorliegende Dissertation selbstständig und nur unter Verwendung der angegebenen Quellen verfasst wurde.

§ 9 Abs. 2 PromO
Die Arbeit hat bisher noch nicht zu Prüfungszwecken gedient.

Darmstadt, den 18.09.2022

_____

(V. Gubaidulin)

Abstract

High-intensity beams in ring accelerators are subject to several destabilising effects. Among them are transverse beam instabilities that cause severe beam losses. These instabilities are considered at the design stage of any accelerator. One of the ways to suppress the instability is Landau damping. Landau damping is caused by energy exchange between the incoherent and coherent motion of the beam's particles. In this work, a novel way to provide Landau damping is introduced and studied.

A pulsed electron lens produces a betatron tune shift in a hadron bunch as a function of the longitudinal coordinates, which is a longitudinal detuning. An example of transverse detuning is the tune shifts due to octupole magnets. This work considers a pulsed electron lens as a measure to mitigate transverse instabilities.

Using a detailed analytical description with the Vlasov formalism, the coherent properties of the longitudinal and transverse detuning are presented. The analytical predictions are compared with the results of the particle tracking simulations. A pulsed electron lens is demonstrated to be a source of tune spread with two components: the static one, leading to Landau damping; and the dynamic one, leading to effective impedance modification, an effect demonstrated analytically and in the particle tracking simulations. The effective impedance modification can be significant for beam stability due to devices with longitudinal detuning, especially for the nonzero head-tail modes. The Vlasov formalism is extended to include the combination of longitudinal and transverse detuning. As a possible application for SIS100 (Facility for Antiproton and Ion Research in Europe GmbH (FAIR) at GSI Darmstadt, Germany), a combination of a pulsed electron lens with octupole magnets is considered.

Additionally, the results of experiments in the existing ring SIS18 are presented. The feasibility of an electron lens for Landau damping was studied experimentally. It was shown that increasing the current of the electron lens weakens the instability. However, more experiments with a larger range of parameters are necessary to demonstrate the reproducibility of this result. Experiments indicated a potential limiting factor for the usage of electron lenses in SIS18.

Zusammenfassung

Hochstromstrahlen in Ringbeschleunigern sind mehreren destabilisierenden Einflüssen ausgesetzt. Dazu gehören transversale Strahlinstabilitäten, die schwere Strahlverluste verursachen. Eine der Möglichkeiten zur Eindämmung der Instabilität ist die Landau-Dämpfung. Diese Dämpfung erfolgt durch den Energieaustausch zwischen der inkohärenten und der kohärenten Strahldynamik. In dieser Arbeit wird eine neuartige Methode zur Landau-Dämpfung vorgestellt und untersucht.

Eine gepulste Elektronenlinse erzeugt eine Betatron-Frequenzverschiebung in einem Hadronenstrahl als Funktion entlang des Bunches, was ein longitudinales Detuning darstellt. Ein Beispiel für ein transversales Detuning ist die Betatron-Frequenzverschiebung wegen der Oktupol-Magnete. In dieser Arbeit wird eine gepulste Elektronenlinse als Maßnahme zur Bekämpfung von transversalen Instabilitäten betrachtet.

Die kohärenten Eigenschaften des longitudinalen und transversalen Detuning werden mit Verwendung einer detaillierten analytischen Beschreibung, basierend auf dem Vlasov-Formalismus, untersucht. Die analytischen Vorhersagen werden mit den Ergebnissen der Teilchen-Tracking-Simulationen verglichen. Die theoretisch Betrachtungen zeigen, dass eine gepulste Elektronenlinse eine Quelle des Detunings mit zwei Komponenten ist: die statische, die zur Landau-Dämpfung führt; und die dynamische Komponente, die zur Modifikation der effektiven Impedanz führt. Der letztere Effekt wird in Rahmen der Arbeit analytisch und in den Simulationen übereinstimmend nachgewiesen. Die Modifikationen der effektiven Impedanz können für die Wirkung der Geräte mit longitudinalem Detuning von grosser Bedeutung sein.

In Rahmen der Arbeit wurde der Vlasov-Formalismus erweitert, um die Kombination von longitudinalem und transversalem Detuning zu beschreiben. Als eine mögliche Anwendung für SIS100 (FAIR bei GSI Darmstadt, Deutschland), wurde eine Kombination aus einer gepulsten Elektronenlinse mit Oktupol-Magneten untersucht.

Die Ergebnisse der dedizierten Experimente im GSI-Ringbeschleuniger SIS18 wurden vorgestellt. Die Möglichkeit der Nutzung einer Elektronenlinse zur Landau-Dämpfung wurde experimentell untersucht. Es konnte dabei gezeigt werden, dass eine vorher vorhandene Strahlinstabilität nicht mehr auftrat. Weitere Experimente mit geänderten Parametern zur Reproduzierbarkeit dieses Effekts sind noch erforderlich. Experimente hatten eine potenzielle Begrenzbarkeit der Verwendung von Elektronenlinsen im SIS18 angedeutet.

Acknowledgements

Contents

1 Introduction

Particle accelerators play an essential role as an instrument in various fundamental research areas: atomic and nuclear physics, astrophysics, elementary particle physics, plasma physics, biophysics, material science and others. Several significant discoveries were made with the help of particle accelerators. For example, the discovery of Higgs boson at the Large Hadron Collider (LHC) [1], [2] or, most recently, anomalous magnetic moment of the muon [3]–[8] at the Fermi National Accelerator Laboratory, Batavia IL (FNAL). However, the vast majority of particle accelerators are applied in industry and medicine. Industrial applications range from materials processing to environmental protection [9]. In medicine, particle accelerators are employed to produce x-rays, protons, neutrons or heavy ions for radiation treatment of cancer tumours. Two other examples of medical applications are the production of radioisotopes for nuclear medicine and imaging for medical diagnoses [10].

The first charged particle acceleration was performed by a high voltage in the gap between the cathode and the anode. The history of modern particle accelerators began with the inventions of Rolf Wideröe. He conceptualised the betatron, the first circular accelerator, but a working betatron was built only decades after. Then, he built the first linear accelerator [11] based on the design of Gustav Ising [12], using the Radio Frequency (RF) acceleration. Linear accelerator refers to an accelerator design where particles travel along a line and are only accelerated once by a single accelerating section (for example, RF cavities). Circular or ring accelerators all refer to an accelerator design in which particles pass through the same accelerating section many times.

The first breakthrough in the development of circular accelerators was the first cyclotron [13]: in a cyclotron, charged particles circulate in a magnetic field and are repetitively accelerated by the same accelerating section. This results in particles having an outwards-spiralling trajectory. The work on the betatron, which is also a cyclic accelerator, was finalised in [14], [15] by Kerst and Serber. In the betatron, charged particles travel on a trajectory with a constant radius. They are accelerated by the change in the magnetic flux (integral of the magnetic field passing through a surface).

High beam energies are necessary for numerous experimental applications, for example for Compressed barionic matter (CBM) [16], [17] experimental programme at FAIR. High energy beams can either be obtained from a Linear Accelerator (linac) or in a *synchrotron*. The synchrotron utilises the principle of repetitive acceleration by RF cavities and at the same time the particles' orbits are kept constant [18], [19]. This is achieved by increasing the strength of the magnetic field in the bending magnets to account for the increasing energy of the beam. After the discovery of the strong focusing principle [20], the transverse focusing is achieved via dedicated quadrupole magnets. The strong

focusing is achieved by varying focusing and defocusing magnets, resulting in a net focusing effect on the beam. The weak focusing refers to a situation when all magnets focus the beam transversely. Before in the weak focusing machines, the focusing was achieved via the bending magnets. In the transverse plane particles oscillate due to the transverse focusing and in the longitudinal plane they oscillate due to the longitudinal RF potential. This is referred to as betatron and synchrotron oscillations respectively. The number of such oscillations in a single revolution period are named betatron tune and synchrotron tune.

The synchrotrons are used to this day in various accelerator facilities. Other accelerator types have emerged, and new designs and applications are proposed to this day: storage rings [21], colliders [22], [23], Energy Recovery Linacs (ERLs) [24], [25], Free Electron Lasers (FELs) [26], Fixed Field Alternating Gradient accelerators (FFAGs) [27]–[29] and others.

At present, accelerator facilities with several different accelerator types are used to achieve higher target beam parameters (beam intensity, beam energy, luminosity for colliders, brilliance for light sources, for example). For instance, the European Organization for Nuclear Research (CERN) main accelerator chain: the beam is injected from a linac, then it is accelerated in three different synchrotrons (PS booster, Proton Synchrotron (PS) and Super Proton Synchrotron (SPS)) and afterwards, it is injected into the LHC. The purpose of this long accelerator chain is producing high energy proton and heavy ion (only ^{82}Pb) beams.

The FAIR accelerator complex will be discussed in this dissertation. Its accelerators are used to produce a variety of heavy ions, with a focus on high intensity, beam quality and a certain range of available beam energies. In this work, the most important parameter is *beam intensity*, the number of particles in a beam.

1.1 FAIR accelerator complex and its heavy ion synchrotrons

The FAIR accelerator complex is currently under construction at Helmholtzzentrum für Schwerionenforschung GmbH (GSI) in Darmstadt, Germany. The layout of the facility is depicted in Fig. 1.1. This accelerator complex is designed to accelerate ions from protons to uranium with various charge states. The primary ion beams are produced by the accelerator chain consisting of ion sources, Universal Linear Accelerator (UNILAC) [30], Schwerionensynchrotron 18 (ger. for heavy ion synchrotron 18) (SIS18) [31] and Schwerionensynchrotron 100 (ger. for heavy ion synchrotron 100) (SIS100) [32]. Secondary ion beams (rare isotopes) are produced after the UNILAC-SIS18-SIS100 accelerator chain via a collision with a target before the Superconducting Fragment Separator (Super-FRS). The proton beams utilise dedicated Proton Linear Accelerator (p-linac) instead of the UNILAC. Proton beam collisions with the target produce the antiprotons after the extraction from the SIS100.
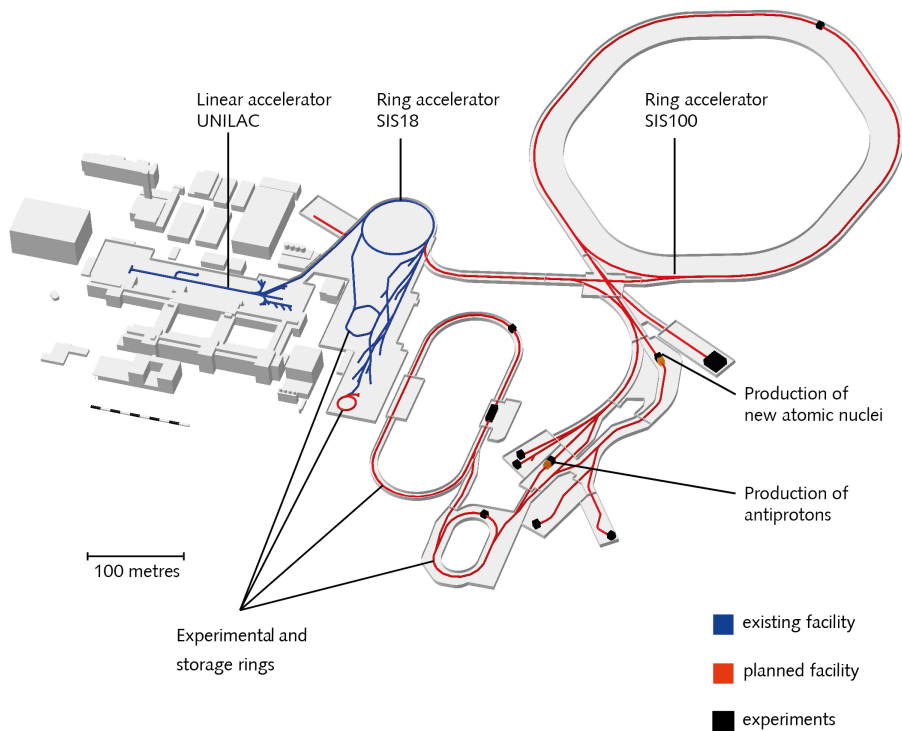
Figure 1.1: FAIR accelerator complex featuring two heavy ion synchrotrons SIS18 and SIS100. The beam is injected from the UNILAC into the booster synchrotron SIS18 with the kinetic energy of 11.4 MeV/nucleon. After the acceleration in the SIS18 the beam is injected into the main FAIR synchrotron SIS100. (Figure from [33])

First, the beam from the ion source is accelerated in the UNILAC. Then, it is injected into the SIS18 and captured by the voltage of the RF cavities into the buckets. An RF bucket is an area where the particles are confined longitudinally and in a specific range of energies. The number of RF buckets depends on the settings of the RF cavities. A collection of particles inside a single RF bucket is called *bunch*. This beam is called a bunched beam (and it can consist of several bunches). In the SIS18, the bunches are further accelerated up to the injection energy of the SIS100. To achieve a higher beam intensity, the bunches injected into the SIS100 are merged and compressed by performing RF manipulations. Secondary beams require high primary beam intensity

because the intensity of the secondary beam is only a fraction of the primary beam intensity (especially rare isotope beams with low production cross-sections). Machine parameters of SIS18 and SIS100 and beam parameters for the reference ion $^{238}\text{U}^{28+}$ are presented in Table 1.1.

Parameter	Units	Symbol	SIS18	SIS100
Intensity	ions/cycle	N_{cycle}	1.5×10^{11}	5×10^{11}
Circumference	m	C	216.72	1083.6
Revolution frequency	kHz	f_{rev}	214	180
Injection energy	MeV/nucleon	E_{inj}	11.4	200
Maximal beam rigidity	T·m	$B\rho$	18	100
RF voltage	kV	V_{RF}	16	58.3
RF harmonic		h_{RF}	4	10
Vertical betatron tune		Q_y	3.47	18.73
Horizontal betatron tune		Q_x	4.27	18.84
Slip factor		η	-0.93	-0.67
Synchrotron tune		Q_{s_0}	7×10^{-3}	4.5×10^{-3}
rms bunch length	m	σ_z	4	13.2
Vertical rms emittance	mm·mrad	ε_y	12.5	3.75
Horizontal rms emittance	mm·mrad	ε_x	37.5	8.75

Table 1.1: Machine parameters and beam parameters of the SIS18 and the SIS100 for the reference ion $^{238}\text{U}^{28+}$ [31], [32], [34], [35]. The parameters are introduced and explained in Chapter 2.

The four pillars of research at FAIR [36] are: 1) CBM program [16], [17], 2) Atomic, Plasma Physics and Applications (APPA) program [37], [38], 3) Nuclear Structure, Astrophysics and Reactions (NUSTAR) program [39], 4) Hadron structure and dynamics program and Antiproton Anihilation at Darmstadt (PANDA) collaboration [40]. The Nuclear Physics European Collaboration Committee (NuPECC) 2017 long-range plan [41] lists the FAIR research program as a top priority. The high beam intensity requirements for FAIR synchrotrons are imposed by this research program; for NUSTAR in particular high-intensity primary beams are essential. However, there are several destabilising effects [42], [43] that scale with the beam intensity and lead to beam losses. Therefore, these intensity-dependent effects give an upper limit for the beam intensity and can degrade the beam quality. The instabilities discussed in this work lead to the loss of the major part of the beam if not mitigated.

1.2 Intensity limitations in the SIS100

The two FAIR synchrotrons, SIS18 and SIS100, are used to accelerate and deliver the beams, ranging from protons to uranium, to the FAIR experiments. Both are designed to operate with a high beam intensity.

Intensity-dependent effects become more potent with higher beam intensity. Therefore, if the intensity-dependent effect has a negative impact on the beam dynamics, it will determine an upper intensity limit. These effects can be classified into a single particle effects and coherent effects. For single particle effects, the individual particles gain unstable trajectories, and the beam loses intensity. The coherent effects are related to the motion of the beam as a whole, for example, trajectories of the beam centre of mass or its transverse size. In this work, we only discuss in detail coherent instabilities when the whole beam becomes unstable. The beam is experiencing an *instability* when one of its statistical momenta is growing exponentially in time.

There are several significant intensity limitations for FAIR synchrotrons. Space charge [44]–[46] effects associated with the self-force (Coulomb interaction) of the beam particles on each other. The effect of this force on the beam is defocusing and, in general, this defocusing is transversely nonlinear. Transverse single-bunch instabilities for ion beams [44], [47] are discussed in this work. Some other transverse instabilities are relevant for SIS100 and SIS18 operation. For example, beam break up instability for protons is predicted to be significant for SIS100 [43]. Two-stream instabilities involve two particle species, for example, electrons and ions [43], [48]. In the SIS18, vacuum-related instabilities are also significant [49].

The topic of compensation of intensity effects related to space charge in SIS100 is currently studied [34], [50], [51]. One effect of space charge on the beam is a change in the betatron frequencies of individual particles depending on their position in the beam. For example, the net space charge force on the particle in the centre of the beam is zero. On the other hand, particles on the edges of the beam are experiencing a defocusing force due to space charge. This position-dependent defocusing, leads among others to position-dependent change in betatron frequencies. The distribution of betatron frequencies in a bunch is referred to as *tune spread*. It can lead to several undesirable effects.

Electron lenses were proposed for the compensation of this space charge tune spread in the SIS100 [35] and will be discussed in more detail in the next subsection. In particular, for space charge compensation in [35] a Pulsed Electron Lens (PEL) with a homogeneous transverse distribution of the electron beam is proposed. In the SIS100, the bunches have a length of ≈ 58 meters each, which is long enough to allow matching the electron lens current to the ion beam profile. Recent studies show a PEL to be an effective measure [34] for compensation of space charge tune spread and reducing its negative effects on the beam intensity. This type of an electron lens can also influence transverse beam stability; this effect was not considered before in the literature.

Transverse beam instabilities have been identified as a potential limiting factor in the SIS100 for the beam intensity [52], [53]. For the ion beams, the transverse head-tail instability[1] is expected to be significant. The head-tail instability occurs due to the interaction between particles in the head and tail of the bunch. This can lead to a transverse instability with a specific longitudinal pattern. Several transverse instability mitigation measures are foreseen for the SIS100: transverse feedback system [54], as an active measure; Landau Octupoles (LO) [52], [55]–[57], as a passive (Landau damping [58] measure); (linear) chromaticity adjustments [53].

This contribution describes how a PEL will affect the transverse instabilities and how it can be combined with some of the instability mitigation measures. It will be demonstrated that a PEL can also be successfully employed for transverse instability mitigation, in particular, for Landau damping.
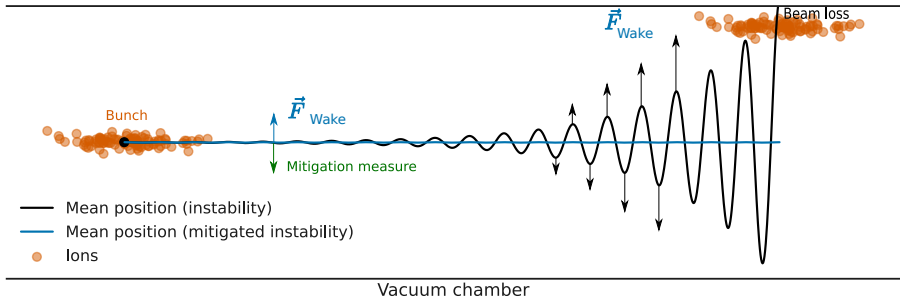
Figure 1.2: A schematic illustration of an instability (black) and a mitigated instability (blue). The external force causing the instability is shown in black and blue as $\vec{F}_{\text{external}}$. Individual particles (Ions) are displayed as orange dots.

An example [2] of a transverse instability is displayed in Fig. 1.2. Individual particles are shown in orange, the collection of these particles here is called a *bunch*. In the absence of any mitigation measure the average position of a collection of particles (shown in black) grows exponentially until the whole beam is lost. This is an example of a *coherent* instability, where all particles move as a whole and will be lost. In this example the external force is proportional to this average position. However, when mitigation measure is applied, the beam remains stable. Some of the possible mitigation measures are: Landau damping, an effect causing an energy exchange between coherent and incoherent motion; transverse feedback system, a dedicated system that detects the beam

---

[1]   see Sec. 2.3.8 for details on the instability itself

[2]   Actual instabilities in a ring accelerator typically slowly develop over many revolution turns. The external force, in this case, can be applied once per revolution turn.
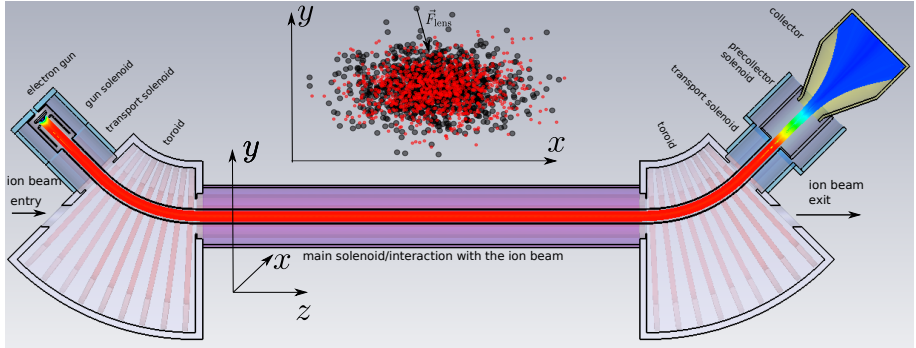
Figure 1.3: Schematic of electron beam trajectory in an electron lens prototype for SIS18 (Figure adapted from [59]). Electron beam travels from the electron gun (left) into the main solenoid (centre) and then it is dumped in the collector (right).

offset and counteracts the external force; an adjustment of chromaticity can weaken the interaction of external force with the beam.

1.3 Electron lens

Electron lens is a dedicated device, where the stored ion beam interacts with low energy electron beam. In this work, two types of electron lenses are considered. In one electron beam current is constant during the passage of the ion beam. This is what is called DC Electron Lens (DC EL). In the other electron beam current varies to match the charge distribution of the ion beam. This configuration is referred to as PEL. The ion beam is affected by an electromagnetic field of the electron beam, while the electron beam is confined by an electromagnetic field of the solenoid magnet. Schematically electron lens is demonstrated in Fig. 1.3. The electron beam is colour-coded depending on its energy, with the red colour corresponding to the maximal energy and the blue colour to the minimal one. The electron beam is generated on the electron gun cathode (left). Then it is steered into the solenoid (centre), where interaction between the ion beam and electron beam occurs. The transverse distribution of the electrons are maintained by the strong magnetic field in the solenoid. The magnetic field should be strong enough to prevent transverse oscillations of the electron beam in the interaction region. After the interaction section, the electron beam is steered into the collector (right), where the electron beam is destroyed. Every revolution, the ion beam interacts with a new electron beam, thus avoiding effects similar to electron clouds [59].

The electron lens was initially proposed for the compensation of beam-beam effects in colliders [60]–[63]. These lenses were successfully used for the beam-beam compensation in the Tevatron collider at FNAL [64], [65] and in the Relativistic Heavy Ion Collider (RHIC) at Brookhaven National Laboratory, Upton NY (BNL) [66]. Since then, electron lenses proved themselves as useful tools in various applications: beam halo collimation [67], space charge tune spread compensation [68], and others.

Recently, electron lenses have been considered for space charge compensation in FAIR synchrotrons [35]. In the SIS18, a prototype PEL will be installed [59] and the resulting increase of the space charge limit in the SIS18/SIS100 is under an active investigation [34], [59].

A PEL affects the hadron bunch via the electromagnetic field of a co-propagating (or counter-propagating) electron beam, similar to a DC EL. It relies on pulsing the electron beam current so that each particle of the hadron bunch receives a kick dependent on its longitudinal position. The longitudinal pulsing, in this work, has a Gaussian profile with the peak current occurring in the longitudinal centre of the bunch. Additionally, homogeneous transverse distribution of the electron beam is considered. This PEL was proposed in [35] for the space charge compensation in the SIS18 [31]/SIS100 [32]. Another type of an electron lens is a DC EL, where the current of the electron beam is constant. In contrast to PEL, a DC EL relies on the transverse nonlinearity of the electron beam's electromagnetic field, providing tune shifts depending on the transverse single-particle amplitudes.

1.4 Current status and motivation

Transverse collective instabilities, induced by the beam coupling impedances[3], can limit the beam intensity in synchrotrons. The head-tail instability occurs without a threshold in the beam intensity and it is observed or expected in many synchrotrons [in the heavy ion synchrotron SIS100 of the FAIR accelerator complex [36], [52] or the LHC [69], for example]. Instability mitigation methods (linear chromaticity adjustments, Landau damping, transverse feedback system, linear coupling, and others) play a crucial role in the operation of synchrotrons for high beam intensities [70].

This work focuses on Landau damping, an effect caused by energy exchange between coherent and incoherent motion of the beam particles, in ring accelerators [57], [58], [69]–[79]. This effect can occur only if there is an incoherent betatron tune spread in the bunch. The incoherent tune distribution can depend on longitudinal or transverse single-particle amplitudes. An incoherent betatron tune shift as a function of the longitudinal amplitude is referred to as longitudinal detuning. The transverse detuning is the tune shift as a function of the transverse action variable (for example, octupole magnets). The dispersion relation analytically links the incoherent tune spread to Landau damping.

---

[3] A measure of electromagnetic interaction between the beam and its surrounding environment: beam pipe, cavities, bellows and more.

This work introduces a longitudinally PEL as a source of the longitudinal detuning and demonstrates its ability to mitigate transverse instabilities via Landau damping. A PEL is compared with other possible devices (Radio Frequency Quadrupole Cavity (RFQ) [76], DC EL [77], and LO [78]) and investigate their effects on the coherent beam stability for a possible SIS100 application. The known analytical formulae are re-derived and extended to include the linear combination of longitudinal and transverse detuning. Particle tracking simulations are used to verify the analytical results. As a possible application at the SIS100, a combination of a PEL with LO is considered.

In the existing literature, Landau damping in particle accelerators is an actively researched topic. Often it is described analytically via a dispersion relation, an integral equation relating beam stability and incoherent frequency spread. Dispersion relations for Landau damping of transverse instabilities in bunches were given in Eq. (1, 2) of [75] for two particular cases: only transverse detuning or only longitudinal detuning. Combined dispersion relation for arbitrary longitudinal and transverse bunch profiles have not been given before. Such dispersion relations could be used to estimate stability boundaries from the following devices and their combinations.

LO are a standard source of the transverse detuning to mitigate transverse instabilities in several accelerators, e.g. the LHC [78], SIS100 [57] and the proposed Future Circular Collider (hadron-hadron option) (FCC-hh) [79]. In recent years, several alternative to LO methods of Landau damping were proposed, mainly for high-energy hadron colliders. The authors of [77] proposed a DC EL as a source of Landau damping due to the transverse detuning. They analytically estimated and compared the resulting stability boundary with LO for the LHC and FCC-hh using Eq. (1) from [75]. The magnitude and the shape of the stability boundaries given in [77] for a DC EL were not confirmed with particle tracking simulations for different head-tail modes.

Authors of [76] introduced an RFQ as an alternative to LO for Landau damping. An RFQ, like a PEL, provides Landau damping due to the longitudinal detuning. Studies of an RFQ using the dispersion relation (Eq. (2) in [75]) and particle tracking were performed in [71], [76]. In [76] a combination of LO with an RFQ for the instability mitigation was proposed and verified in [71] using particle tracking. However, no analytical expression for this combination was given via a dispersion relation for a bunch with a realistic Gaussian-like distribution.

In [72], [80] the second order chromaticity $\xi^{(2)}$ was studied in an experiment and, analytically, using a Vlasov formalism, where its effects on the coherent beam stability were linked to an RFQ. A new dispersion relation (see Eq. (31) in [72]) was derived, including only the longitudinal detuning. Authors of [72] established two separate effects for an RFQ and for the second order chromaticity $\xi^{(2)}$: Landau damping and an effective impedance modification. Effective impedance modification leads to a change in the instability growth rate and the frequency of coherent oscillations. These effects were studied separately. The effective impedance modification was demonstrated in a case of an airbag bunch, with no incoherent tune spread, which means no Landau damping. Landau damping was demonstrated in a regime where the effective impedance modi-

fication was shown to be weak. Therefore, it was impossible to establish the relative strength of Landau damping and the effective impedance modification for various parameter regimes. In this work, we use Vlasov formalism to derive a dispersion relation that includes a linear combination of transverse and longitudinal detuning.

Landau damping of nonzero head-tail modes was investigated in detail for transverse detuning [81] due to octupoles. Studies of a DC EL, an RFQ and the second order chromaticity $\xi^{(2)}$ neglected to discuss Landau damping of nonzero head-tail modes in detail using either particle tracking or analytical expressions. Nevertheless, in the operation usually the instability is shifted to nonzero head-tail modes by adjusting the linear chromaticity.

In hadron synchrotrons operating below transition energy, the zero head-tail mode is usually suppressed by natural chromaticity. Transverse feedback systems can be effective mitigation against head-tail instability, and other instabilities [82], [83]. However, they can have restrictions, for example, higher-order head-tail modes in short bunches or an instability due to a resistive damper [84]. In such cases, Landau damping devices are indispensable for beam stability. For the $l = 0$ mode, even if a feedback system can suppress it, Landau damping devices can be used supplementary, resulting in lower power requirements for the feedback, for example.

1.5 Overview of the thesis

In Chapter 1, a motivation for this work was given. FAIR accelerator complex was described with an emphasis on the new synchrotron SIS100. The beam intensity limitations in the SIS100 were discussed. Several existing transverse instability mitigation measures were listed. A concept of a PEL was introduced and briefly compared with a DC EL. Recent literature was discussed with an emphasis on Landau damping studies in order to motivate this study.

Chapter 2 introduces fundamental concepts of beam dynamics in accelerators, starting from a single particle motion and ending with collective instabilities and Landau damping. Only the concepts relevant to understanding the present work are discussed. Known instability mitigation methods are briefly introduced. Among them, Landau damping is explained in detail.

Chapter 3 describes the simulation framework and numerical implementation of a PEL that are used in this study. The general concept of macroparticle tracking codes is introduced and discussed.

Chapter 4 focuses on the coasting beam experiments conducted as a part of this study. In the beam dynamics experiments, an existing electron cooler in the SIS18 was used as a (transversely) non-linear DC EL. Its effects on the transverse beam stability were studied in the experiment. First, the experimental setup used in the SIS18 beam time is explained in detail. Then, the results are presented for studies with $^{40}Ar^{10+}$ and $^{40}Ar^{18+}$ beams. Finally, the obtained results are interpreted with a semi-analytical model.

Chapter 5 presents this study's main analytical results. First, the effect of a PEL on the coherent beam dynamics is discussed. PEL is determined to be a strong source of longitudinal betatron frequency detuning and is related to an RFQ and higher order chromaticity. First, we demonstrate that the longitudinal detuning induced by a a PEL leads to Landau damping of a transverse head-tail instability. Second, two effects of a PEL on the head-tail instability are analysed: Landau damping and the effective impedance modification. The effective impedance modification is related in this work to the head-tail mode spectrum distortion by the longitudinal detuning. Third, an integral equation for the longitudinal modes, including both longitudinal and transverse detuning, is derived. Finally, new dispersion relations are derived for the linear combination of longitudinal detuning and transverse detuning.

Chapters 6, 7 discuss the main numerical results of this study. Chapter 6 presents the simulation results for Landau damping of head-tail mode zero. Zero head-tail mode stability boundaries are reconstructed for a PEL, a DC EL, LO and an RFQ by the means of particle tracking using an antidamper [85] as a rigid mode kick (Section 6.2). Similar reconstruction methods were used in [86] for the transverse plane and in [87] for the longitudinal plane. These simulation results are compared to the respective dispersion relations from Section 5. Furthermore, with this method, we validate the dispersion relation for a combination of LO and a PEL for the FAIR SIS100.

In Chapter 7, we investigate Landau damping of nonzero head-tail modes using a resistive wall impedance model (Section 7.1). Particle tracking simulation results are compared with analytical formulae of Chapter 5 for a PEL, a DC EL, LO, an RFQ. We discover that the effective impedance modification for nonzero head-tail modes significantly increases the threshold for Landau damping due to the longitudinal detuning.

In Chapter 8, the main results of this work are summarised and the limitations of the current study are discussed briefly.

2 Fundamentals of accelerator beam dynamics

The beam dynamics topics and terminology relevant to the understanding of this work are presented in this chapter. Detailed discussion of particle dynamics in accelerators can be found in numerous textbooks, for example in [88]–[91], in particular the high intensity dynamics in [43], [92].

Any particle of the beam can be described by six coordinates and the location s of the reference particle in the accelerator:

$$\vec{X}(s) = (x(s),\, x'(s),\, y(s),\, y'(s),\, z(s),\, \delta(s))^T. \tag{2.1}$$

Location along the accelerator s is conventionally used in accelerator physics instead of time. The coordinates x', y', δ, s are defined as

$$x'_i = \frac{\mathrm{d}x_i}{\mathrm{d}s_i} = \frac{p_x}{p_0}, \tag{2.2}$$

$$y'_i = \frac{\mathrm{d}y_i}{\mathrm{d}s_i} = \frac{p_y}{p_0}, \tag{2.3}$$

$$\delta_i = \Delta p_i / p_0, \tag{2.4}$$

$$s_i = \int_0^t v_0(\tilde{t})\mathrm{d}\tilde{t}, \tag{2.5}$$

where p_0 is the reference particle momentum, p_x, p_y are the horizontal and vertical momenta of a deviated particle, Δp_i is the momentum offset from the reference particle, and v_0 is the reference particle velocity. The *momentum deviation* is defined as the ratio of the momentum offset Δp_i and the reference particle momentum p_0. The x', y' variables describe the slope between reference particle momentum and the deviated particle momentum. These coordinates are always defined relative to the coordinates of the *reference particle*, that travels on the design orbit with design energy. In this coordinates reference particle is always located at the origin. The particles with nonzero momentum deviation are called *off momentum particles*.

Figure 2.1 illustrates the coordinate frame, co-moving with the reference particle. The reference particle (red dot) travels along the reference orbit (red curve), while the deviated particle (green dot) travels along its actual orbit (green curve). The deviated
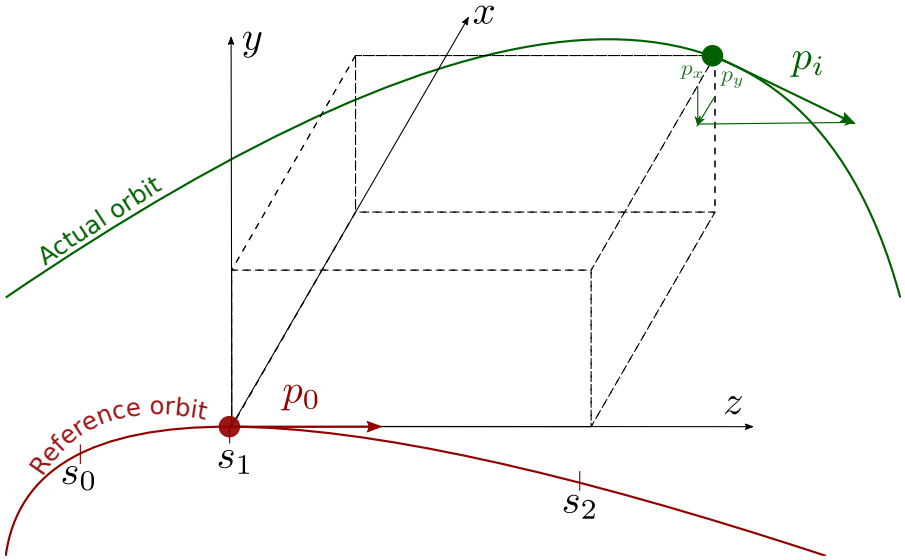
Figure 2.1: Moving frame coordinate system is illustrated as black axis lines. The coordinate frame is moving with the reference particle from point s_0, through s_1 and to s_2. In red, the reference particle orbit is shown. The green line is the actual orbit of a deviated particle. The deviated particle is located $\{x, y, z\}$ and has a momentum p_i. The coordinates of all deviated particles are always described w.r.t. the reference particle position.

particle is fully described by this set of coordinates. The deviated particle coordinates are always described w.r.t. the reference particle position.

Beam rigidity is defined as

$$B\rho = p_0/(eZ), \tag{2.6}$$

where e is the elementary electric charge, Z is the charge number of the ion. The beam rigidity relates the strength of the bending magnets and effective radius of the accelerator to the beam energy that can be achieved. Beam rigidity is often mentioned instead of energy in heavy ion accelerators because of the variety of ions accelerated. This allows to give a single quantity describing the available energies for different ions.

2.1 Transverse beam dynamics

The single-particle dynamics of a particle in an accelerator can be split into a transverse dynamics and longitudinal dynamics. Usually, the transverse motion occurs at a much higher frequency. Therefore, we can rightfully approximate transverse and longitudinal motion to be independent of each other.

2.1.1 Single-particle dynamics

In an alternating gradient synchrotron, the transverse particle dynamics are described with a Hill equation

$$x'' + K_x(s)x = 0, \tag{2.7}$$

$$y'' + K_y(s)y = 0, \tag{2.8}$$

where $K_{x,y}(s)$ is the horizontal and vertical focusing functions. In a ring accelerator, these function will be periodic, $K_{x,y}(s) = K_{x,y}(s + C)$, with a period equal to the circumference of the ring C. One of the simplest ways to make an alternating gradient focusing is the use of a Focusing - drift space - Defocusing - drift space (FODO) cell structure. The focusing and defocusing is typically achieved with quadrupole magnets. In a FODO cell, $K_x(s) = -K_y(s)$, due to the geometry of a quadrupole magnet. The solutions of the Hill equation, for example for the horizontal plane are described as

$$x = A_x w_x(s) \cos\left(\psi_{\hat{\beta}_x}(s) + \theta_{\hat{\beta}_x}\right), \tag{2.9}$$

$$x' = A_y w_y(s) \left[-\psi'_{\hat{\beta}_x}(s) \sin\left(\psi_{\hat{\beta}_x}(s) + \theta_{\hat{\beta}_x}\right) + \frac{w'_x(s)}{w_x(s)} \cos\left(\psi_{\hat{\beta}_x}(s) + \theta_{\hat{\beta}_x}\right) \right], \tag{2.10}$$

where $A_{x,y}$ are the horizontal and vertical amplitudes of particle oscillations. The initial betatron phase offset, determined by the ratio of x and x', is denoted as $\theta_{\hat{\beta}_x}$. Functions $w_{x,y}(s)$ are the horizontal and vertical envelope functions, describing the envelope of the particle oscillations along the accelerator ring. Functions $\psi_{\hat{\beta}_{x,y}}(s)$ are called horizontal and vertical betatron phase advance.

Twiss parameters or *Twiss functions* are defined as follows

$$\hat{\beta}_{x,y}(s) = w_{x,y}^2(s), \tag{2.11}$$

$$\hat{\alpha}_{x,y}(s) = -\hat{\beta}'_{x,y}(s)/2, \tag{2.12}$$

$$\hat{\gamma}_{x,y}(s) = \frac{1 + \hat{\alpha}_{x,y}^2(s)}{\hat{\beta}_{x,y}(s)}. \tag{2.13}$$

Twiss beta function is defined as proportional to the envelope of particle oscillations. Here we use a proportionality constant equal to 1. Twiss alpha function is related to the slope of this envelope.

The betatron phase $\psi_{\hat{\beta}_{x,y}}$ and betatron tune $Q_{x,y}$ are defined as

$$\psi_{\hat{\beta}_{x,y}} = \int\limits_{0}^{s} \frac{d\tilde{s}}{\hat{\beta}_{x,y}(\tilde{s})}, \tag{2.14}$$

$$Q_{x,y} = \frac{1}{2\pi} \oint \frac{ds}{\hat{\beta}_{x,y}(s)}. \tag{2.15}$$

Betatron tune is the number of transverse oscillations a particle makes in a single revolution period. The betatron tune can be split into an integer part and a fractional part of the tune. The integer part describes the number of full oscillations. The fractional part of the tune describes the incomplete part of the oscillation. The transverse dynamics can often only depend on the fractional part of the tune. Betatron tune can be estimated from a uniform focusing approximation:

$$Q_{x,y} \approx R/\langle\hat{\beta}_{x,y}\rangle, \tag{2.16}$$

where $R = C/(2\pi)$ is the effective radius of the accelerator, $\langle\hat{\beta}_{x,y}\rangle$ is the average Twiss beta function.

Figure 2.2 represents the motion of a particle on the horizontal phase space x, x' plane. The particle (orange dot) coordinates x, x' are restricted to an ellipse defined by the Twiss parameters. The Twiss parameters are changing with s, transforming the ellipse but the ellipse area $\pi\varepsilon_x$ stays constant. Furthermore, Twiss parameters are periodic in s with the period of accelerator circumference C. Thus the phase-space ellipse at s repeats itself at $s + nC$ ($n \in \mathbf{N}$), but the particle arrives each turn with a phase advance by $\Delta\psi_{x,y}(s) = 2\pi Q_{x,y}$. Therefore, at the location s the particle over many turns will fill out the ellipse from Fig. 2.2 (if the fractional part of the tune has several digits)

The ellipse is described by the Twiss parameters as

$$\hat{\gamma}_x x^2 + 2\hat{\alpha}_x x x' + \hat{\beta}_x x'^2 = \pi\varepsilon_x. \tag{2.17}$$
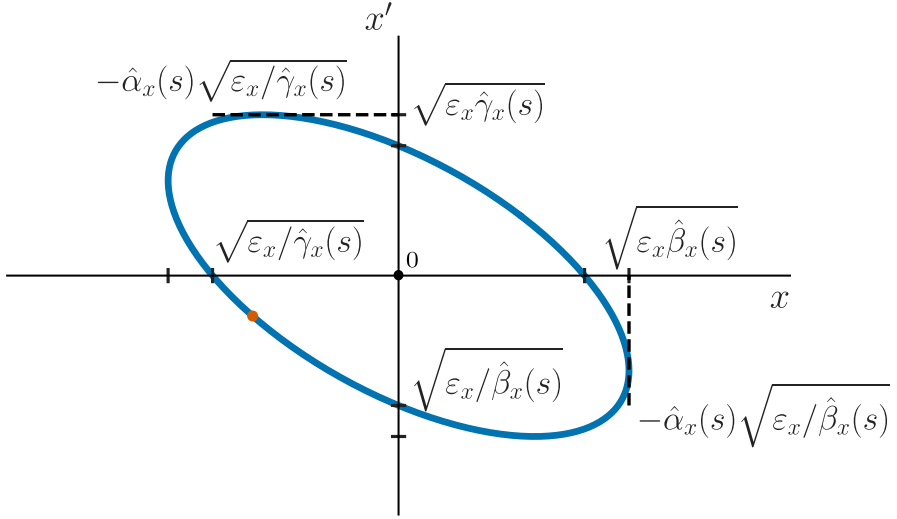
Figure 2.2: Horizontal phase space for a single particle (orange dot shows initial coordinates). The particle can only have coordinates that lie on an ellipse with the area of $\pi\varepsilon_x$. The characteristics of this ellipse are expressed via Twiss parameters.

Since the area of this ellipse $\pi\varepsilon_x$ is constant, ε_x is an invariant of motion. The coordinates $\{u, u'\}$ ($u \in \{x, y\}$) could be transformed in $\{J_u, \theta_u\}$ coordinates with $J_u \propto \varepsilon_u$ as follows

$$u = \sqrt{2J_u\hat{\beta}_u}\cos\theta_u, \tag{2.18}$$

$$u' = -\sqrt{2J_u\hat{\beta}_u}\sin\theta_u, \tag{2.19}$$

where J_u is called action, or particle amplitude, θ_u is called angle coordinate.

If the focusing $K_{x,y}(s)$ in an accelerator can be assumed to be independent of the particle amplitudes J_u, then all particles have the same betatron tunes Q_{x_0}, Q_{y_0}. The approximate Hamiltonian $\mathcal{H}_\perp$ of this system is that of a two-dimensional harmonic oscillator:

$$\mathcal{H}_\perp = Q_{x_0}J_x + Q_{y_0}J_y. \tag{2.20}$$

In an accelerator, the focusing can always depend on the transverse amplitudes of the particles or be perturbed by an unintended magnetic field deviation. This *detuning* can be described as

$$\Delta Q_u = \frac{1}{4\pi} \oint \frac{\hat{\beta}_u(s) B_u'(s)}{B\rho} \mathrm{d}s, \tag{2.21}$$

where B_u' is the gradient of the magnetic field. The detuning is usually a lot weaker than the linear focusing of the accelerator. Meaning that $\delta Q_{x,y} \ll Q_{x_0,y_0}$ One particular example of betatron frequency detuning is the detuning due to octupole magnets [78]. The magnetic field of an octupole is described as:

$$B_y + jB_x = O_3(x + jy)^3, \tag{2.22}$$

where O_3 is the octupolar strength [78], [83], j is used to describe the imaginary unit throughout this work. In the action-angle coordinates the magnetic field has first and third order harmonics of $\theta_{x,y}$.
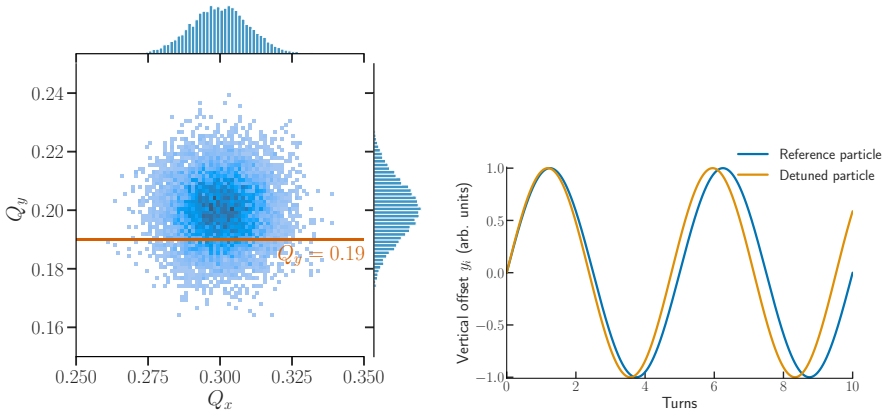
Figure 2.3: (Left) An example of an incoherent tune distribution in both vertical and horizontal planes. The coloured histogram shows the tunes of individual particles. The orange line indicates where on the tune diagram the particles with the tune of $Q_y = 0.19$ are located. (Right) An example of betatron oscillations of different particles within the tune spread.

For dipolar oscillations the third harmonic terms can be omitted. Then the magnetic field gradients in action-angle variables are expressed as

$$\frac{\partial B_x}{\partial y} \approx \frac{3}{2} O_3 (\hat{\beta}_x J_x - 2\hat{\beta}_y J_y), \tag{2.23}$$

$$\frac{\partial B_y}{\partial x} \approx \frac{3}{2} O_3 (2\hat{\beta}_x J_x - \hat{\beta}_y J_y), \tag{2.24}$$

where $\hat{\beta}_{x,y}$ are vertical and horizontal beta functions at the location of an octupole magnet.

From the tune shift formula Eq. (2.21) then we obtain a tune shift depending on the action variables

$$\Delta Q_x(J_x, J_y) = a_{xx} J_x + a_{xy} J_y, \tag{2.25}$$

$$\Delta Q_y(J_x, J_y) = a_{yx} J_x + a_{yy} J_y, \tag{2.26}$$

where a_{xx}, a_{xy}, a_{yx}, a_{yy} are called *octupole detuning coefficients*. This coefficients are defined as:

$$a_{uu} = \frac{3}{8\pi} \oint \hat{\beta}_u^2 \frac{O_3}{B\rho} \mathrm{d}s, \tag{2.27}$$

$$a_{uv} = -\frac{3}{8\pi} \oint \hat{\beta}_u \hat{\beta}_v \frac{O_3}{B\rho} \mathrm{d}s, \tag{2.28}$$

where u and v each stand for either x or y, the integration over s is performed to account for octupoles distributed at different positions in a ring.

Octupoles are only one of the ways to create a betatron frequency detuning. In this work we refer to all betatron frequency detuning that depends on transverse action variables (J_x, J_y) as the *transverse detuning*. While the betatron frequency detuning that depends on the longitudinal variables (z, δ) and longitudinal action angle variables (J_z, φ), as the *longitudinal detuning*.

Figure 2.3 illustrates betatron frequency detuning: (left) 2D histogram of individual particle horizontal Q_x and vertical Q_y tunes; (right) an example of transverse offset of a reference particle (blue) and a particle with a detuned frequency (yellow). In this illustrative figure the horizontal and vertical tunes simply have a Gaussian distribution. For a small transverse detuning $\Delta Q_u \ll Q_u$, the Hamiltonian of the transverse motion can be written as

$$\mathcal{H}_\perp = [Q_{x_0} + \Delta Q_x(J_x, J_y)]J_x + [Q_{y_0} + \Delta Q_y(J_x, J_y)]J_y = Q_x J_x + Q_y J_y. \tag{2.29}$$

2.2 Longitudinal beam dynamics

In a synchrotron the particles are accelerated repeatedly by RF cavities. The cavities create a longitudinal potential and confine the particles longitudinally into *bunches*. The RF voltage as a function of time can be expressed as:

$$V_{RF}(t) = V_0 \sin(h_{RF}\omega_0 t + \phi_0) = V_0 \sin\phi_s, \tag{2.30}$$

where we define ϕ_s as the *synchronous phase*, the phase at which the reference (sometimes also referred to as synchronous) particle arrives at the cavity; V_0 is the maximum RF voltage; h_{RF} is called the RF harmonic. ω_0 is the angular revolution frequency. The deviated particle has a different phase $\phi_i = \phi_s + \Delta\phi_i$, where $\Delta\phi_i = 2\pi\frac{zh_{RF}}{C}$. While discussing longitudinal dynamics the reference particle with phase ϕ_s is referred to as *synchronous particle*. The longitudinal motion of an individual particle i is described by the following set of differential equations

$$\frac{d\delta_i}{dt} = \frac{\omega_0 q V_0}{2\pi E_0 \beta_r^2}(\sin\phi_i - \sin\phi_s), \tag{2.31}$$

$$\frac{d\phi_i}{dt} = h_{RF}\omega_0 \frac{\Delta\tau_i}{\tau}, \tag{2.32}$$

where E_0 is the energy of the reference particle, q is the electric charge of a particle, τ is the arrival time of the reference particle, $\Delta\tau_i$ is the difference in arrival time between particle i and the reference particle. This difference in arrival times depends on the speed at which particle travels in the accelerator and on the length of its closed orbit.

2.2.1 Momentum compaction factor and transition energy

The difference $\Delta\tau_i$ between arrival time of a deviated particle i and the reference particle τ is described as follows

$$\frac{\Delta\tau_i}{\tau} = \frac{\Delta L_i}{L} - \frac{\Delta v_i}{v}, \tag{2.33}$$

where L is a closed orbit of the reference particle (equal to the design circumference C), ΔL_i is a difference between closed orbits of deviated particle i and the reference particle, $v = \beta_r c$ is the speed of the reference particle, Δv_i is the difference between the speed of the deviated and reference particle. The first term is the influence of deviated particle having a different path length L_i that the reference particle. Indeed, particles that have a longer path $\Delta L_i > 0$ will contribute to a later arrival time. The momentum

compaction factor $\alpha_c^{(n)}$ is defined as a proportionality coefficient between the relative change in path of an off-momentum particle and the momentum deviation δ_i:

$$\Delta L_i/L = \sum_{n=1}^{\infty} \alpha_c^{(n)} \delta_i^n \approx \alpha_c^{(n)} \delta_i + O(\delta_i^2).$$ (2.34)

In this work only the first order momentum compaction factor is considered. Throughout this work it is referred to as the momentum compaction factor α_c.
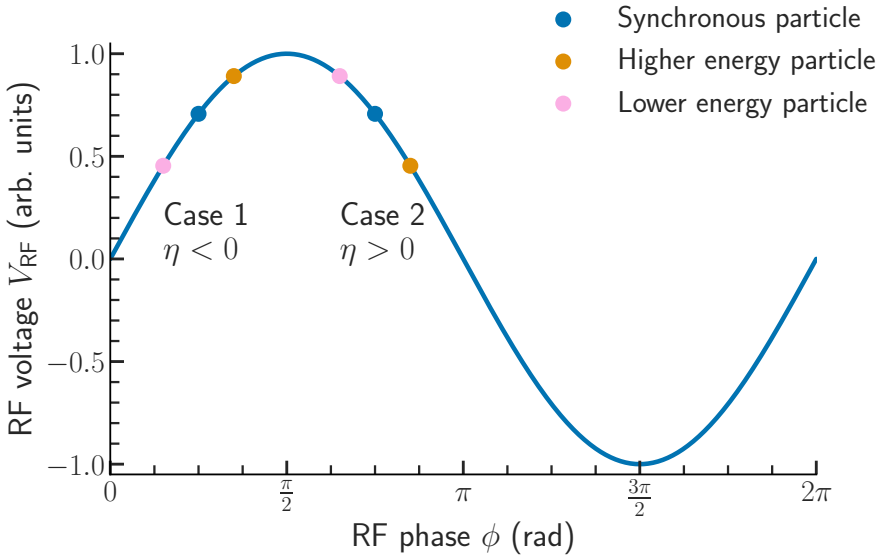
Figure 2.4: RF voltage seen by the reference particle, and particles with higher and lower energy than the reference particle. Two cases are presented: $\eta > 0$ case is the acceleration above transition energy; $\eta < 0$ case is the acceleration below transition energy.

The second term reflects the impact of a different deviated particle speed. If the particle is faster than the reference particle $\Delta v_i > 0$, the arrival time τ_i is shorter. This term can be expressed as a difference in particle momentum

$$\frac{\Delta v_i}{v} = \frac{1}{\gamma_r^2} \delta_i,$$ (2.35)

where γ_r is the relativistic gamma factor.

The dependency of the arrival time difference on the momentum deviation is expressed as:

$$\frac{\Delta \tau_i}{\tau} = \sum_{n=0}^{\infty} \eta^{(n)} \delta^n,$$

(2.36)

similarly to the higher order momentum compaction factor $\alpha_c^{(n)}$. In this work only the first-order dependency $\eta^{(1)} = \eta$ is considered. We can define the proportionality coefficient between relative time slippage $\Delta \tau_i / \tau$ and the momentum deviation δ as the *slip factor*:

$$\eta = \alpha_c - \frac{1}{\gamma_r^2} = \frac{1}{\gamma_t^2} - \frac{1}{\gamma_r^2}.$$

(2.37)

The *transition energy* is determined as the energy at which the slip factor is zero:

$$\gamma_t = 1/\sqrt{\alpha_c}.$$

(2.38)

The slip factor can have a positive or a negative sign. For a positive slip factor, particles with longer path $\Delta L_i > 0$ have a later arrival time $\Delta \tau_i > 0$, for a negative slip factor – an earlier arrival time $\Delta \tau_i < 0$.

Figure 2.4 illustrates two scenarios: particle acceleration below and above the transition energy. In the case below transition energy $\eta < 0$, the phase of the synchronous particle must be between 0 and $\pi/2$ for a stable acceleration. This range can be understood if we consider two other particles: one (orange dot) with higher energy than the reference particle; another (magenta dot) with lower energy than the reference particle. The higher energy particle $\delta_i > 0$ will arrive at a time $\tau_i = \tau(1 + \eta \delta_i) < \tau$, and will be decelerated w.r.t. the reference particle. On the next revolution turn this particle will arrive at a time closer to the reference particle one. The particle with lower energy $\delta_i < 0$ will be accelerated instead, and will arrive on the next revolution turn also at a time closer to a reference particle.

2.2.2 RF buckets and the synchrotron motion

The longitudinal phase space area of particles circulating in a synchrotron is divided by a line called *separatrix* into two regions where the particle motion in it is qualitatively different. In areas enclosed by the separatrix, the particles have closed trajectories in a phase space and are confined. The longitudinal phase space area that lies inside the separatrix is called a *bucket*. Outside the separatrix, a particle can be found anywhere in the accelerator. With a different RF setting, for example for acceleration, the particles outside of the separatrix will be lost.

In Fig. 2.5 one bucket around the position $z = 0$ is illustrated along with the halves of its neighbouring buckets. The *bunch* is all the particles that are located inside a single bucket. In a synchrotron several bunches can travel simultaneously depending on the RF harmonic h_{RF}. For example, in the SIS100 $h_{RF} = 10$ and two buckets are left empty. In this situation 8 bunches are present in 8 non empty buckets in the SIS100.
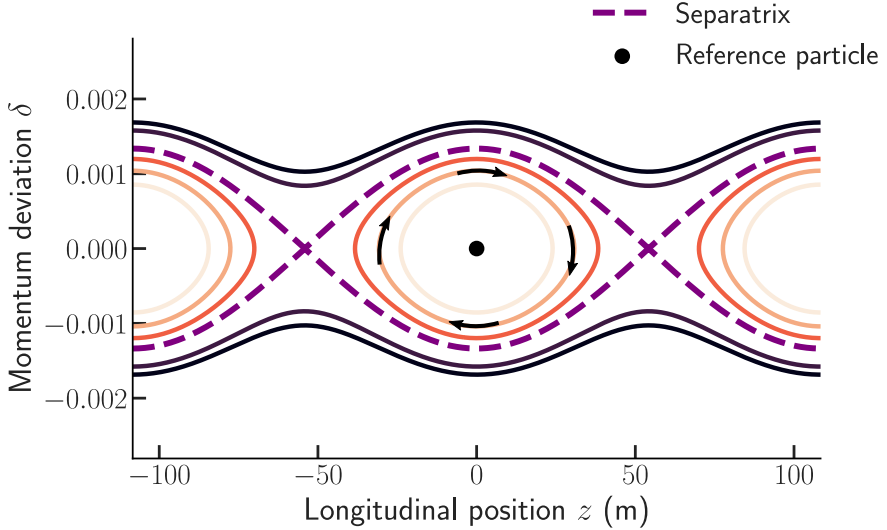
Figure 2.5: An example of an RF bucket and the separatrix (purple dashed curve), calculated from Eq. (2.39). Trajectories inside the separatrix are shown in bright orange colours. Trajectories outside of the separatrix are shown in dark purple and black. Accelerator parameters of SIS100 from Table 1.1 were used to produce this figure (below transition energy $\eta < 0$).

The Hamiltonian of the longitudinal motion is given by

$$\mathcal{H}_{\parallel} = \frac{1}{2} h_{RF} \omega_0 \eta \delta_i^2 + \frac{\omega_0 q V_0}{2\pi \beta_r^2 E_0} \left[\cos \phi_i - \cos \phi_s + (\phi_i - \phi_s) \sin \phi_s \right]. \tag{2.39}$$

If we examine a particle with a small phase $\phi_i - \phi_s \ll 1$ and small momentum offset $\delta_i \ll 1$, they all rotate in the longitudinal phase space with the same frequency Ω_{s_0}. This

frequency is referred to as *small amplitude synchrotron frequency* or simply as *synchrotron frequency*. A synchrotron tune is defined as

$$Q_{s_0} = \Omega_{s_0}/\omega_0 = \sqrt{\frac{qh_{\mathrm{RF}}V_0|\eta\cos\phi_s|}{2\pi m\gamma_r\beta_r^2 c^2}}, \tag{2.40}$$

where m is the mass of the particle. It describes the number of oscillations a particle makes in the longitudinal phase space in a single revolution turn. Particles that do not fulfill the assumptions above will have a different synchrotron tune $Q_s \neq Q_{s_0}$. The synchrotron tune in modern ring accelerators has only a fractional part. The speed of oscillations in the longitudinal plane is much slower than in the transverse plane $Q_{s_0} \ll Q_{x,y}$. The factor $|\eta\cos\phi_s|$ is taken as a modulus, in fact for a case $\eta < 0$, below transition energy $0 < \phi_s < \pi/2$ meaning that $\cos\phi_s > 0$. While for the case above transition energy $\eta > 0$ the cosine is negative $\cos\phi_s < 0$. Thus, $\eta\cos\phi_s$ is always negative for the stable motion, and the modulus is taken for convenience.

Practically, the sign of the slip factor η determines the direction of rotation of the particles in the longitudinal phase space. This can be determined from the equations of motion Eqs. (2.31, 2.32), where the sign of η determines the sign of the derivatives. For $\eta < 0$, the particles travel in a counterclockwise direction in phase space, as demonstrated by black arrows in Fig 2.5. For $\eta > 0$, the particles will travel in the clockwise direction. For the special case of the bunch at the transition energy $\eta = 0$, the synchrotron motion is frozen $Q_{s_0} = 0$.

Depending on the slip factor of the ring accelerator, the synchronous phase ϕ_s is chosen to be either 0 or π to keep the energy of the bunched beam constant. The synchrotron tune in hadron synchrotrons is of the order $\approx 10^{-3}$, and in the electron synchrotrons it is often higher $\approx 10^{-2}$.

Similarly to the transverse planes we can define a longitudinal Twiss beta function (that has the same dimension of meters):

$$\hat{\beta}_z = \frac{\eta v}{Q_{s_0}\omega_0}. \tag{2.41}$$

And the longitudinal coordinates z, δ can be expressed as action-angle coordinates J_z, φ. The simplified Hamiltonian for the linear synchrotron motion is:

$$\mathscr{H}_\parallel = Q_{s_0}J_z. \tag{2.42}$$

The full Hamiltonian of transverse and longitudinal motion in our approximation is simply $\mathscr{H} = \mathscr{H}_\perp + \mathscr{H}_\parallel$.

2.2.3 Chromaticity

The chromaticity is an important effect in the beam dynamics. It links a longitudinal coordinate δ to the change of the transverse betatron tune $\Delta Q_{x,y}$. This proportionality coefficient between the ratio of tune spread $\Delta Q_{x,y}$ to the reference particle tune Q_{x_0,y_0} and the ratio of momentum spread Δp to reference particle momentum p_0 is known as (linear) chromaticity $\xi_{x,y}^{(1)}$:

$$\Delta Q_{x,y}/Q_{x_0,y_0} = \xi_{x,y}^{(1)} \delta, \tag{2.43}$$

where $\delta = \Delta p/p_0$. Sometimes $\xi_{x,y}^{(1)}$ is referred to as the normalised chromaticity, and $\xi_{x,y}^{(1)} Q_{0_{x,y}}$ is then called chromaticity. In this work this property $\xi_{x,y}^{(1)}$ will simply be referred to as *linear chromaticity*. The chromaticity of the accelerator without a dedicated correction scheme is called *natural chromaticity*. For example, the natural chromaticity of a FODO cell is precisely $\xi_{x,y}^{(1)} = -1$. In many synchrotrons the natural chromaticity is shifted to a different value in order to optimise the performance of the accelerator. This is achieved by using a dedicated sextupole magnets. Usually a two-family scheme is employed to control the chromaticity in the vertical and horizontal planes independently.

This concept of the chromaticity can be expanded to include the dependency of the tune spread on higher order of momentum deviation δ^n. This property is referred to as higher order or *nonlinear chromaticity* $\xi_{x,y}^{(n)}$:

$$\Delta Q_{x,y}/Q_{x_0,y_0} = \sum_{n=1}^{\infty} \xi_{x,y}^{(n)} \delta^n \approx \xi_{x,y}^{(1)} \delta + \xi_{x,y}^{(2)} \delta^2 + O(\delta^3), \tag{2.44}$$

where (n) in $\xi_{x,y}^{(n)}$ denotes order of the chromaticity, but in δ^n, n is the argument of the exponentiation operation.

2.3 Multiparticle dynamics and beam distribution function

Considering each individual particle in the beam separately is impractical, taking into account, that beam intensities in modern heavy ion synchrotrons can be higher than 10^{11} particles. Instead, a distribution of particles and the momenta of the particle distribution can be considered to describe the beam as a whole.

2.3.1 Emittance and rms beam properties

An ensemble of particles in the beam can be described by a *distribution function*

$$\Psi = \Psi(x, x', y, y', z, \delta; s) = \Psi(J_x, \theta_x, J_y, \theta_y, J_z, \varphi; s). \tag{2.45}$$

The first momentum of a distribution function will determine the transverse (or longitudinal) *total beam offset*

$$\langle u \rangle (s) = \overline{u}(s) = \int u \Psi(x, x', y, y', z, \delta; s) \mathrm{d}x \mathrm{d}x' \mathrm{d}y \mathrm{d}y' \mathrm{d}\delta \mathrm{d}z, \tag{2.46}$$

where $u \in \{x, y\}$. Additionally to the total beam offset, a related quantity can be defined *local beam offset* or *beam offset*. This would describe the beam offset within the bunch, depending on the position z

$$\langle u \rangle (z, s) = \overline{u}(z, s) = \int u \Psi(x, x', y, y', z, \delta; s) \mathrm{d}x \mathrm{d}x' \mathrm{d}y \mathrm{d}y' \mathrm{d}\delta. \tag{2.47}$$

The commonly used statistical quantity, describing the beam size in transverse or longitudinal direction is *rms beam size*

$$\sigma_{u=x,y,z}(s) = \int (u - \overline{u})^2 \Psi(x, x', y, y', z, \delta; s) \mathrm{d}x \mathrm{d}x' \mathrm{d}y \mathrm{d}y' \mathrm{d}\delta \mathrm{d}z. \tag{2.48}$$

One can define an *rms emittance* as:

$$\varepsilon_u = \sqrt{\langle u^2 \rangle \langle u'^2 \rangle - \langle u u' \rangle^2}, \tag{2.49}$$

where $u \in \{x, y\,z\}$. The main focus of this work is the stability of the transverse beam offset over time s.

2.3.2 Vlasov equation

For the analysis of beam stability with the distribution function one can employ Liouville's theorem, which states the preservation of the particle density in phase space under the influence of conservative forces [88]:

$$\frac{\mathrm{d}\Psi}{\mathrm{d}s} = \frac{\partial \Psi}{\partial s} + [\mathcal{H}, \Psi], \tag{2.50}$$

where H is the Hamiltonian of motion, $[\mathcal{H}, \Psi]$ denotes a Poisson bracket. This expression is also known as the *Vlasov equation*.

2.3.3 Detuning due to a pulsed electron lens

Here we assume that a PEL has a homogeneous (and round) transverse distribution, and the distribution of a PEL current is Gaussian. Additionally, PEL beam fully covers the ion beam transversely. Hamiltonian $\mathscr{H}_{\text{PEL}}$ of the PEL is $\mathscr{H}_{\text{PEL}} = \int_0^{r_\perp} F_{r_\perp} \, dr_\perp$:

$$\mathscr{H}_{\text{PEL}} = \frac{I_{\max} e(1 \pm \beta_e \beta_i)}{\varepsilon_0 c \beta_e \sigma_e^2 p_0 \omega_0} r_\perp^2 \exp\left(-\frac{z^2}{2\sigma_e^2}\right). \tag{2.51}$$

where $I_{\max}$ is the maximal current of the electron beam; β_e is the relativistic beta of the electron beam; β_i is the relativistic beta of the ion beam; ε_0 is the vacuum permitivity or an electron constant; σ_e is the rms longitudinal size of the electrom beam; p_0 is the momentum of the reference particle in the beam; ω_0 is the angular revolution frequency; $r_\perp^2 = x^2 + y^2$ is the radius of the ion beam in the transverse direction; z is the longitudinal position of a particle within the ion beam. While considering y-plane effects, x-plane term could be ignored as the derivatives of the respective Hamiltonian over J_y are zero, and we will show that all derivatives over the longitudinal coordinates can be neglected

$$\mathscr{H}_{\text{PEL}} = \left(\frac{2I_{max} e(1 \pm \beta_e \beta_i)}{\varepsilon_0 c \beta_e \sigma_e^2 p_0 \omega_0} \beta_y\right) J_y (1 + \cos 2\theta_y) \exp\left[-\frac{J_z \beta_z}{2\sigma_e^2}(1 + \cos 2\varphi)\right], \tag{2.52}$$

where we have changed to action-angle coordinates $(J_x, \theta_x, J_y, \theta_y, J_z, \varphi)$. Let us examine the derivatives and determine smallness parameters for each derivative starting with the detuning derivative

$$\Delta Q_y^{\|} = \frac{\partial \mathscr{H}_{\text{PEL}}}{\partial J_y} = A\beta_y(1 + \cos 2\theta_y)\exp\left[-\frac{J_z}{2\varepsilon_z}\frac{\sigma_z^2}{\sigma_e^2}(1 + \cos 2\varphi)\right] \propto \Delta Q_{\max}, \tag{2.53}$$

where σ_z is the rms longitudinal size of the ion beam; $\Delta Q_{\max}$ is the maximum tune shift due to the electron lens. In this particular case, the maximum tune shift is achieved for the particles in the longitudinal centre of the beam. The term $A\beta_y$ is a dimensionless constant that represents the maximum tune shift $\Delta Q_{\max}$ due to the electron lens, i.e. tune shift for a particle with zero amplitude $(J_x, J_y, J_z) = 0$. Another important term, that can cause Landau damping (via detuning of the synchrotron tune) is

$$\begin{aligned}
\Delta Q_s^{\text{PEL}} &= \frac{\partial \mathscr{H}_{\text{PEL}}}{\partial J_z} = A\beta_y J_y \frac{\sigma_z^2}{\sigma_e^2}\frac{1}{\varepsilon_z}(1 + \cos 2\theta_y)(1 + \cos 2\varphi) \\
&\times \exp\left[-\frac{J_z}{2\varepsilon_z}\frac{\sigma_z^2}{\sigma_e^2}(1 + \cos 2\varphi)\right] \propto \Delta Q_{\max}\frac{\varepsilon_y}{\varepsilon_z},
\end{aligned}$$

where $\varepsilon_{x,y}$ are the rms geometrical transverse emittances of the ion beam; ε_z is the rms geometrical longitudinal emittance of the ion beam. This term is directly proportional to the transverse emittance of the beam and inversely proportional to the longitudinal emittance. For this term we assume that PEL is matched to the ion beam longitudinal profile $\sigma_e = \sigma_z$. The same applies to the following term:

$$\frac{\partial \mathcal{H}_{\text{force}}}{\partial \varphi} = A\beta_y J_y \frac{J_z}{\varepsilon_z} \frac{\sigma_z^2}{\sigma_e^2} (1 + \cos 2\theta_y) \exp\left[-\frac{J_z}{\varepsilon_z} \frac{\sigma_z^2}{2\sigma_e^2} (1 + \cos 2\varphi) \right] \propto \Delta Q_{\text{max}} \varepsilon_y, \quad (2.54)$$

and the last term affects non-dipolar harmonic of the transverse motion:

$$\frac{\partial \mathcal{H}_{\text{PEL}}}{\partial \theta_y} = A\beta_y J_y \sin 2\theta_y \exp\left[-\frac{J_z}{2\varepsilon_z} \frac{\sigma_z^2}{\sigma_e^2} (1 + \cos 2\varphi) \right] \propto \Delta Q_{\text{max}} \varepsilon_y. \quad (2.55)$$

Additionally, one can ignore all the harmonics higher than θ_y for the transverse motion, as it's driven by a dipolar force – eliminating the $\frac{\partial \mathcal{H}_{\text{PEL}}}{\partial \theta_y}$ term, and the last term appears in the Vlasov equation as $\frac{\partial \mathcal{H}_{\text{PEL}}}{\partial \varphi} \frac{\partial \psi_0}{\partial J_z}$, with the whole term scaling as $\varepsilon_y/\varepsilon_z$. This effect can be ignored as long as $\varepsilon_y \ll \varepsilon_z$, which is usually the case in particle accelerators.

For the SIS100, $\varepsilon_y/\varepsilon_z < 10^{-3}$, meaning that the only significant effect from the pulsed lens is the detuning of the betatron tune with longitudinal amplitude J_z. The detuning of the synchrotron tune can be ignored in comparison. For a pulsed lens the total tune spread at any given moment within a single synchrotron period is given as:

$$\Delta Q(J_z, \varphi)/\Delta Q_{\text{max}} = I_0^{(e)}\left(\frac{J_z}{2\varepsilon_z} \frac{\sigma_z^2}{\sigma_e^2} \right) + 2\sum_{n=1}^{\infty} I_n^{(e)}\left(\frac{J_z}{2\varepsilon_z} \frac{\sigma_z^2}{\sigma_e^2} \right) \cos(2n\varphi), \quad (2.56)$$

where $I_n^{(e)}(u) = e^{-u} I_n(u)$ is the exponentially scaled modified Bessel function of the first kind. This has a static and a dynamic part, later we will show that the first one leads to Landau damping and the other one is equivalent to a higher order chromaticity effect. We can write the effective detuning term, as an exponentially scaled modified Bessel function, after averaging over the synchrotron phase φ

$$\langle \Delta Q(J_z) \rangle_\phi / \Delta Q_{\text{max}} = \exp\left(-\frac{J_z}{2\varepsilon_z} \frac{\sigma_z^2}{\sigma_e^2} \right) I_0\left(\frac{J_z}{2\varepsilon_z} \frac{\sigma_z^2}{\sigma_e^2} \right) = I_0^{(e)}\left(\frac{J_z}{2\varepsilon_z} \frac{\sigma_z^2}{\sigma_e^2} \right), \quad (2.57)$$

where $\langle \Delta Q(J_z) \rangle_\phi$ indicates average value over φ. The limiting cases are $\frac{\sigma_z}{\sigma_e} \ll 1$ and $\frac{\sigma_z}{\sigma_e} \gg 1$. For $\frac{\sigma_z}{\sigma_e} \ll 1$, than all dynamics terms are zero and $\Delta Q \approx \Delta Q_{\text{max}}$. This is a DC EL limit. For $\frac{\sigma_z}{\sigma_e} \gg 1$, than the static part goes to zero, and we have only influence from higher harmonics of $\cos\varphi$. PEL range of parameters are in fact for a $\sigma_e \approx \sigma_z$, meaning that we have both static and dynamic terms contributing significantly to the dynamics.

In conclusion, this short derivation demonstrates that the main effect from a pulsed electron lens kick is longitudinal detuning, detuning with longitudinal amplitude J_z and longitudinal phase φ.

2.3.4 Wakefield

Wakefields describe the interaction between the beam and its environment (beam pipe, cavities, etc) via electromagnetic interaction. Two approximations are necessary for the present explanation. In the rigid beam approximation, the beam travels through the vacuum chamber rigidly and the wakefield does not affect this rigidity in a single revolution turn.

In the impulse approximation, particles motion can be described via impulse. This is necessary because the electromagnetic fields $\vec{E}$, $\vec{B}$ are more difficult to compute. The impulse received from the electromagnetic field can be expressed as

$$\Delta \vec{p} = \int_{-\infty}^{\infty} \vec{F} \mathrm{d}r, \tag{2.58}$$

where $\Delta \vec{p}$ is the impulse the particle receives; $\vec{F} = e(\vec{E} + \vec{v} \times \vec{B})$ is the Lorentz force.

Through the Panofsky-Wentzel theorem [43], [92] the computation of the impulse can be performed. The decomposed into two directions (parallel to z and perpendicular to s) form of the theorem reads as [43]:

$$\nabla \cdot (\vec{e}_s \times \Delta \vec{p}) = 0, \tag{2.59}$$

$$\frac{\partial}{\partial z} \Delta \vec{p}_\perp = (\nabla_\perp \cdot \Delta p_s), \tag{2.60}$$

where p is the particle momentum; $\Delta \vec{p}_\perp$ is the projection of the momentum on the transverse plane; Δp_s is the momentum component in the s direction; ∇ is the nabla operator and $\nabla_\perp$ is the nabla operator only taking the derivatives in the transverse plane.

For example for a cylindrical beam pipe the components of the impulse are expressed as

$$v \Delta \vec{p}_\perp = -q M_m W_m(z) m r^{m-1} [\vec{e}_r \cos(m\theta) - \vec{e}_\theta \sin(m\theta)], \tag{2.61}$$

$$v \Delta p_s = -q M_m W_m'(z) r^m \cos(m\theta), \tag{2.62}$$

where r, θ are the cylindrical coordinates; q is the charge of the source particle; M_m is the mth multipole moment of the source particle; m is the azimuthal number; W_m' is the longitudinal wake function of azimuthal m; W_m is the transverse wake function of azimuthal m. An example of a wakefield is illustrated in Fig. 2.6.
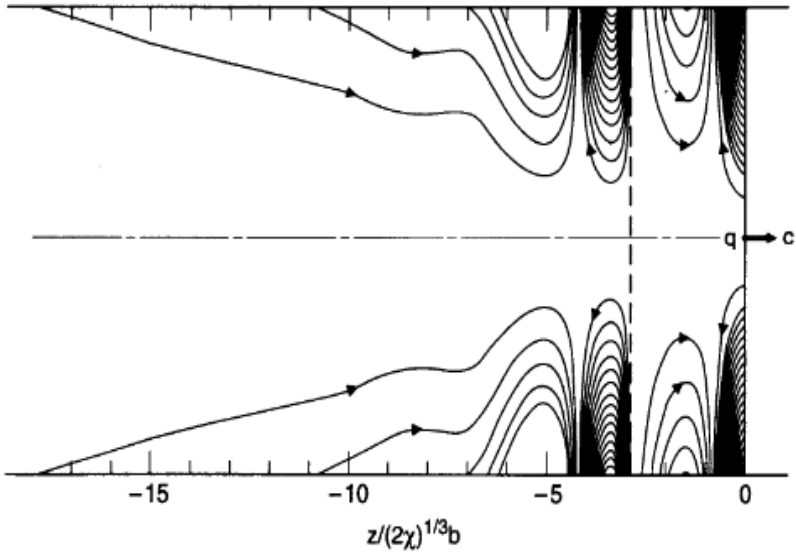
Figure 2.6: Illustration of a wakefield generated by a single particle with a charge q inside a resistive beam pipe. Picture is taken from [92], where the wakefield was computed. $z/(2\chi)^{1/3}b$ is a measure of distance from the source particle.

The following relationship between transverse and longitudinal wakefields is a consequence of Panofsky-Wentzel theorem

$$W'_m(z) = -\frac{\mathrm{d}}{\mathrm{d}z}W_m(z), \tag{2.63}$$

where m is the azimuthal number; W'_m is the longitudinal wake function of azimuthal m; W_m is the transverse wake function of azimuthal m. In this work we would only be interested in the *dipolar transverse impedance*, the resulting force from a wakefield can be expressed as [93]

$$
\begin{aligned}
F_y^{\mathrm{coh}}(z,t) \quad = \quad & \frac{q^2}{2\pi R} \iint\limits_0^\infty \sum_{k=-\infty}^{\infty} \mathrm{d}z' \mathrm{d}\delta' W_y(z' + 2\pi kR - z) \\
\times \quad & \iiiint \mathrm{d}J'_x \mathrm{d}\theta'_x \mathrm{d}J'_y \mathrm{d}\theta'_y \Psi\left(J'_x, \theta'_x, J'_y, \theta'_y, J'_z, \varphi', t-k\right) \sqrt{2J'_y \beta_y} \sin \theta'_y,
\end{aligned}
\tag{2.64}
$$

where $F_y^{\mathrm{coh}}(z,t)$ is the force for a particle at longitudinal position z at time t; k is the number of revolution turns; Ψ is the particle distribution in 6D phase space; W_y is the transverse vertical dipolar wakefield ($m = 1$).

2.3.5 Beam coupling impedance

Wakefield expressed in the frequency domain is referred to as *beam coupling impedance*:

$$Z_m^{\parallel}(\omega) = \int_{-\infty}^{\infty} e^{j\omega/v} W_m'(s) \frac{\mathrm{d}s}{v_0}, \tag{2.65}$$

$$Z_m^{\perp}(\omega) = \frac{j}{\beta_r} \int_{-\infty}^{\infty} e^{j\omega/v} W_m(s) \frac{\mathrm{d}s}{v_0}. \tag{2.66}$$

In this work we are only interested in transverse beam coupling impedance, that will drive transverse instabilities. The transverse impedance would have the following properties[43]:

1. Because wake-function are real-valued functions: $Z_m^{\perp}(-\omega) = [Z_m^{\perp}(\omega)]^{\dagger 1}$.

2. $Z^{\perp}$ is analytic with only poles in the lower half ω-plane.

3. The energy of the particle cannot be increased without any accelerating forces: $\Re Z_m^{\perp} \geq 0$ if $\omega > 0$, if the beam pipe has the same cross section at the entrance and at the exit.

4. From $W_m(0) = 0$ follows that $\int_0^{\infty} \Im Z_m^{\perp}(\omega) \mathrm{d}\omega = 0$.

One of the sources of impedance in an accelerator is resistive beam pipe, referred to as *resistive wall impedance*. The resistive wall dipolar impedance of a circular beam pipe can be expressed as [92][2]

$$Z_1^{\perp}(\omega) = Z^{\perp}(\omega) = [1 - j\,\mathrm{sgn}(\omega)] \frac{cL\rho}{\omega\pi b^3 \delta_{\mathrm{skin}}} \tag{2.67}$$

where $\delta_{\mathrm{skin}} = \sqrt{\frac{2\rho}{\mu_r \mu_0 \omega}}$ is the skin depth at frequency ω; μ_0 is the vacuum permeability; μ_r is the relative permeability; L is the length of beam pipe with the resistive wall; b is the radius of the beam pipe; ρ is the conductivity of the beam pipe material.

---

1    $a^{\dagger}$ denotes complex conjugate of a.

2   This formula is only valid if the wall thickness t is much larger than the skin depth δ_{skin}.

In a real accelerator there are many sources of beam coupling impedance and the wakefields: resistive wall beam pipe, cavities, belows, etc. The influence of the wakefield on the beam will scale with Twiss beta function. Therefore, *total machine impedance* can be defined as a Twiss beta function weighted sum of all impedance sources in the machine:

$$Z_{\text{machine}}(\omega) = \frac{\sum_i \hat{\beta}_{x,y} Z_i(\omega)}{\overline{\hat{\beta}}_{x,y}}. \tag{2.68}$$

2.3.6 Transverse instabilities

Beam coupling impedances add an external force that acts on a beam and depends on its particle distribution in the phase space Ψ. We would define an *instability* as a situation when one or more momenta of the beam distribution (beam offset, transverse or longitudinal rms beam size, etc.) increases exponentially. In this work we only study transverse instabilities, related to the transverse particle distribution momenta. In particular, this work deals with transverse beam offset stability. The transverse offset can be driven to be unstable, for example, by a dipolar transverse impedance. Transverse instabilities limit the maximal achievable beam intensity. For a recent overview of transverse and longitudinal instabilities in hadron synchrotrons we would direct the reader to [42].

The transverse instabilities can be characterised in several different ways. One is to distinguish bunched beam and coasting (unbunched) beam instabilities, the difference between them is often due to the synchrotron motion. Another one is to separate bunched beam instabilities into single-bunch and multibunch instabilities. We would consider only two specific transverse instabilities: coasting beam instability due to a resistive wall impedance; head-tail instability, which is a single bunch instability that occurs for nonzero chromaticity.

2.3.7 Resistive wall coasting beam instability

Coasting beam occupies the whole circumference of the ring, and thus, we can describe it with just the transverse coordinates (x, p_x, y, p_y), momentum offset $\Delta p/p_0$, position along the ring s and the time t taken in turns. For the study of dipolar transverse instabilities we are interested in transverse beam offsets $\langle x \rangle(s, t)$, $\langle y \rangle(s, t)$. For coasting beam case we can use the following ansatz for the beam offset:

$$\langle y \rangle(s, t) = \sum_{n=0}^{\infty} \frac{eN\Delta_y}{C} e^{j(ns/R - Q_{\text{coh}} t)}, \tag{2.69}$$

where e is the elementary electric charge; Δ_y is the maximum vertical amplitude; N is the number of particles in the beam; C is the circumference of the accelerator; $R = C/(2\pi)$ is the effective radius of the accelerator; n is the mode number; Q_{coh} frequency of the coherent oscillations (in turns).

The equation of motion in y-plane is a driven harmonic oscillator:

$$\ddot{y}(s,t) + Q_y^2 y(s,t) = \frac{F(s,t)}{\gamma_r m} = \frac{j e v \beta_r}{\gamma_r m C} Z_1^\perp(Q_{\text{coh}}) \langle y \rangle (s,t). \tag{2.70}$$

This equation will have the following solution:

$$\left[Q_y^2 - (Q_{\text{coh}} - n)^2 \right] y(s,t) = \frac{j e^2 N c Z_1^\perp(Q_{\text{coh}}) \Delta_y}{E_0 T_0^2} e^{jnS/R - j(Q_{\text{coh}} - n)t}. \tag{2.71}$$

From the self-consistency we can obtain a dispersion relation:

$$1 = \frac{j e^2 N c Z_1^\perp(Q_y)}{E_0 T_0^2} \int dQ_y \frac{\psi(Q_y)}{\left[Q_y - (Q_{\text{coh}} - n) \right]^2}, \tag{2.72}$$

where the betatron frequency distribution is denoted as $\psi(Q_y)$.

We can assume that the coherent tune shift due to the wakefield is $Q_{\text{coh}} \approx Q_y + n$, meaning that the instability is close the one of the beam modes. Then, we can classify the beam modes in the following way: $n > 0$ will be fast waves, $n < 0$ will be slow waves, with specifically $|n| < Q_y$ be referred to as backward waves. This classification is due to a comparison of the wave frequency to the frequency of the angular phase:

$$Q_{\text{ang}} = 1 + Q_y/n, \tag{2.73}$$

fast waves travel faster than the revolution frequency, slow waves travel slower than the revolution frequency, and backward waves travel in the opposite direction.

Since $\Delta Q_{\text{coh}} \propto -j Z_1^\perp(Q_y + n)$, for an instability we would need negative real part of the impedance $\Re Z_1^\perp(Q_y + n) < 0$. Due to the properties of the wakefield and beam-coupling impedances (see Section 7.1), the real part of the impedance is only negative for negative frequencies. This means that in coasting beam case only slow waves (with $|n| > Q_y$) can be driven to an instability by a beam coupling impedance. The fast waves and backward waves are not excited by the wakefield. However, those are the eigenmodes of the beam and can be excited and even be unstable.

In our work, related to the coasting beam, the betatron frequency will depend on the momentum offset δ (for example, from chromaticity and momentum compaction factor) and on the transverse amplitudes (J_x, J_y) (for example, from space-charge and DC electron lens or octupole magnets). Let us here consider only the momentum spread
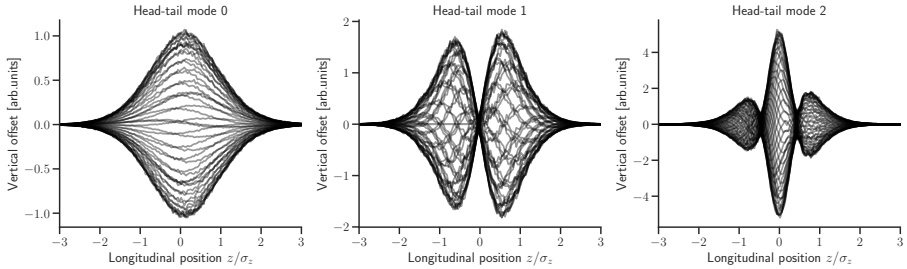
Figure 2.7: Examples of a head-tail instabilities observed in the simulation for several chromaticity values. Each curve corresponds to an intrabunch offset during one turn. Curves for several consecutive turns are superimposed on each other to produce a stroboscopic plot.

contributions, because, in the case of DC electron lens and space-charge, the transverse amplitude contribution will be significantly smaller. Then, we can write the betatron tune spread as

$$\Delta Q_y = \xi_y Q_y - (n + Q_y)\eta, \tag{2.74}$$

where ξ_y is the normalised vertical chromaticity and η is the slip factor. The contribution of the slip factor is due to particles with positive momentum offset have a smaller revolution frequency for accelerator above transition ($\eta > 0$). Landau damping becomes stronger for larger tune spreads, consequently different modes n of the coasting beam will be damped differently.

For the slow wave modes $n < 0$ and $|n| < Q_y$ and an accelerator below transition energy at natural (negative) chromaticity we will have: $\xi_y Q_y < 0$ and $-(n + Q_y)\eta < 0$, where both the chromaticity and the slip factor contribute to the increase of the momentum spread. In this case, the beam will naturally have some stabilisation due to Landau damping. If one wants to excite an instability, this could be achieved by shifting chromaticity to a positive value, such that $\Delta Q_y \approx 0$. For SIS18, with $\eta = -0.93$, $Q_y = 3.27$ and a first slow wave, driven by a wakefield $n = 4$, the compensated chromaticity would be $\xi \approx 0.21$.

For the fast wave modes $n > 0$ and an accelerator below transition energy at natural chromaticity we will have: $\xi_y Q_y < 0$ but $-(n + Q_y)\eta > 0$. In this situation, the chromaticity and momentum offset are counteracting each other, for a certain mode number n, the Landau damping will be minimal. Let us consider SIS18 as an example with $\eta = -0.93$, $Q_y = 3.27$ and $\xi_y Q_y = -5.6$. Then, $\Delta Q_y = -5.6 + 0.93(n + 3.27)$ will clearly be minimal for $n = 3$ at the natural chromaticity.

2.3.8 Transverse head-tail instability

In this work, we are concerned with the head-tail instability. This is a transverse single bunch instability that is observed or expected in many synchrotrons.
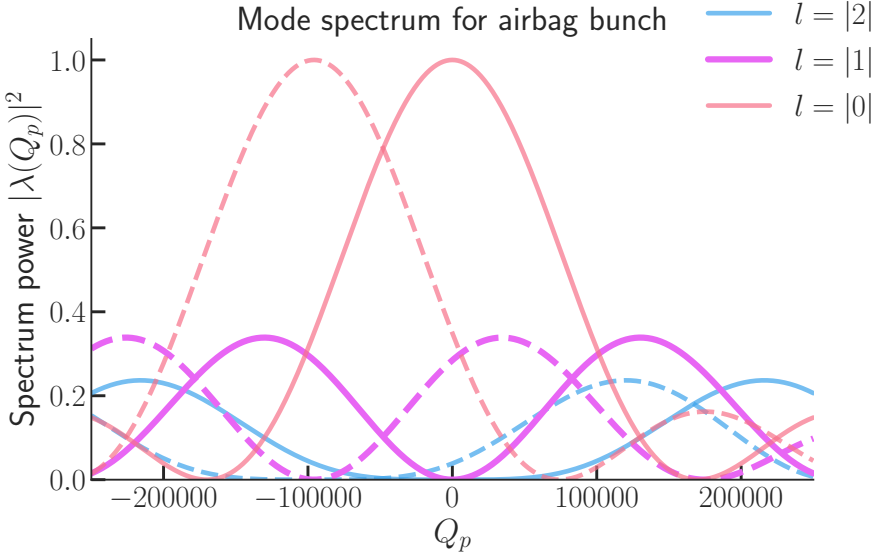
Figure 2.8: Head-tail mode spectrum (taken for an airbag bunch) with zero chromaticity (solid lines) and nonzero linear chromaticity (dashed lines). First three head-tail modes are demonstrated.

The detailed derivations and explanations of head-tail instability can be found in standard accelerator physics textbooks [43], [92]. We would only provide and interpret results of these derivations here and in Chapter 5 we would give a detailed solution for Landau damping of a head-tail instability where the betatron frequency detuning is present.

Let us assume the form of the perturbation to the distribution function

$$\Psi(J_x, \theta_x, J_y, \theta_y, J_z, \phi; s) = \Psi_0(J_x, J_y, J_z) + \Psi_1(J_x, \theta_x, J_y, \theta_y, J_z, \phi)e^{-j\Omega s/v}, \qquad (2.75)$$

where Ω is the frequency of the coherent transverse oscillations.

Figure 2.7 demonstrates examples of a transverse offset along the bunch length of an unstable bunch for several head-tail modes. The head-tail mode can be characterised by a number of "knots", by the frequency of oscillations and an instability growth rate.

Figure 2.8 demonstrates the head-tail mode spectrum for a specific longitudinal distribution – an *airbag bunch*. An airbag bunch is a simplification of a real bunch longitudinal distribution. In an airbag bunch all the particles have the same longitudinal amplitude J_z. The effect of the linear chromaticity on the spectrum of the head-tail modes will remain the same for other longitudinal distributions. In Fig. 2.8 the spectrum is shown to be shifted by the linear chromaticity by a chromatic frequency $\omega_{\xi^{(1)}} = Q_{x,y} \omega_0 \xi^{(1)}/\eta$. The mode spectrum shape remains unperturbed and the azimuthal modes $l = \pm n$ (where n is an arbitrary integer) are degenerate.

It is useful to define *effective impedance* of a given head-tail mode:

$$Z_{\text{eff}} = \frac{\sum_{p=0}^{\infty} Z_y(\omega)|\lambda(\omega)|^2}{|\lambda(\omega)|^2}, \tag{2.76}$$

where $|\lambda(\omega)|^2$ is the spectral power of a given mode. The effective impedance describes the interaction between the machine impedance and the beam mode spectrum. The instability growth rate and coherent frequency of oscillations are related to this quality.

In the absence of chromaticity, the mode spectrum is an even function $\lambda(\omega) = \lambda(-\omega)$. From the impedance property 1 in Subsection 2.3.5 we can make conclusion about the real and imaginary part of the effective impedance. The real part of the impedance is an odd function $\Re Z^{\perp}(\omega) = -\Re Z^{\perp}(\omega)$, so the real part of the effective impedance would be zero $\Re Z_{\text{eff}} = 0$. The imaginary part is an even function of ω, $\Im Z^{\perp}(\omega) = \Im Z^{\perp}(-\omega)$, so the effective impedance would be nonzero $\Im Z_{\text{eff}} \neq 0$. For the zero chromaticity, there is no instability until the effective impedance will couple two neighbouring modes. When the chromaticity is not zero, as in Fig. 2.8 (dashed lines), the mode spectrum is no longer an even function of the frequencies. Therefore, an instability with a certain growth rate will develop for nonzero chromaticity. Depending on the impedance and the sign of the chromaticity, different modes can become unstable.

2.4 Landau Damping and other instability mitigation measures

There are several ways to mitigate or suppress beam instabilities in an accelerator (for an overview see [70]). In the case of a head-tail instability those include: transverse feedback system [82], chromaticity adjustment and Landau damping [70]. Adjusting chromaticity with the sextupole magnets is not always possible because strong nonlinear magnetic fields significantly reduce single particle stability. Transverse feedback systems are usually operating in a narrowband frequency range. If the tune shift of the instability is known one can design a transverse feedback system that will help damp the instability. Landau damping on the other hand is a passive mitigation measure that requires a betatron frequency spread in the bunch. For many accelerators these and other mitigation measures are combined with each other.
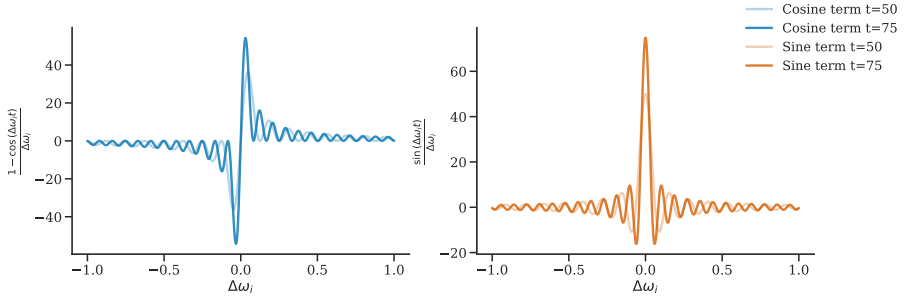
Figure 2.9: Time dependent integrated functions for cosine (left, blue) and sine (right, orange) terms of the beam offset in Eq. (2.79) for two different times. The frequency distribution was assumed to be uniform $\rho(\omega_i) = 1$.
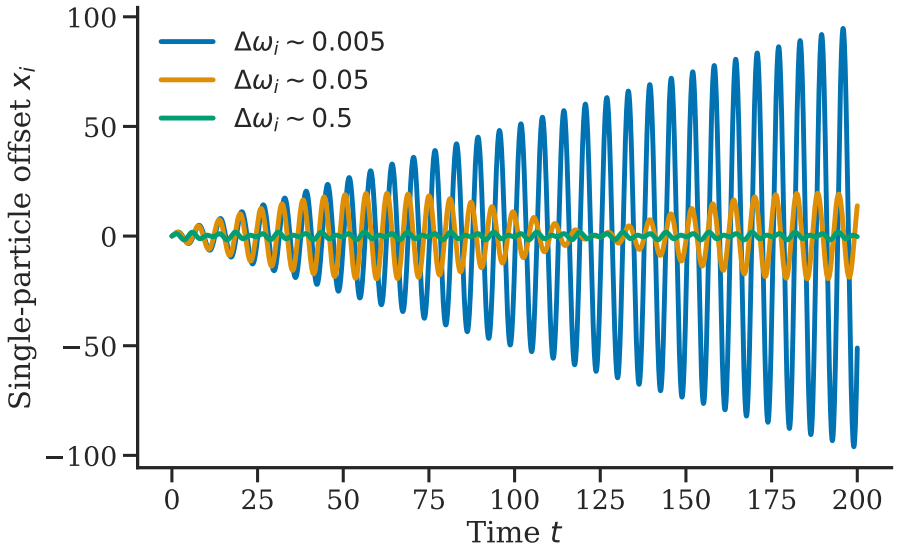
Figure 2.10: Single particle offset for three different particles: one had a natural frequency very close to the frequency of the driving force; another a close frequency; and a third one a frequency far from the frequency of the driving force.

Landau damping was first conceived analytically by L. D. Landau [58] and later confirmed in the experiments [94]. For particle accelerators Landau damping was first

studied for longitudinal instabilities in [95] and for transverse instabilities in [96] for a coasting beam and in [97] for bunched beam. In the present time, Landau damping is used or considered in many synchrotrons as a transverse instability mitigation measure.

The following explanation will largely follow the one from textbooks [43], [92]. To explain the effect of Landau damping let us consider a simple analytical problem: a set of harmonic oscillators (with natural frequencies ω_i) driven by an external force F_{ext} with a frequency Ω

$$\ddot{x}_i + \omega_i^2 x_i = A \cos \Omega t, \tag{2.77}$$

where $\ddot{x}_i$ is the second derivative over time t; A is the amplitude of the driving force; ω_i is the eigenfrequency of the particle i; Ω is the frequency of the driving force. For a single particle i, the general solutions is

$$x_i = x_{\text{init}} \cos \omega_i t + \dot{x}_{\text{init}} \frac{\sin \omega_i t}{\omega_i} + \frac{A}{\omega_i^2 - \Omega^2}(\cos \Omega t - \cos \omega_i t). \tag{2.78}$$

For the discussion of Landau damping the initial conditions could be chosen to be $x_{\text{init}} = \dot{x}_{\text{init}} = 0$. We are interested in a beam offset $\langle x \rangle$, so we need to integrate over the particle distribution by frequency $\Psi(\omega)$. Additionally, let us assume that all natural frequencies ω_i are close to the frequency of the driving force Ω ($|\Delta \omega_i| = |\omega_i - \Omega| \ll 1$). In a synchrotron it means that the frequency of the driving force will be close to the frequency of the betatron oscillations. Then, one obtains:

$$\langle x(t) \rangle = \frac{-A}{2\Omega} \left(\cos(\Omega t) \text{P.V.} \int \frac{1 - \cos \Delta \omega_i t}{\Delta \omega_i} d\omega_i + \sin(\Omega t) \int \frac{\sin \Delta \omega_i t}{\Delta \omega_i} d\omega_i \right), \tag{2.79}$$

where P.V. denotes that a principal value of the integral is taken. Figure 2.9 demonstrates that the offset from Eq. (2.79) is stable.

On the left of Fig. 2.9 a function $\frac{1 - \cos \Delta \omega_i t}{\Delta \omega_i}$ is plotted in blue. On the right – $\frac{\sin \Delta \omega_i t}{\Delta \omega_i}$ in orange. On a long timescale $t \to \infty$, these functions have the following limits:

$$\lim_{t \to \infty} \left(\frac{1 - \cos \Delta \omega_i t}{\Delta \omega_i} \right) = 1/\Delta \omega_i, \tag{2.80}$$

$$\lim_{t \to \infty} \left(\frac{\sin \Delta \omega_i t}{\Delta \omega_i} \right) = \pi \delta_D(\Delta \omega_i), \tag{2.81}$$

where $\delta_d(\omega)$ is Dirac delta function. In terms of the exponent the beam offset $\langle x(t) \rangle$ for $t \to \infty$ can be expressed as:

$$\langle x(t) \rangle = -\langle x(t) \rangle \frac{\tilde{A} e^{j\Omega t}}{2\Omega} \int \frac{\rho(\omega_i)}{\omega_i - \Omega} d\omega_i, \tag{2.82}$$

where $\Im\Omega > 0$ would indicate an instability. Thus, we conclude that the beam offset will stay stable.

In order to answer why the beam offset stays stable in this system, we can look at two particles: one with exactly the frequency of the driving force $\omega_i = \Omega$; another with the frequency close to Ω. In Fig. 2.10 single particle offsets are shown for three different particles. Each has a frequency separated from the frequency of the driving force by the values of $\{0.005, 0.05, 0.5\}$. The amplitude of the particles with frequency closest to the driving force frequency grows linearly. Particles with larger frequency detuning may grow linearly initially but afterwards their amplitudes decrease. In the long-term, only the particles with exactly the frequency Ω will continue to grow in amplitude.
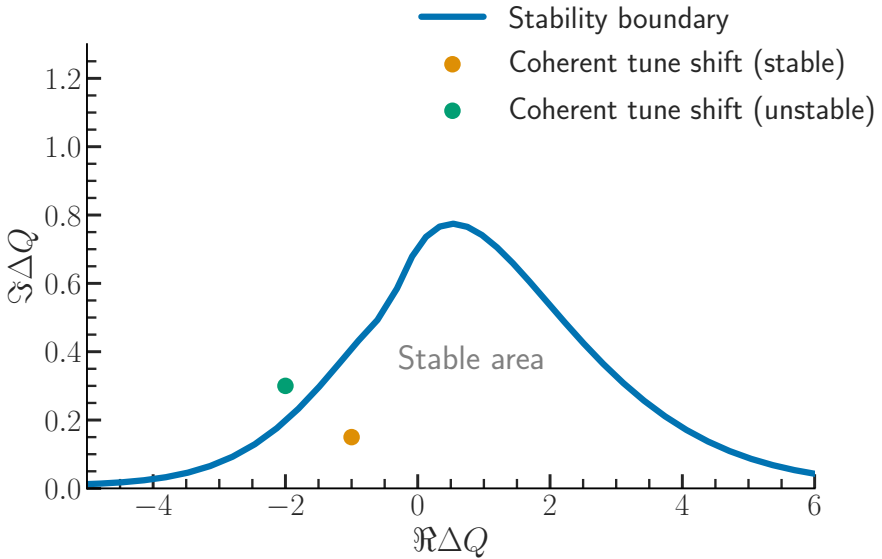
Figure 2.11: Illustration of a stability boundary (blue curve) in the complex coherent tune shift space. An example is given for a stable (orange dot, below the stability boundary) and unstable (green dot, above the stability boundary) coherent tune shift.

In a particle accelerator, for a wakefield driven instability we have a force proportional to the beam offset: $A = \tilde{A}\langle x(t)\rangle$. For a certain number of frequencies defined by a *dispersion relation* Eq. (2.82) the beam will stay stable. We can add that the crucial ingredient of Landau damping is having the frequency of the *coherent* oscillations (oscillations of the beam offset) inside the *incoherent* frequency spread of individual particles.

The dispersion relation in a case of a coasting beam and frequency detuning with transverse amplitudes (J_x, J_y) takes the following form:

$$\Delta Q^{-1} = \frac{1}{N} \int \frac{\frac{\partial \Psi_0}{\partial J_y} J_y \mathrm{d}J_x \mathrm{d}J_y \mathrm{d}J_z}{Q_{\mathrm{coh}} - Q_{y_0} - \Delta Q_y^{\perp}(J_x, J_y)}. \tag{2.83}$$

The dispersion relation in a case of a bunch with only a frequency detuning with transverse amplitudes takes the following form:

$$\Delta Q^{-1} = \frac{1}{N} \int \frac{\frac{\partial \Psi_0}{\partial J_y} J_y \mathrm{d}J_x \mathrm{d}J_y \mathrm{d}J_z}{Q_{\mathrm{coh}} - Q_{y_0} - \Delta Q_y^{\perp}(J_x, J_y) - l Q_{s_0}}, \tag{2.84}$$

where the normalisation is $N = \int \frac{\partial \Psi_0}{\partial J_y} J_y \mathrm{d}J_x \mathrm{d}J_y \mathrm{d}J_z$. Both dispersion relations are similar and describe the Landau damping from octupole magnets on the coherent beam stability.

The solution to the dispersion relation can be represented as a stability diagram. Figure 2.11 describes a stability diagram due to Landau damping. The diagram is plotted in the coordinates of the instability coherent tune shift in the absence of Landau damping (arb. units). The complex plane of coherent instability tune shifts is divided into a stable and an unstable areas by a stability boundary (blue curve). The shape and size of the stability boundary would depend on the betatron frequency detuning and on the particle distribution function.

3 Simulation framework

3.1 Macroparticle models and PyHEADTAIL computer code

The motion of a single particle in the transverse and longitudinal planes was described in Chapter 2. Analytically, we can obtain information about the whole beam's average motion and the particle distribution's statistical momenta. In the case of instabilities, the most unstable modes can be obtained. Numerically, however, we can solve the single particle equations of motion and obtain the particle coordinates in phase space at any position s for each particle. Nevertheless, the number of particles in the accelerator is large $\approx 10^{10} - 10^{13}$, and solving the differential equations for each particle in the beam is impractical. Each turn in the accelerator can already involve many integration steps for particle tracking through the accelerator lattice and collective effects. In addition to the long computation time, this large number of particles could not be used due to the memory limitations in modern computing systems. Instead, a macroparticle approach can be used for numerical simulations.

The whole beam in the simulation is presented as an ensemble of $N_{\mathrm{m.p.}}$ macroparticles, typically a much smaller number than $N_{\mathrm{particles}}$. Each macroparticle represent a small ensemble of particles $N_{\mathrm{particles}}/N_{\mathrm{m.p.}}$ and has a charge of $ZeN_{\mathrm{particles}}/N_{\mathrm{m.p.}}$ and mass $Am_p N_{\mathrm{particles}}/N_{\mathrm{m.p.}}$. The number of macroparticles relative to the number of particles in a physical system is known as *granularity*. This is a purely numerical parameter, and, in general, the physical results should not depend on the choice of this parameter. If the results depend on the granularity, this is due to the numerical noise. When the numerical noise does not affect the simulation results, the macroparticle number *converges*. The number of macroparticles used for particular simulations is determined through a convergence study.

In this work we have used PyHEADTAIL macroparticle tracking code [98], successor of the HEADTAIL code [99]. PyHEADTAIL is an open-source tracking code specialising in the simulation of collective effects. In recent years, this code was used to conduct or verify many beam dynamics studies, for example, [34], [51], [100], [101]. In several studies, it was benchmarked against other tracking codes; for example, bimbim [102], and against other non tracking codes, for example, against a Vlasov solver DELPHI [83], [93]. We would emphasise that PyHEADTAIL code was used for the recent studies on Landau damping [71], [72], [80] with an RFQ. In this work, we have extended the PyHEADTAIL code to include modules describing the influence of a PEL and a DC EL on the beam. In the rest of this section, we will briefly summarise the relevant numerical models in PyHEADTAIL.
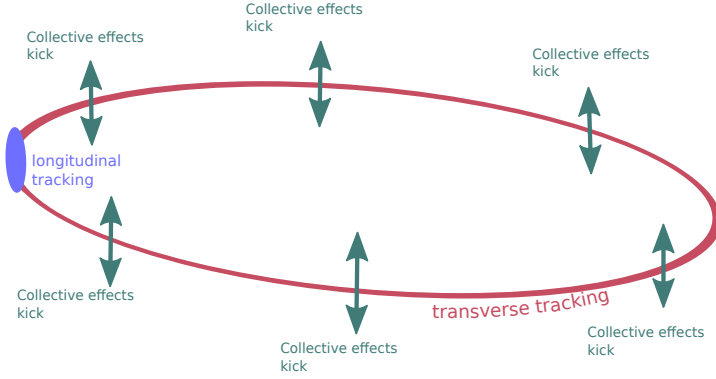
Figure 3.1: Schematic description of beam tracking in PyHEADTAIL code.

3.2 Wakefield models in PyHEADTAIL

Constant, dipolar and quadrupolar wakefields are implemented in the PyHEADTAIL tracking code. The wakefield can be passed to PyHEADTAIL as the data from a file, for example, obtained by a code calculating the wakefields or impedances Impedance-Wake2D [83]. Alternatively, several analytical wakefields are implemented in the code, for example, wakefield from a resistive wall or a resonator.

In order to properly simulate, without sacrificing computing efficiency, the wakefield interaction along the bunch, the bunch is represented by longitudinal slices. A slice is a collection of particles that are located between two longitudinal coordinates. Nearest grid point interpolation assigns a given particle to a given slice each turn (due to the synchrotron motion, the particles slowly rotate in the longitudinal phase space). Several slicing options are present in PyHEADTAIL. However, in this work, we only use slicing into uniform bins (equally spaced bins). If we count slices from tail to the head as $0, 1, ..i, ..N_{\text{slices}}$, the kick for the ith slice is

$$\Delta x_i' = \frac{q^2}{p_0 c} \sum_{j=i+1}^{N_{\text{slices}}} N_{\text{per slice}} W_x(z_j) \Delta x_j, \tag{3.1}$$

where $N_{\text{per slice}}$ is the number of macroparticles per slice. Figure 3.2 illustrates an example of a wakefield acting on the beam. The beam has a small transverse offset (orange dot) and the wakefield kick is shown after several revolution turns in the PyHEADTAIL simulations. Three numerical parameters need to be optimised by means of a conver-
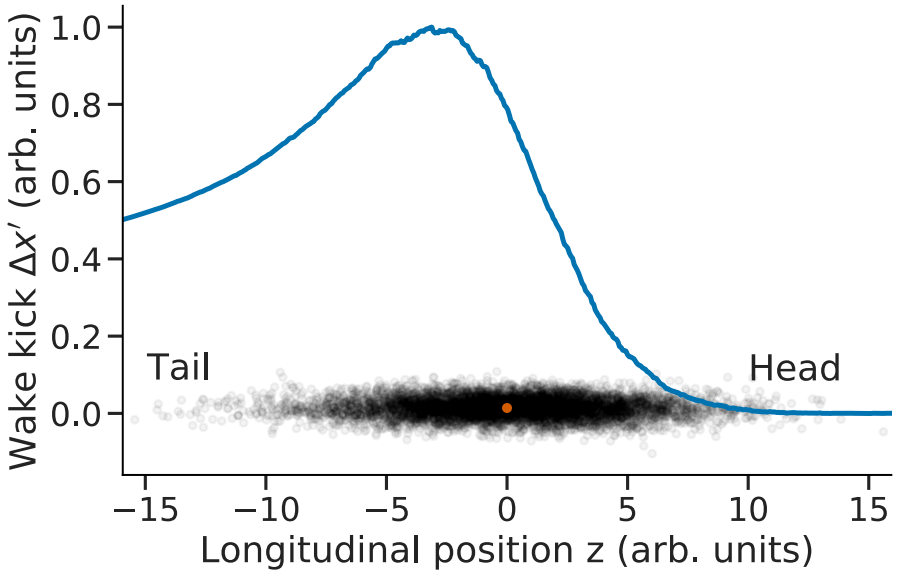
Figure 3.2: A schematic example of a simulated wakefield kick (in blue) acting on the beam (black dots) that has a small transverse offset.

gence study for the simulation of wakefields: the number of slices; the number of wakefield kicks per turn; the number of macroparticles in each slice. The accurate number of slices is necessary to resolve the intrabunch motion and its interaction with the wakefield. For the number of wakefield kicks per turn in the models used in this work, we always use only one wakefield kick per turn, using a total machine impedance. In the real accelerator, the wakefield is distributed along the ring, and the kicks occur at different positions. The number of macroparticles in each slice should be high enough to resolve the beam offset of each slice (in the case of a dipolar wakefield).
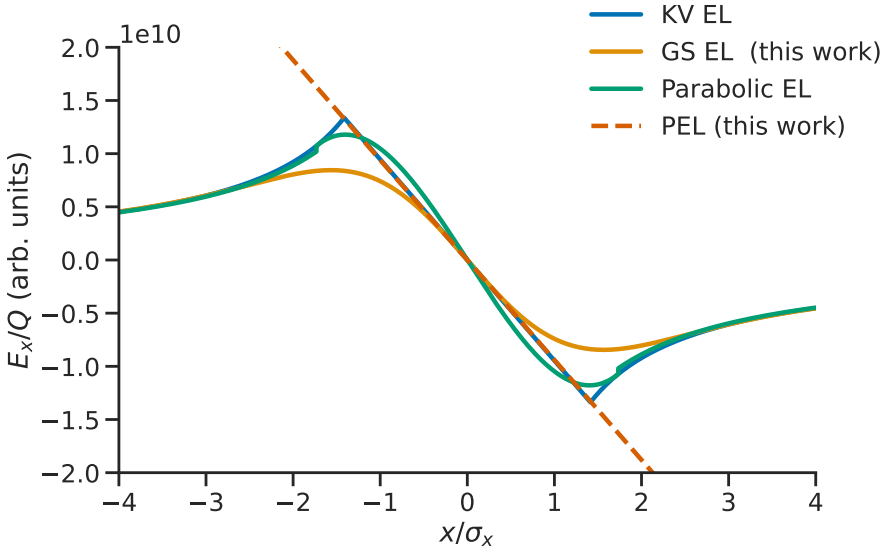
Figure 3.3: Electric fields (simulated) from different electron distributions of the electron lens beam as a function of transverse coordinate. For the homogeneous transverse electron distribution the electric field is depicted in blue. For the Gaussian distribution – in red. For the parabolic distribution – in green. For the PEL distribution used in this work – in dashed orange line.

3.3 Electron lens implementation

Electron lenses were not implemented in PyHEADTAIL, both PEL and DC EL were implemented in the code as a part of this work. The force of an electron lens, acting on a proton or heavy ion beam and assuming the beam centres coincide, is given by [77]

$$F(r_\perp) \propto E_{r_\perp}(r_\perp) \propto \frac{\int_0^{r_\perp} j_e(r'_\perp) r'_\perp \, dr'_\perp}{r_\perp}, \tag{3.2}$$

where $E_{r_\perp}(r_\perp)$ the electric field; $r_\perp = \sqrt{x^2 + y^2}$ is the distance from the centre of the beam; $j_e(r_\perp)$ is the electron current density. The electron current density depends on the transverse distribution of the electron beam. The compact expressions for electric fields for several transverse distributions can be found in [103], [104]. For a PEL, this current is additionally pulsed to match some longitudinal profile.
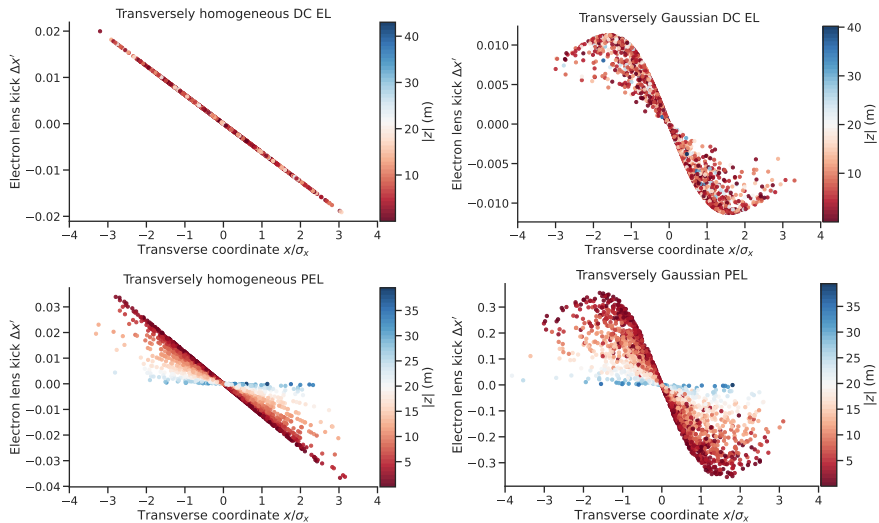
Figure 3.4: Kicks received by ion beam particles in the simulations from four different electron lens configurations. On the top row, DC EL with homogeneous transverse distribution (left) and Gaussian transverse distribution (right). On the bottow row, PEL with homogeneous transverse distribution (left) and Gaussian transverse distribution (right). The colour bar indicates magnitude of longitudinal position of a particle in the bunch.

In PyHEADTAIL, several transverse distributions for electron beam profile have been implemented: Gaussian, parabolic and homogeneous (Kapchinskij-Vladimirskij (KV) distribution). Figure 3.3 illustrates the electric field generated by these electron distributions for the particles located in the (longitudinal) centre of the bunch. A PEL in this work has a transverse distribution that covers the ion beam entirely. Hence, the electric field is always linear with the transverse coordinate. The longitudinal pulsing is achieved by dividing the bunch longitudinally into slices, similar to the wakefield. The current is given as a function of the longitudinal positions of the particles.

Figure 3.4 demonstrates the kicks received by an ion beam from different electron lenses in the PyHEADTAIL simulation after one revolution turn. The ion bunch has a transversely and longitudinally Gaussian distribution. Four cases are presented with a colour bar showing the longitudinal position of a particle inside the beam. The top row shows results for a DC EL. On the left, a DC EL with a homogeneous transverse distribution of electrons. On the right, with a transversely Gaussian distribution. The bottom row shows these transverse distributions but for a PEL. A PEL transverse electron distribution covers the ion beam entirely on the left. This is done to ensure that the

kick of a PEL always depends on the transverse coordinate linearly, ensuring that a PEL provides detuning only with longitudinal coordinates. On the right, a PEL transverse distribution has an equal to ion distribution transverse rms beam size. In Fig. 3.4, 50 slices are used for electron lens kicks. From Fig. 3.4 one can observe that for a PEL, the strength of the electric field depends on the longitudinal position. On the other hand, for a DC EL, there is no such dependency.

In all simulations in this work electron lens kick was used only once per revolution turn. Convergence studies showed no effect of increasing the number of kicks on Landau damping.

4 Experimental studies: Coasting beam instabilities in SIS18 with a DC electron lens

The experiments goal was to demonstrate and understand the influence of an electron lens on the beam stability in SIS18 at the injection energy. The goals of the experiment are helpful for understanding the effects of the proposed electron lens [35] in the SIS100 and of its prototype [59] to be installed in SIS18. The feasibility of Landau damping with an electron lens was investigated along with the instabilities, possibly induced by the electron lens. Throughout the experiments, an unbunched (coasting) [1] beam was used because instabilities with an unbunched beam were observed before in SIS18 [105].

4.1 Experimental setup

For the purpose of the experiment, an existing SIS18 electron cooler was used as an electron lens. This dedicated setup was achieved with the help of GSI beam cooling group. Figure 4.1 demonstrates the SIS18 lattice layout and some of the machine parameters.

During our beam time the following diagnostics equipment was used. Direct-current current transformer (DCCT) was used to monitor the beam current during the experiments. If the beam current is decreasing, we consider the beam losses to be observed. Beam position monitor (BPM) was used to measure the beam offset. When the beam offset is growing exponentially in time (linearly in the logarithmic scale), the beam experiences an instability. BPM is four conducting plates, two in the vertical plane and two in the horizontal plane. The difference of the signal between the two vertical plates is a measure of the vertical beam offset. In SIS18 there are 12 BPM that were used in our measurements. Ionisation Profile Monitor (IPM) was used to measure the beam size. IPM in SIS18 consists of 64 wires and a microchannel plate in front of them. The wires are spread out in the transverse plane. When a beam travels through an IPM it ionises residual gas. The residual gas than hits the microchannel plate. The plane emits electrons onto the wire array. The distribution of the electric charge on the wires corresponds to the ion beam charge density in the transverse plane.

An electron cooler (magenta colour) is located in section 10. The experiment was carried out with an unbunched (coasting) beam at the injection energy of 8.602[2]

---

[1]   With the RF cavities turned off the beam injected into SIS18 uniformly fills the ring.

[2]   This is lower than the nominal SIS18 injection energy of 11.4 MeV/nucleon due to technical reasons.
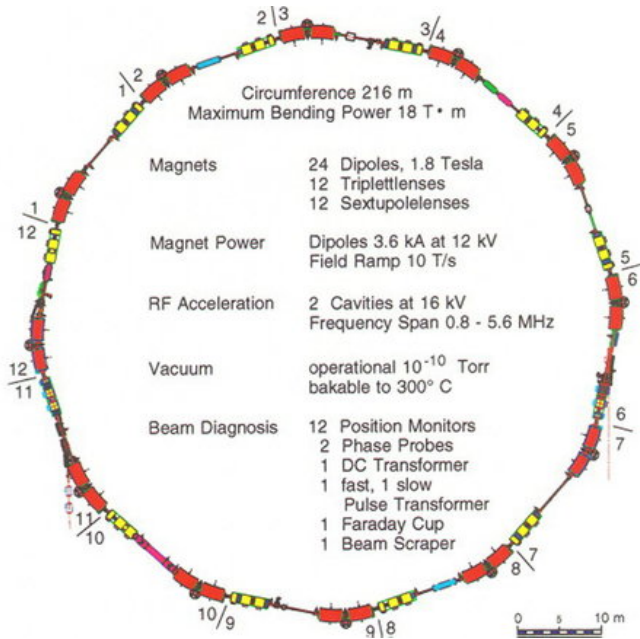
Figure 4.1: Schematic representation of the SIS18 heavy ion synchrotron. The electron cooler, used in our study as a non-linear electron lens, is located in section 10. The picture is adapted from [106].

MeV/nucleon. The beam was observed during the injection plateau for approximately 0.3 seconds. With the revolution frequency $f_{rev} = 186$ kHz this injection plateau corresponds to ≈ 55000 turns. Two different charge states of ^{40}Ar were studied in two separate experimental runs: one[3] with ^{40}Ar^{10+} and another[4] with ^{40}Ar^{18+}. The beam parameters during two experimental runs are summarised in Table 4.1.

Figure 4.2 demonstrates SIS18 cycle used in the experiments. An SIS18 cycle is a time frame between the bunch injection and extraction. Four beam current measurements of ^{40}Ar^{18+} are demonstrated as an example. A region where the beam current stays approximately constant, we will call a plateau. Grey lines indicate the injection plateau, where a coasting beam is stored in the SIS18, to be later bunched and accelerated to top energy. All measurements were done during the injection plateau with a coasting beam. The length of the injection plateau is approximately ≈ 0.3 seconds.

---

[3]   Data taken on 14/06/2021 and on 15/06/2021.
[4]   Data taken on 12/06/2021.

Ion	Parameter	Symbol	Units	Value
$^{40}\text{Ar}^{18+,10+}$	Intensity	N_b		$10^9 \dots 10^{10}$
$^{40}\text{Ar}^{18+,10+}$	Revolution frequency	f_{rev}	kHz	186
$^{40}\text{Ar}^{18+,10+}$	Injection energy	E_{inj}	MeV/nucleon	8.602
$^{40}\text{Ar}^{18+,10+}$	Tune	$Q_{x,y}$		4.32, 3.27
$^{40}\text{Ar}^{18+,10+}$	Chromaticity (natural)	$Q'_{x,y}$		$-4.1, -5.6$
$^{40}\text{Ar}^{18+}$	Horizontal rms emittance	ε_x	mm·mrad	25.7
$^{40}\text{Ar}^{18+}$	Vertical rms emittance	ε_y	mm·mrad	12.1
$^{40}\text{Ar}^{10+}$	Horizontal rms emittance	ε_x	mm·mrad	13.5
$^{40}\text{Ar}^{10+}$	Vertical rms emittance	ε_y	mm·mrad	6.1

Table 4.1: Ion beam parameters during the experiments with $^{40}\text{Ar}^{18+}$ and $^{40}\text{Ar}^{10+}$.
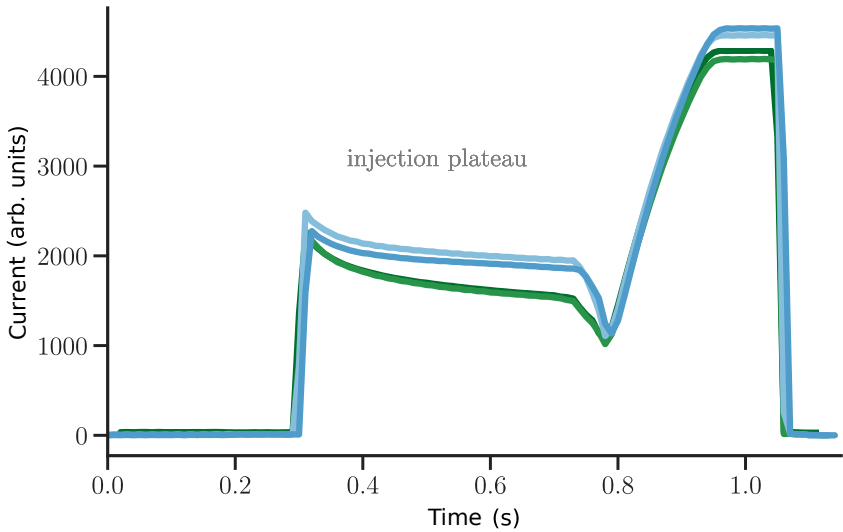

Figure 4.2: SIS18 cycle that was used in the experiments. Several different shots (measurements) are shown in different colours.

4.1.1 Electron cooler as a nonlinear lens

The parameters available from the electron cooler in SIS18 are summarised in Tab. 4.2. U_e and β_e are the electron beam kinetic energy and relativistic beta. f_{exp} is an adiabatic

expansion factor. The electron beam is assumed to be round with a radius a. The electron beam size a in the interaction region is governed by this adiabatic expansion factor as:

$$f_{\text{exp}} = \frac{a^2}{a_{\text{cath}}^2} = \frac{B_{\text{gun}}}{B_{\text{int}}},$$ (4.1)

where B_{gun} and B_{int} are the strengths of the magnetic field in the gun solenoid and in the interaction region solenoid, a_{cath} is the electron beam size at the cathode. It determines by how much the transverse size of the electron beam had increased compared to the beam size on the cathode (electron gun). The adiabatic expansion is achieved via varying strength of the solenoid magnetic field on the electron gun and in the interaction region solenoid magnet.

Parameter	Symbol	Units	Value
Kinetic energy	U_e	keV	6.6
Relativistic beta	β_e		0.16
Adiabatic expansion factor	f_{exp}		1 … 3
Interaction region length	L_e	m	2.8
Electron beam current	I_e	mA	0 … 900
Horizontal Twiss beta at cooler location	$\hat{\beta}_x$	m	10.9
Vertical Twiss beta at cooler location	$\hat{\beta}_y$	m	15

Table 4.2: SIS18 Electron cooler parameters. (Courtesy of GSI beam cooling group.)

For the electron cooler setup as a nonlinear lens, we should also consider the effect of residual gas ionisation and its interaction with the electron beam. This interaction can result in a beam-drift instability [107], where a slight separation of electron and ion beams will be exponentially amplified.

4.1.2 Accelerator and beam parameters during the experiment

Figure 4.3 demonstrates beam profiles measured with an IPM during the beam time with $^{40}\text{Ar}^{18+}$. The beam profiles in Fig. 4.3 were averaged over the whole injection plateau. The left part of the figure demonstrates the horizontal beam profile, and the right part — the vertical beam profile. Two cases are demonstrated for each transverse profile: beam profile with an electron cooler switched off and beam profile with an electron cooler current of 200 mA. No beam losses were observed for this setting of the electron cooler. The beam profiles for all four cases are fitted to a Gaussian to approximate the real transverse distribution and obtain the rms beam sizes. Compared with a Gaussian beam profile, the beam profile in SIS18 is not symmetric and has a longer "tail" on one side of the distribution. We can conclude that the electron cooler does not significantly modify

Parameter	Units		Value
Ion species		$^{40}\text{Ar}^{18+}$	$^{40}\text{Ar}^{10+}$
$\Delta\beta = \beta_e - \beta_i$		0.02	0.02
γ_e		1.012	1.012
U_e	keV	6.132	6.132
f_{exp}		3	3
I_e	mA	10	10

Table 4.3: Electron cooler parameters used to set it up as a non-linear electron lens. With the present settings no cooling effect was observed during the beam time. Identical settings of the electron cooler were used for two different charge states of ^{40}Ar.

Parameter	Units	IPM		Average		El. cooler	
		Ar^{18+}	Ar^{10+}	Ar^{18+}	Ar^{10+}	Ar^{18+}	Ar^{10+}
Hor. rms σ_x	mm	12.7	9.2	16.6	12	9.9	14.2
Vert. rms σ_y	mm	9.7	6.9	19.6	7.1	11.5	8.2
Hor. rms $\hat{\beta}_x$	m	7.8		8.2		10.9	
Vert. rms $\hat{\beta}_y$	m	6.3		10.7		15	

Table 4.4: Beam sizes on IPM, electron cooler and average in SIS18.

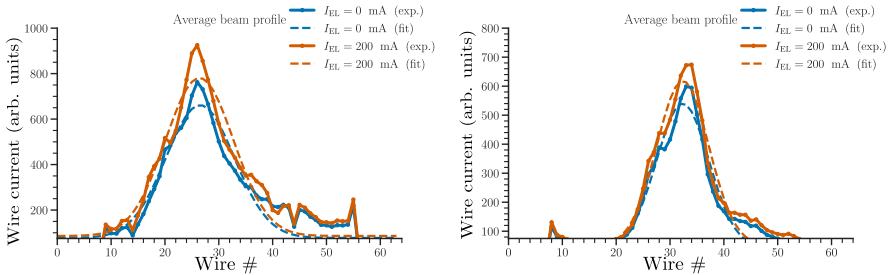**Figure 4.3:** Horizontal (left) and vertical (right) measured beam profiles (solid lines) and a Gaussian distribution fit (dashed lines). The distance between two neighbouring wires is 2 mm. Two measurements were taken: 1) Electron lens was off, 2) Electron lens was on with the current $I_e = 200$ mA.

the beam profile shape or the rms beam size. This observation is especially accurate for the vertical transverse beam profile.

For the beam time with $^{40}\text{Ar}^{10+}$, no dedicated measurement with IPM was made. Instead, the IPM recorded each shot's beam profiles. Then, the shots were sorted with respect to the observed beam losses. The shots with no beam losses were fitted to a Gaussian distribution to obtain an rms beam size. This way, more IPM data was stored for different shots and various electron beam currents I_e.

The measured and calculated beam sizes at several positions in the ring are shown in Table 4.4. The beam size on the IPM was measured. Than one can calculate rms emittance from $\sigma_{x,y} = \sqrt{\epsilon_{x,y} \hat{\beta}_{x,y}}$. The values of the emittance are invariant, Twiss beta function at the location of the IPM is known. The emittances were displayed in Table 4.1. Knowing the average beta function and the beta function at the position of the electron cooler, we can calculate the corresponding beam sizes.

Figure 4.4 demonstrates ion rms beam sizes on the injection plateau during the experiments as a function of time, for $^{40}\text{Ar}^{18+}$ on the left and for $^{40}\text{Ar}^{10+}$ on the right. The horizontal beam sizes are shown in blue and the vertical in orange. Different shots are indicated with the marker shape of the scatter plot. Solid horizontal lines indicate the average value over the injection plateau and over different shots. Figure 4.4 shows that the rms beam size (especially vertical one) was consistent over the injection plateau and shot-by-shot. Only the stable beam shots were considered for the beam size analysis.
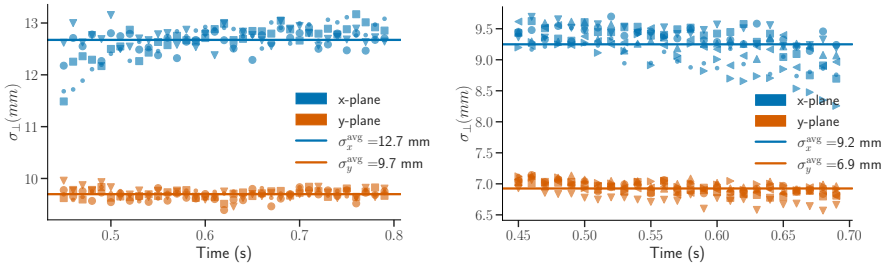
Figure 4.4: Ion beam sizes in the SIS18 during the injection plateau in experiments with $^{40}\text{Ar}^{18+}$ (left) and $^{40}\text{Ar}^{10+}$ (right). Vertical (orange colour) and horizontal (blue colour) rms beam sizes are displayed. Different shots are indicated via different markers (dots, triangles, squares, etc.). Only the shots with an observed stable beam were considered. The computed average values during the experiments are shown in solid lines.

4.2 Results of the experiment

The main experimental results were obtained with a BPM. The BPM characterises the beam envelope evolution during these losses, its growth time and the frequency of the

transverse oscillations. The signals were recorded from all of them for the entire beam time. During the postprocessing of the data, we identified that all of the BPMs yield equivalent signals. Here only the results from BPM number 1 are presented.

Additionally, the difference signals for vertical and horizontal planes were equivalent in the frequency domain. The signal from the BPM corresponded to a vertical instability, and the vertical difference signal was always stronger. Therefore, we would show and analyse only the vertical signals.

4.2.1 Results of the experiment with ^{40}Ar^{18+}

Shot	I_e (mA)	BPM Observation	Q'_y	Q'_x	τ (ms)	N
1.1	0	Stable beam	−5.6	−4.1		
1.2	0	Instability	0.	0.	92	11.5×10^3
1.3	0	Instability	0.	0.	92	11.5×10^3
1.4	0	Instability	0.2	0.15	68	8.5×10^3
1.5	200	Stable beam	0.2	0.15		
1.6	0	Instability	0.2	0.15	68	8.5×10^3
1.7	200	Stable beam	0.2	0.15		
1.8	100	Instability	0.2	0.15	68	8.5×10^3
1.9	160	Instability	0.2	0.15	100	12.5×10^3

Table 4.5: Instability observation and a reference observation of a stable beam for ^{40}Ar^{18+} in our experiment. For each instability we give a current of the electron cooler beam and growth rates in ms and in number of turns.

In Table 4.6 the results for several instabilities observed for ^{40}Ar^{18+} are summarised. The instability growth times were obtained by an exponential fit to the BPM data. The observed instabilities have growth times corresponding to $\approx 10 \ldots 100$ ms. For ^{40}Ar^{18+}, an electron cooler was used as an electron lens to stabilise the otherwise unstable beam.

Figure 4.5 demonstrates experimental data obtained from a BPM and the respective signals of the spectrum. In Fig. 4.5, Shots 1.1, 1.2, 1.3 from Table 4.5 are presented. The leftmost figures show the vertical difference signal obtained from the row data of the BPM. The middle figures show a zoomed-in vertical difference signal for one or a few revolution turns. The rightmost figure demonstrates a Fast Fourier transform (fft) spectrum of the vertical difference signal.

The top row of three figures represents the reference signal with natural chromaticity and electron cooler switched off. The amplitude of the difference signal from the BPM does not grow, and the spectrum of the signal remains dominated by the noise. We conclude that the beam remains stable during the injection plateau in the SIS18 at the natural chromaticity.

The two bottom figures demonstrate the same setting as the top row pictures, except the vertical and horizontal chromaticities, are changed to zero. From the BPM signal, one can conclude that the signal grows exponentially until turn number 20000. The growth time of the instability in both Shot 1.2 and Shot 1.3 are identical and equal to 92 ms or 11500 revolution turns. Therefore, the instability was reproduced for several shots. In the middle figures, we can observe that several oscillations occur within a single revolution turn. The fft spectrum of the unstable signal reveals that the instability has a broad spectrum of frequencies, including frequencies many times higher than the revolution frequency. The most unstable modes of this instability correspond to the fast waves of the coasting beam up to the 25th sideband of the revolution frequency.
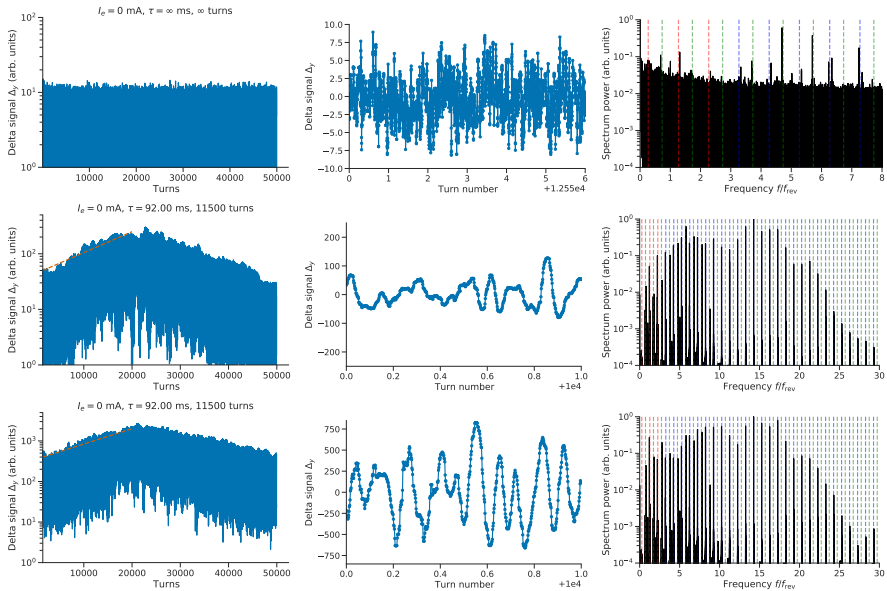
Figure 4.5: Experimental results from top to bottom of the image for Shots 1.1, 1.2, 1.3 (see Table 4.5). The electron cooler was switched off for all three shots. Shot 1.1 was taken at the natural chromaticity. For Shots 1.2, 1.3 the chromaticity was set to $Q'_{x,y} = 0$ in the control system. (Left) Raw BPM data. The delta signal for vertical plates is plotted in the logarithmic scale over the injection plateau in revolution turns. (Middle) BPM signal displayed for 6 consecutive turns, starting at turn 12500 for the top plot, and at 10000 for two bottom plots. (Right) FFT spectrum of the BPM signal. The dashed line illustrate the modes of the coasting beam oscillations (see Section 2.3.7): in purple fast waves, in green slow waves, in red (slow) backward waves.

The tune spread is zero when the tune spreads from chromaticity and the slip factor cancel each other. The chromaticity could be further changed (from zero) to correspond to a zero tune spread. For SIS18 this values were calculated to be $Q'_{x,y} = 0.15, 0.2$. The chromaticity in both vertical and horizontal planes is changed via sextupole magnets to correspond to this optimal value from Shots 1.4-1.9. This change should lead to stronger instability.
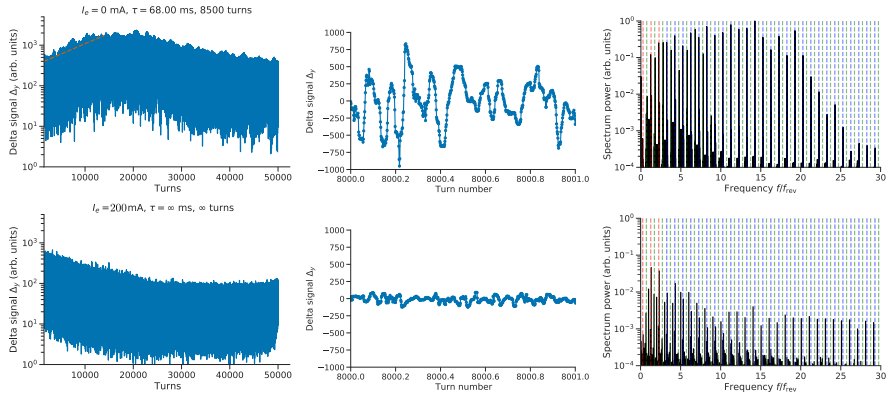

Figure 4.6: Experimental results from top to bottom of the image for Shots 1.4, 1.5 (see Table 4.5). (Left) Raw BPM data. (Middle) BPM signal showed for 6 consecutive turns from turn 12500 to turn 12506. (Right) FFT spectrum of the BPM signal. The dashed line illustrate the modes of the coasting beam oscillations (see Section 2.3.7): in purple fast waves, in green slow waves, in red (slow) backward waves.

Figure 4.6 demonstrates experimental data obtained for Shots 1.4, 1.5, top and bottom row of Fig. 4.6 respectively. In the top row, the electron cooler is switched off, and we observe an instability with a growth time of 68 ms. In the bottom row, only the setting of the electron cooler current was changed. This plot corresponds to an electron beam current of $I_e = 200$ mA. No instability is observed with an electron cooler turned on. This indicates that the electron cooler suppressed the instability in this case. One way an electron cooler can suppress the instability is via Landau damping.

Figure 4.7 demonstrates experimental data obtained for Shots 1.6-1.9. Shot 1.6 corresponds to the settings of Shot 1.4. We have an instability with a growth time of 68 ms for an optimal chromaticity setting $Q'_{x,y} = 0.15, 0.2$ and the electron cooler is switched off. Shots 1.7, 1.8, 1.9 correspond to the same setting and gradual increase of the electron beam current $I_e = 100, 160, 200$ mA. An increase in the electron beam current corresponds to the increase of the betatron tune spread from an electron cooler, associated with an increase in Landau damping. For the Shot 1.7 and $I_e = 100$ mA we observe the
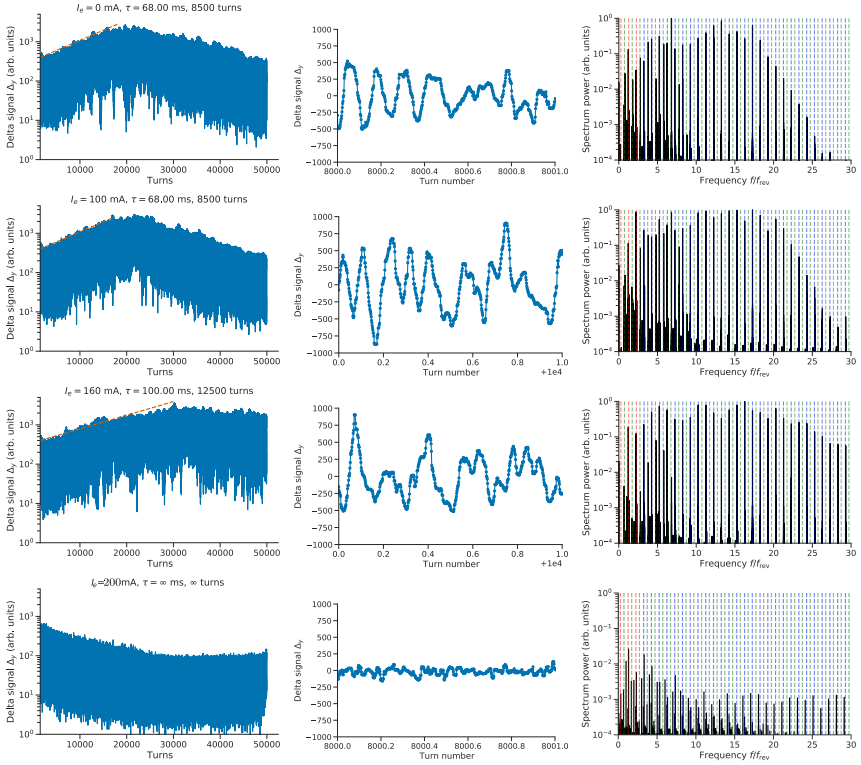
Figure 4.7: Experimental results from top to bottom of the image for Shots 1.6, 1.7, 1.8, 1.9. (Left) Raw BPM data. (Middle) BPM signal showed for 6 consecutive turns from turn 12500 to turn 12506. (Right) fft spectrum of the BPM signal. The dashed line illustrate the modes of the coasting beam oscillations (see Section 2.3.7): in purple fast waves, in green slow waves, in red (slow) backward waves.

same instability with the growth time of 68 ms. For the Shot 1.6 and $I_e = 160$ mA the instability has a lower growth time of 100 ms. The Shot 1.8 is taken under identical conditions to the Shot 1.5. In this case, with the electron beam current of $I_e = 200$ mA, the ion beam is considered stable during the injection plateau.

For all instabilities in Shots 1.4-1.9, we observe a similar broad frequency response to Shots 1.2, 1.3. Additionally, the frequency of oscillations is shown to be higher than the revolution frequency.

In summary, we have observed in Fig. 4.5 that the $^{40}Ar^{18+}$ coasting beam in the SIS18 can be made unstable via chromaticity correction. The observed instability, however, does not correspond to a well-known slow wave mode of the coasting beam. Figures 4.6, 4.7 demonstrate faster instabilities for a different setting of the chromaticity and the fact that this instabilities can be weakened (with $I_e = 160$ mA) or suppressed by the electron cooler (with $I_e = 200$ mA). To the author's knowledge, this is the first experimental confirmation of instability mitigation via an electron lens (cooler).

Section 2.3.7 discussed that the wakefield-driven instabilities could only excite slow wave coasting beam modes. Additionally, in [105], the resistive wall impedance of the SIS18 beam pipe was identified by measuring unstable slow wave coasting beam modes. In our case, a fast wave coasting mode is observed with a broad range of frequencies. Therefore, we can assume that a wakefield does not drive these instabilities.

4.2.2 Results of the experiments for $^{40}Ar^{10+}$

In Table 4.6 the results for several instabilities observed for $^{40}Ar^{10+}$ are summarised. Five shots with different settings are presented. For all shots the chromaticity was set to $Q'_{x,y} = -0.55, 1.25$ in the control system. The electron beam current of the electron cooler was varied for different shots.

Shot	I_e (mA)	BPM Observation	τ (ms)	N
2.1	<500	Stable beam		
2.2	600	Slow instability	108	13500
2.3	700	Fast instability	2.6	324
2.4	600	Slow instability	120	15000
2.5	700	Fast instability	4.5	566

Table 4.6: Instability observation and a reference observation of a stable beam for $^{40}Ar^{10+}$ in our experiment. For each instability we give a current of the electron cooler beam and growth rates in ms and in number of turns. All shots were made at natural chromaticity of SIS18.

Figure 4.8 demonstrates Shots 2.1, 2.2, 2.3 corresponding to three different currents of the electron beam $I_e = 500, 600, 700$ mA. Similarly to the results for $^{40}Ar^{18+}$ in Figs. 4.5, 4.6, 4.7 three figures are shown for each shot: the vertical difference signal for the whole injection plateau; the different signal for the selected few turns; the difference signal spectrum obtained via a Fourier transform. For the Shot 2.1 and electron beam current $I_e = 500$ mA a stable beam is observed. The corresponding frequency spectrum is dominated by noise and the strongest signal simply corresponds to a harmonic of the revolution frequency.

For the electron beam current $I_e = 600$ mA in Shot 2.2, we observe an instability with a growth time of 108 ms developing in the revolution turn range from 40000 to

50000. The corresponding pattern over a few revolution turns is shown in the second row's middle plot. We observe 4 complete oscillations (or one complete oscillation with the wavenumber 4) over ≈ 5.5 revolution turns.

In Section 2.3.7, the fast and slow wave modes of the coasting beams were discussed with the corresponding angular frequencies. For the vertical plane, the betatron tune is $Q_y = 3.27$. The first slow wave corresponds to a wavenumber with the closest integer above the betatron tune $n = 4$. The number for the full rotation of this mode is $N_{\text{ang}} = 1 + Q_y/(n - Q_y) \approx 5.5$.

In the frequency domain, in the rightmost picture, for the current of $I_e = 600$ mA we also see that the frequency $1 - Q_y$ is the strongest one, corresponding to the slow wave mode of the coasting beam. Additionally, the higher harmonics are exponentially weaker. This situation corresponds well with the instability induced by a resistive wall impedance of the SIS18, also observed in [105].

For the Shot 2.3 and the electron beam current of $I_e = 700$ mA a different instability is observed. The growth time of this instability is 2.6 ms or 324 revolution turns. The instability occurs for several thousand turns starting from the revolution turn ≈ 20000. This growth time is significantly shorter than the growth times observed for a resistive wall induced instability in [105].

The pattern of oscillations is demonstrated in the middle plot. We observe that the signal is very clear, and there are six complete oscillations within a single revolution turn.

In the rightmost plot, the frequency spectrum is demonstrated to be dominated by a fast wave mode closest to the revolution frequency harmonic 6. This corresponds to a fast wave mode $n = 3$. The frequency spectrum can still be considered broadband, although one mode is more potent than all others. This instability is similar to those observed with the $^{40}\text{Ar}^{18+}$ beam.

Figure 4.9 demonstrates results for the Shot 2.4. In the top row of the figure on the left, there is a difference signal from a BPM Δ_y plotted over the whole injection plateau. On the right, Δ_y is illustrated for several consecutive revolution turns. The left figure in the bottom row of Fig. 4.9 demonstrates a frequency spectrum of the difference signal. The right figure in the bottom row shows a spectrogram of the difference signal. The spectrogram illustrates the evolution of the spectrum of the difference signal over many revolution turns. We can observe that the most dominant mode corresponds to the frequency of the first slow wave mode $n - Q_y$ with n being the first integer above the integer part of the betatron tune.

In Shot 2.4, the electron beam current was set to $I_e = 600$ mA, and a slow wave instability can be observed with a growth time of 120 ms. Similarly to Fig. 4.8, we observe a slow wave mode $n = 4$ and a nearly perfect rotation of the wave during 5.48 revolution turns.

Figure 4.10 illustrates the experimental results for the Shot 2.5. The same subfigures as for the Shot 2.4 are used here. The electron beam current $I_e = 700$ mA was used in this shot. Instability can be observed after the turn of 20000 with a growth time
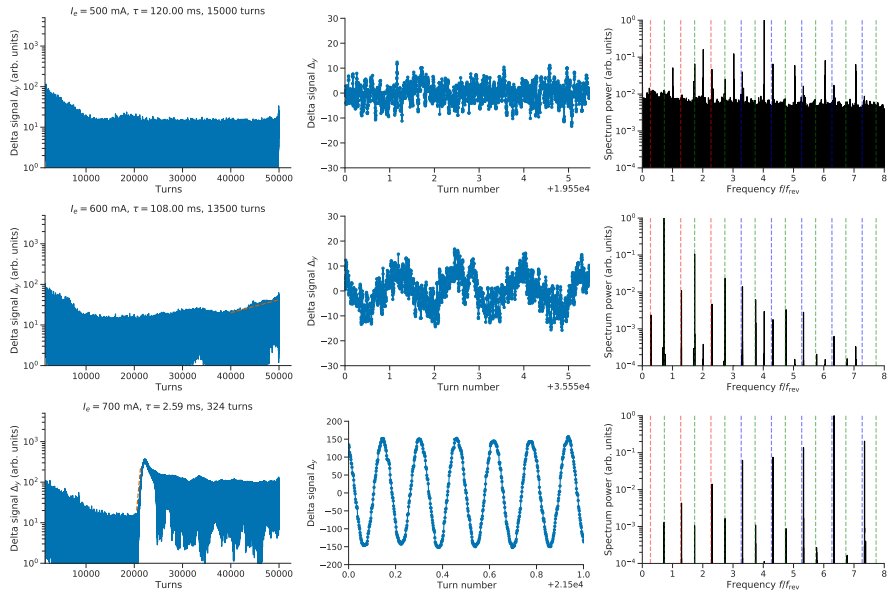
Figure 4.8: Experimental results for Shots 2.1, 2.2, 2.3. (Left) Raw BPM data. (Middle) BPM signal showed for 6 consecutive turns from turn 12500 to turn 12506. (Right) FFT spectrum of the BPM signal. The dashed line illustrate the modes of the coasting beam oscillations (see Section 2.3.7): in purple fast waves, in green slow waves, in red (slow) backward waves.

of 4.5 ms. This instability corresponds to the same settings as in Shot 2.3. It is also characterised as $n = 3$ fast wave instability with the most unstable mode being close to harmonic 6 of the revolution frequency.

During the beam time with the $^{40}Ar^{10+}$, the beam was only unstable with an electron cooler turned on. The electron cooler's current was significantly higher than in the beam time with $^{40}Ar^{18+}$. Two different instabilities were observed for different settings of an electron cooler. One was characterised as a slow wave mode of coasting beam with growth times $\approx$ 100 ms. Another was characterised as a fast wave mode of a coasting beam. For a fast wave mode instability, the growth time was significantly larger $\approx 1ms$. Slow wave mode instability can be related to the machine impedance. In SIS18, specifically to the resistive wall impedance of the SIS18 beam pipe. In the previous study [105] of coasting beam instabilities in SIS18, it was identified as the primary impedance source. On the other hand, the fast wave mode instability cannot be caused by the beam coupling impedance on the SIS18. The beam coupling impedance can only excite the
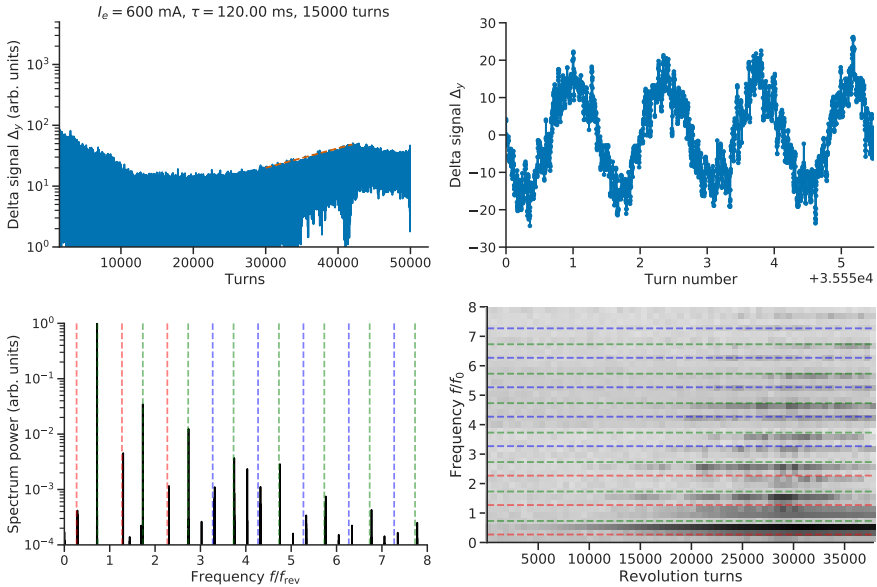
Figure 4.9: Experimental results for Shot 2.4. (Top left) BPM difference signal between vertical planes during the injection plateau. Exponential fit is shown in an orange dashed curve. (Top right) BPM difference signal during a single revolution turn. (Bottom left) Frequency spectrum of the BPM difference signal. (Bottom right) Spectrogram of the frequency spectrum during the injection plateau. The dashed line illustrate the modes of the coasting beam oscillations (see Section 2.3.7): in purple fast waves, in green slow waves, in red (slow) backward waves.

slow wave modes of a coasting beam. Overall, the instabilities observed during the beam time with $^{40}Ar^{10+}$ had a single most unstable mode.

4.3 Interpretation of the results

For both $^{40}Ar^{18+}$ and $^{40}Ar^{10+}$, an Instability is observed. We can classify these instabilities into two types: one has a broadband frequency spectrum centred at the frequency several times higher than the revolution frequency and growth times in the range of $\approx 100 - 10000$ revolution turns; another has a narrowband frequency spectrum centred around the revolution frequency with a growth time of ≈ 10000 turns. The first instability occurs both for $^{40}Ar^{18+}$ and $^{40}Ar^{10+}$, with the electron cooler turned on or off.
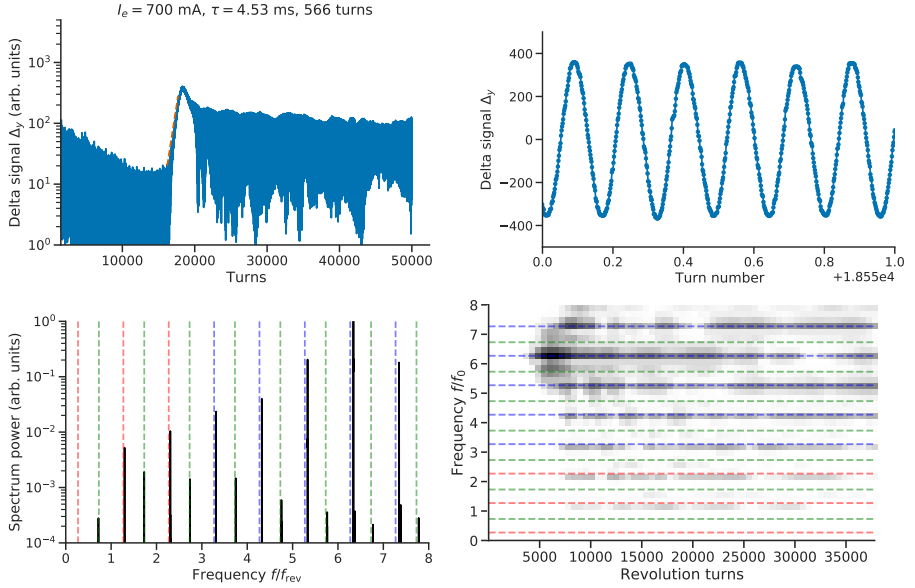
Figure 4.10: Experimental results for Shot 2.5. (Top left) BPM difference signal between vertical planes during the injection plateau. Exponential fit is shown in an orange dashed curve. (Top right) BPM difference signal during a single revolution turn. (Bottom left) Frequency spectrum of the BPM difference signal. (Bottom right) Spectrogram of the frequency spectrum during the injection plateau. The dashed line illustrate the modes of the coasting beam oscillations (see Section 2.3.7): in purple fast waves, in green slow waves, in red (slow) backward waves.

The second type resembles previously studied instability in SIS18 [105]. In [105], it was associated with a resistive wall impedance and compared with an analytical model. The impedance inferred from the experimental data was ≈ 3 times higher than the analytical one. This discrepancy is typical for most synchrotrons. In our experiment, evident slow wave instability of the mode $n = 4$ with a frequency of oscillations of $(n - Q_y)\omega_0$ was observed in Shots 2.2, 2.4. The growth time of the instability was determined to be 120 ms.

Equation (7) in [105] gives an analytical estimation for a growth time for a given impedance

$$\frac{1}{\tau} = \frac{N_{\text{ion}}e^2 Z^2 \beta_r}{8\pi^2 A m_p \gamma_r R Q_y} \Re Z_y^\perp, \tag{4.2}$$

where τ is the growth time; N_{ion} is the intensity; Z, A charge and atomic number of the ion (10 and 40 for Shots. 2.2, 2.4); e, m_p electric charge and mass of the proton; R the effective radius of the accelerator; Q_y is the vertical betatron tune; $\Re Z_y^{\perp}$ is the real part of the transverse vertical (effective) impedance.

In [105] the vertical resistive wall impedance is estimated to be $\Re Z_y^{\perp} = 0.15$ MOhm/m for SIS18, while the experiments of [105] suggest that the impedance is 3 times higher at $\Re Z_y^{\perp} = 0.45$ MOhm/m.

From the data of our experiment (Shots 2.2, 2.4) and Eq. (4.2) we estimate that for $^{40}\text{Ar}^{10+}$ beam with the intensity of 10^{10} particles and a 120 ms instability, we have $\Re Z_y^{\perp} \approx 1.5$ MOhm/m. This value is 10 times higher than the impedance expected from a resistive wall of SIS18 and 3 times higher than the impedance obtained from the previous measurements. Therefore, even this slow wave mode instability is unlikely to be caused by the machine impedance.

This calculation can be repeated for all presented shots. The results of the calculations are presented in Table 4.7.

Shot	τ (ms)	$Z_y^{\perp}$ (MOhm/m)
1.1		0
1.2	92	1.9
1.3	92	1.9
1.4	68	2.6
1.5		0
1.6	68	2.6
1.7		0
1.8	68	2.6
1.9	100	1.7
2.1		0
2.2	108	1.6
2.3	2.6	67
2.4	120	1.5
2.5	4.5	38.7

Table 4.7: Equivalent (to growth times observed in the experiments) effective impedances calculated from Eq. (4.2). Effective impedances for stable shots are simply noted as 0.

These values are significantly larger than the SIS18 vertical impedance from [105] of 0.45 MOhm/m or to the analytical estimation for the resistive wall of 0.15 MOhm/m. Therefore, the machine impedance cannot explain all of the observed instabilities.

We have also observed instabilities where fast wave modes are the most unstable. This is evident, for example, in Shots 1.4, 2.3, 2.5. From Section 2.3.7, we know that

a wakefield cannot drive the fast waves. Therefore, this second argument is that the observed instabilities cannot be explained as a wakefield-driven instability.

Let us examine the possibility that we observe a two-stream instability. Two-stream instabilities cover many different effects, but in all cases, two particle species are involved. A two-stream instability can be caused by the interaction between an ion beam and an electron beam in the cooler. Another possibility is an electron "beam" inside the vacuum chamber, for example, from ionised residual gas and secondary yield emission.

Observations of similar two-stream instabilities have been made, for example, in [108]–[110]. These observations have been summarised in [43] and, in more detail, in [48] (references therein contain a few more examples of similar observations in different accelerators). An estimation of a bounce frequency of trapped electron was made in [110] by the following expression

$$Q_e = \Omega_e \omega_0 = \sqrt{\frac{2Z^2 N r_e c^2}{Aa^2 C}} \approx 1 \dots 10, \tag{4.3}$$

where N is the intensity of ions (for this estimation we used a range of $10^9 \dots 10^{10}$), $r_e = \frac{1}{4\pi\epsilon_0} \frac{e^2}{m_e c^2}$ is the classical electron radius, A, Z atomic mass number and charge number, a is the radius of an ion beam, C, accelerator circumference. If the frequency of the proton oscillations of the unstable beam matches this frequency of trapped electron, then the beam is unstable due to coupled oscillation with the trapped electron beam. In our observations, all of the instabilities had frequencies ranging from zeroth to twentieth harmonics of the revolution frequency, with harmonics five and six being the strongest ones. Therefore, the observed frequencies of the unstable beam match well with the frequencies from an approximate formula Eq. (4.3).

The electron lenses (and electron cooler) are designed in a way to prevent this undesirable interaction of ion beam with electron beam in the lens (see Fig. 1.3). The magnetic field of the solenoid magnet in the interaction region should be strong enough to prevent oscillations of the electron beam of the electron lens. However, it is still possible that some of the instabilities reported here were either caused by the electron lens or enhanced by it.

Specifically for Shots 1.4, 1.6, 1.8, the electron cooler was not powered. Instead, the instability was achieved only by changing the chromaticity. This means that the two-stream instability in SIS18 can be observed without the electron cooler. In fact, for Shots 1.5, 1.7, the electron cooler was powered with a current of 200 mA (with other settings being unchanged), and the beam was considered stable.

In conclusion, several transverse instabilities have been observed with a coasting beam in SIS18. However, the beam-environment interaction driving the instability was not identified with certainty. The instability is likely a two-stream instability. A possible mitigation measure depends on the source of the instability. For example, suppose the

instability is due to powering the electron cooler. The solenoidal field in the interaction region should be increased in that case.

5 Analytical studies: Vlasov formalism with longitudinal and transverse detuning

The majority of the analytical results presented in this chapter were published by the author in [111]. In this chapter we discuss in detail the influence of a PEL on the coherent beam stability. At the end, new dispersion relations for analytical estimation of Landau damping and beam stability are derived.

5.1 Pulsed electron lens as longitudinal detuning

The present derivation of a PEL detuning applies the general perturbation formalism presented in [43], [72], [92], [93]. Additionally, it expands to both transverse $\Delta Q_y^\perp(J_x, J_y)$ and longitudinal $\Delta Q_y^\parallel(J_z, \varphi)$ detuning. At the end, new dispersion relations are derived and two effects of a PEL on the coherent beam stability are discussed. For the longitudinal detuning, the dependency on the longitudinal phase φ is included, because the time scale of the head-tail instability development is the timescale of the synchrotron motion, determined by the synchrotron tune Q_{s_0}. The transverse detuning, on the contrary, can be averaged over significantly faster betatron motion $Q_{x_0, y_0} \gg Q_{s_0}$. Therefore, the transverse detuning is justified to be independent of the betatron phases θ_x, θ_y.

Using a perturbation method, let us assume that the distribution function Ψ has a small ($\epsilon \ll 1$) perturbation $\epsilon \Psi_1$:

$$\Psi = f_0(J_x, J_y) g_0(J_z) + \epsilon \Psi_1(J_x, \theta_x, J_y, \theta_y, J_z, \varphi; t). \tag{5.1}$$

Here we assume that the unperturbed distribution function is factorised into a longitudinal $g_0(J_z)$ and a transverse distribution $f_0(J_x, J_y)$. Time t is taken in the revolution turns and (J_u, θ_u) are action-angle variables, J_u is used for the single-particle amplitudes. Vlasov equation with a dipolar wake $\mathcal{H}_{\text{wake}}$ and a PEL $\mathcal{H}_{\text{PEL}}$ contributions is

$$\frac{d\Psi}{dt} = \frac{\partial \Psi}{\partial t} + [\mathcal{H}_0 + \mathcal{H}_{\text{PEL}} + \epsilon \mathcal{H}_{\text{wake}}, \Psi] = 0, \tag{5.2}$$

where $\mathcal{H}_0 = Q_{y_0} J_y + Q_{x_0} J_x - Q_{s_0} J_z$ is the Hamiltonian of the unperturbed system, $[\mathcal{H}, \Psi]$ is a Poisson bracket notation.

This study is limited to the instabilities driven by dipolar wakefields. The unperturbed distribution has no dipolar moment, therefore $\mathscr{H}_{\text{wake}} = \frac{F_{\text{wake}}(z,t)}{\omega_0 \gamma_r m v} \sqrt{2 J_y \hat{\beta}_y} \sin \theta_y$ is of the order ϵ ($\hat{\beta}_y$ is the average beta function). Thus, at the perturbation order ϵ, Vlasov equation is

$$\frac{\partial \Psi_1}{\partial t} + [\mathscr{H}_0, \Psi_1] + [\mathscr{H}_{\text{PEL}}, \Psi_1] = -[\mathscr{H}_{\text{wake}}, \Psi_0]. \tag{5.3}$$

Hamiltonians are normalised by the revolution frequency ω_0 and by the particle momentum $\gamma m v$. Let us consider a PEL with a homogeneous transverse profile (of the electron beam) and a modulated current with a Gaussian longitudinal profile (z is the longitudinal coordinate, $\sigma_{e_\parallel}$ is the rms size of the electron beam) $I_e(z) = I_{\text{max}} e^{-(z/\sqrt{2}\sigma_{e_\parallel})^2}$, then

$$\mathscr{H}_{\text{PEL}} = \Delta Q_{\text{max}} J_y e^{-(z/\sqrt{2}\sigma_{e_\parallel})^2}, \tag{5.4}$$

where ΔQ_{max} is listed in the Table 5.1.

If the ratio of transverse and longitudinal (geometrical) rms emittances satisfies $\varepsilon_y / \varepsilon_z \ll 1$ then the only significant effect from a PEL is the longitudinal detuning $\Delta Q_y^\parallel (J_z, \varphi) = \frac{\partial \mathscr{H}_{\text{PEL}}}{\partial J_y}$, the same holds for an RFQ as a longitudinal detuning device. Additionally, all synchrobetatron resonances are considered to be weak. The same assumptions are made for the head-tail instability theory in [92] that does not account for either transverse or longitudinal detuning. From the Hamiltonian, we can find that a PEL tune shift is:

$$\Delta Q_y^\parallel (J_z, \varphi)/\Delta Q_{\text{max}} = \underbrace{I_0^{(e)}\left(\frac{J_z}{2\varepsilon_z}\frac{\sigma_z^2}{\sigma_{e_\parallel}^2}\right)}_{\text{static}} + \underbrace{2\sum_{n=1}^{\infty} I_n^{(e)}\left(\frac{J_z}{2\varepsilon_z}\frac{\sigma_z^2}{\sigma_{e_\parallel}^2}\right)\cos(2n\varphi)}_{\text{dynamic}}, \tag{5.5}$$

where $I_n^{(e)}(u) = e^{-u} I_n(u)$ stands for the exponentially scaled modified Bessel function of the first kind. This tune shift has two components. The static component is independent of the longitudinal phase. It is similar to LO but depending on the longitudinal amplitude instead of the transverse amplitudes. The dynamic component depends on the even harmonics $\cos 2n\varphi$. It is closer to the linear chromaticity $\xi^{(1)}$, its average tune shift over a synchrotron period is zero. A similar Fourier decomposition exists for any longitudinal detuning $\Delta Q_y^\parallel(z, \delta)$ because it is guaranteed to be periodic in φ (over a synchrotron period). Chromatic tune shifts depend on the energy spread $\delta^n \propto \sin^n \varphi$, and longitudinal position based kicks (an RFQ or a PEL) depend on $z^n \propto \cos^n \varphi$. Thus, it is generally not accurate to consider tune shifts only varying with the longitudinal amplitude ignoring their dependency on the phase φ.

5.2 Landau damping from a combination of longitudinal and transverse detuning

Assuming a dipolar motion only in the vertical plane in Eq. (5.3), the perturbed distribution function has the following two terms

$$\Psi_1^{\pm}(J_x, \theta_x, J_y, \theta_y, J_z, \varphi, t) = \psi_1(J_x, J_y, J_z, \varphi)e^{\pm j\theta_y} e^{-jQ_{\text{coh}}t}. \tag{5.6}$$

Knowing that the instability coherent tune shift is small $Q_{\text{coh}} - Q_{y_0} \approx 0$, only one term $\Psi_1^- \propto e^{-j\theta_y}$ is significant. The result, after inserting the Hamiltonians and the perturbed distribution function in Eq. (5.3) is a partial differential equation w.r.t φ only:

$$\{Q_{\text{coh}} - Q_{y_0} - \Delta Q_y^{\perp}(J_x, J_y) - \Delta Q_y^{\parallel}(J_z, \varphi) - j[Q_{s_0} + \Delta Q_s(J_z, \varphi)]\partial_\varphi\}\psi_1(J_x, J_y, J_z, \varphi)$$

$$= \sqrt{2J_y\hat{\beta}_y}\, g_0(J_z)\frac{\partial f_0(J_x, J_y)}{\partial J_y}\frac{F_{\text{wake}}(z, t)}{2\omega_0\gamma_r m\nu}, \tag{5.7}$$

where the transverse detuning $\Delta Q_y^{\perp}(J_x, J_y)$ (e.g. LO) is introduced as a small addition to the betatron tune Q_{y_0}. A small synchrotron detuning $\Delta Q_s(J_z, \varphi) \ll Q_{s_0}$ is also included here. Let us find the eigenfunction expansion of $\psi_1 = \sum_l \psi_1^l(J_x, J_y, J_z, \varphi)$ and its eigenvalues Q^l assuming periodic boundary conditions $\psi_1^l(J_x, J_y, J_z, \varphi = 0) = \psi_1^l(J_x, J_y, J_z, \varphi = 2\pi)$ and considering the differential operator on the left hand side of Eq. (5.7)

$$Q^l = -Q_{\text{coh}} + Q_{y_0} + lQ_{s_0} + \langle\Delta Q_y^{\parallel}\rangle_\varphi(J_z) + \Delta Q_y^{\perp}(J_x, J_y) + l\langle\Delta Q_s\rangle_\varphi(J_z), \tag{5.8}$$

$$\psi_1^l(J_z, \varphi) = A_l(J_x, J_y, J_z)e^{jl\varphi} e^{-jB(J_z, \varphi)}, \tag{5.9}$$

$$B(J_z, \varphi) = \int_0^\varphi \left[\Delta Q_y^{\parallel}(J_z, \varphi') - \langle\Delta Q_y^{\parallel}\rangle_{\varphi'}(J_z)\right]\frac{\mathrm{d}\varphi'}{Q_s}, \tag{5.10}$$

where $\langle\Delta Q_y^{\parallel}\rangle_{\varphi'}(J_z)$ indicates averaging over a synchrotron period and thus depends only on the longitudinal amplitude J_z. The function $B(J_z, \varphi)$ generalises the betatron phase factor χ of the linear chromaticity $\xi^{(1)}$ (see Eq. (6.185, 6.187) in [92]) for arbitrary longitudinal detuning. It has been modified w.r.t Eq. (20) in [72] and Eq. (9) in [112] (where it is denoted as Λ) to include $Q_s(J_z, \varphi)$ in the integral to account for $\Delta Q_s(J_z, \varphi)$ detuning and its effect on the betatron phase factor. The function B specifies for a given particle with an amplitude J_z and a phase φ, by how much it leads or trails the head particle in the betatron phase. Figure 5.1 demonstrates the variation of the betatron phase factor over a single synchrotron period: for the linear chromaticity $\xi^{(1)}$, there is a phase difference between the head and the tail of the particle reflected by the B-function;
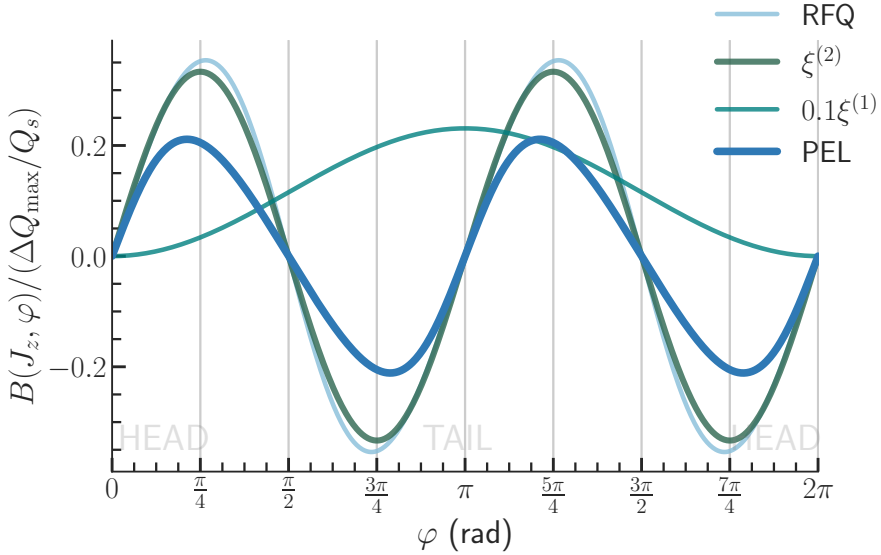
Figure 5.1: Comparison between the betatron phase factors $B(J_z, \varphi)$ for a PEL, $\xi^{(2)}$ and an RFQ. The PEL and the RFQ are matched to the rms bunch length, the value of $\xi^{(2)}$ corresponds to the same rms tune spread, $J_z = \varepsilon_z$. The case of a linear chromaticity $\xi^{(1)}$ is shown for reference. Curves obtained analytically from Eq. (5.10).

for a PEL or the second order chromaticity $\xi^{(2)}$, bunch head and tail particles have the same phase, but particles near bunch ends still have different phases. Specific formulae for the betatron phase factor $B(J_z, \varphi)$ and tune shifts ΔQ_y are given in Table 5.1 for a PEL, an RFQ, a DC EL, and LO. One can observe that the B-function of a PEL and an RFQ has only even harmonics of φ, and only the J_z dependency is different. For a PEL and for an RFQ, the first even harmonic $\sin 2\varphi$ is the strongest one, corresponding to the second order chromaticity $\xi^{(2)}$ tune shift (see Eq. (33) in [72]). The B-function (see Fig. 5.1) of a PEL is described well by the first two even φ harmonics. Figure 5.1 illustrates that the $B(J_z = \varepsilon_z, \varphi)$-function of a PEL is similar to that of the second order chromaticity for $\sigma_z = \sigma_{e_\parallel}$ (from Table 5.1) as well as to an RFQ when the wavelength is matched to the bunch length.

Figure 5.2 demonstrates how strong each individual harmonic is for the same PEL and RFQ settings as in Fig. 5.1. Only even harmonics are present for both devices in the proposed setup, where the kick is symmetric w.r.t the bunch center. If, for example, an RFQ is operated with asymmetric kick, there is no static component of the detuning (and
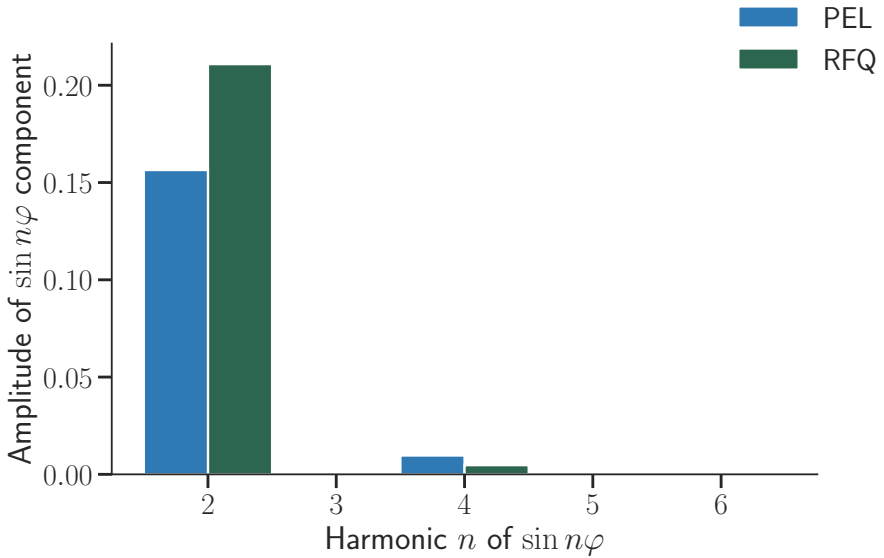
Figure 5.2: First ten harmonics of φ for PEL (blue) and RFQ (orange) obtained from formulae in Table 5.1 for B-function of Eq.(5.10).

no Landau damping) but dynamic component will have odd harmonics of $\sin n\varphi$. For both a PEL and an RFQ the strongest harmonic is $\sin 2\varphi$ and the effect of the B-function vanishes for harmonic 6 and higher. One notable difference between a PEL and an RFQ is significance of $\sin 4\varphi$ harmonic for PEL. This harmonic is tilting the sine wave from Fig. 5.1 of PEL. The contribution from higher harmonics is mostly negligible for the parameters considered in this work.

Landau damping with the transverse detuning, in contrast, does not affect betatron phase relation between the head and the tail of the bunch.

After substituting Ψ_1 using the eigenfunction expansion of Eq. (5.9) into the Eq. (5.7) it reduces to an expression for the function of the transverse and longitudinal amplitudes $A_l(J_x, J_y, J_z)$:

$$\sum_{l'=-\infty}^{\infty} \frac{A_{l'}(J_x, J_y, J_z)}{\sqrt{2 J_y \hat{\beta}_y \frac{\partial f_0(J_x, J_y)}{\partial J_y}}} e^{jl'\varphi} e^{-jB(J_z, \varphi)} Q^{l'} = -\frac{F_{\text{wake}}(J_z, \varphi; t)}{2\omega_0 \gamma_r m v} g_0(J_z). \tag{5.11}$$

The right hand side of Eq. (5.11) does not depend on the transverse amplitudes $\{J_x, J_y\}$, thus the left hand side must be constant w.r.t. these coordinates. The amplitude de-

	LO	RFQ	PEL	DC EL
ΔQ_{max}	$\propto I_{\mathrm{LO}}\frac{J_x}{\varepsilon_x}$	$\frac{\hat\beta_y}{2\pi}\frac{q v_2}{p_0 \omega_{\mathrm{RFQ}}}$	$\frac{Z}{A}\frac{I_e}{I_a}\frac{m_e}{m_p}\frac{g L_e}{4\pi\varepsilon_{nx}}\frac{\sigma_x^2}{\sigma_z^2}\frac{1\pm\beta_e\beta_i}{\beta_p\beta_i}$	$\int_0^1 \left[I_0^{(e)}\left(uk_y\right)-I_1^{(e)}\left(uk_y\right)\right]$ $\times I_0^{(e)}\left(uk_x\right)du$
$\langle \Delta Q_y / \Delta Q_{\mathrm{max}}\rangle_\phi$	$a_{yx}\frac{J_x}{\varepsilon_x}+a_{yy}\frac{J_y}{\varepsilon_y}$	$J_0\left(\frac{\sigma_z}{\lambda_{\mathrm{RFQ}}}\sqrt{2\frac{J_z}{2\varepsilon_z}}\right)$	$I_0^{(e)}\left(\frac{J_z}{2\varepsilon_z}\frac{\sigma_z^2}{\sigma_{e\parallel}^2}\right)$	
$\Delta Q_{\mathrm{rms}}/\Delta Q_{\mathrm{max}}$	0.24	0.2	0.14	0.16
$B(J_z,\varphi)/\frac{\Delta Q_{\mathrm{max}}}{Q_s}$	0	$\sum_{n=1}^\infty J_{2n}\left(\frac{\omega_{\mathrm{rfq}}\sigma_z}{\beta_r c}\sqrt{\frac{J_z}{\varepsilon_z}}\right)\frac{\sin(2n\varphi)}{n}$	$\sum_{n=1}^\infty I_n^{(e)}\left(\frac{J_z}{2\varepsilon_z}\frac{\sigma_{e\parallel}^2}{\sigma_z^2}\right)\frac{\sin(2n\varphi)}{n}$	0
$H_l(z^{(1)},z^{(2)},...z^{(k)})$	$j^{-l}J_l(z^{(1)})$	$\approx j^{-l}\sum_{n=-\infty}^\infty J_{l+2n}(z^{(1)})J_n(z^{(2)})$		$j^{-l}J_l(z^{(1)})$

Table 5.1: Tune spreads, betatron phase factors $B(J_z,\phi)$ and head-tail spectrum functions $H(z^{(1)},z^{(2)})$ for electron lenses, an RFQ and LO. $k_{x,y}=\frac{J_{x,y}}{2\varepsilon_{x,y}}\frac{\sigma_{x,y}^2}{\sigma_{e\perp}^2}$.

pendency can be redefined as $A_{l'}(J_x,J_y,J_z)=R_{l'}(J_z)I_{l'}(Q_{\mathrm{coh}})\sqrt{2\hat\beta_y/J_y}$, where $R_{l'}(J_z)$ is the longitudinal mode. By substituting the expression for the amplitude dependency in Eq. (5.11) we find the dispersion integrand

$$I_l(Q_{\mathrm{coh}}) = \frac{\frac{\partial f_0(J_x,J_y)}{\partial J_y}J_y}{Q_{\mathrm{coh}} - Q_{y_0} - \Delta Q_y^\perp - \langle \Delta Q_y^\parallel\rangle_\varphi - lQ_s}. \tag{5.12}$$

This separation of pure longitudinal amplitude dependency $R_{l'}(J_z)$ from $A_{l'}(J_x,J_y,J_z)$ is only possible because we consider a specific combination of transverse and longitudinal detuning $\Delta Q_y = \Delta Q_y^\parallel(J_z,\varphi) + \Delta Q_y^\perp(J_x,J_y)$ and not a more general case of detuning $\Delta Q_y(J_x,J_y,J_z,\varphi)$. In the latter case, one would need to solve an integral equation for the amplitudes and the betatron phase factor B will also be a function of the amplitudes J_x,J_y,J_z.

Now everything about the perturbed distribution function Ψ_1 is known, except its longitudinal modes $R_l(J_z)$:

$$\Psi_1 = e^{-jQ_{\mathrm{coh}}t}e^{-jB(J_z,\varphi)}\sum_{l=-\infty}^\infty R_l(J_z)e^{jl\varphi}e^{-j\theta_y}I_l(Q_{\mathrm{coh}})\sqrt{2\hat\beta_y/J_y}. \tag{5.13}$$

In order to find the longitudinal modes we need to solve the Vlasov equation perturbed by a wakefield force, expressed as

$$F_{\mathrm{wake}} = \frac{q^2 Q_{s_0}\omega_0}{Q_{y_0}\eta R}\sum_{p=-\infty}^\infty Z_y^\perp(Q_p)e^{jQ_p \frac{r}{R}\cos\varphi}\sum_{l'=-\infty}^\infty \lambda_l(Q_p) \tag{5.14}$$

(for comparison, see Eq. (6.173) in [92] with $r=\sqrt{2J_z\hat\beta_z}$, where $\hat\beta_z$ is the longitudinal beta function). The frequency of the impedance $Q_p = Q_{y_0} + lQ_{s_0} + p$ is normalized by

the revolution frequency ω_0, $R = C/(2\pi)$ is the accelerator effective radius, η is the slip factor, q is the ion charge. The line density of the dipolar moment $\lambda_l(Q_p)$ of the distribution function Ψ for the azimuthal mode l in the frequency domain is

$$\lambda_l(Q_{p_0}) = \int_0^\infty H_l^{p_0}(r) R_l(r) \left[\iint I_l(Q_{\text{coh}}) \mathrm{d}J_x \mathrm{d}J_y \right] r \mathrm{d}r. \tag{5.15}$$

H-functions have the physical meaning of an airbag bunch head-tail mode spectrum. In general, the head-tail mode spectrum is $|\lambda_l|^2$ and it depends on both the spectrum functions H and the longitudinal distribution function g_0. Integral representation of H-functions was first defined by the authors of [72] in Eq. (22):

$$H_l^p(J_z) = \int_0^{2\pi} e^{-jQ_p \frac{r}{R} \cos\varphi} e^{-jB_{\text{PEL}}} e^{jl\varphi} \frac{\mathrm{d}\varphi}{2\pi}. \tag{5.16}$$

Using Jacobi-Anger expansion [113], we introduce a simpler sum representation, considering only the first even harmonic ($\propto \sin 2\varphi$) of B_{PEL} (see Table 5.1), and the contribution of the wakefield, and the linear chromaticity $\xi^{(1)}$ ($\propto \cos\varphi$):

$$H_l^p(z^{(1)}, z^{(2)}) = j^{-l} \sum_{n=-\infty}^{n=+\infty} J_{l+2n}(z^{(1)}) J_n(z^{(2)}), \tag{5.17}$$

where $J_n(x)$ is the Bessel function of the first kind [113]. The arguments of the H-function are defined as

$$z^{(1)} = (Q_p - Q_{y_0} \xi^{(1)}/\eta) \frac{2\sigma_z}{R} \sqrt{\frac{J_z}{2\varepsilon_z}}, \tag{5.18}$$

$$z_{\text{PEL}}^{(2)} = \frac{\Delta Q_{\text{max}}}{Q_{s_0}} I_1^e \left(\frac{J_z}{2\varepsilon_z} \frac{\sigma_z^2}{\sigma_{e_\parallel}^2} \right), \tag{5.19}$$

where $z^{(1)}$ stands for the first harmonic effects (wakefield and $\xi^{(1)}$), and $z_{\text{PEL}}^{(2)}$ describes the second harmonic effects (from a PEL in Eq. (5.19), an RFQ or the second order chromaticity $\xi^{(2)}$ have a similar formula). This expression can be extended to include other higher harmonics as well. The sum representation in Eq. (5.17) has advantages for faster numerical calculations and for understanding the effect of a PEL on the head-tail mode spectrum. Indeed, if $z^{(2)} \approx 0$, only $n = 0$ term is nonzero, and we have a known expression $j^{-l} J_l(z^{(1)})$ (for example, Eq. (6.177) and discussions therein in [92]). As $z^{(2)}$ rises, $n = \pm 1$ components become significant and the mode spectrum mixes with

$J_{l\pm2}(z^{(1)})$ terms and $J_{n=0,1}(z^{(2)})$ serve as the weight functions. Head-tail mode spectrum distortion by a PEL, determined by $z_{\text{PEL}}^{(2)}$, scales with the parameter $\Delta Q_{\text{max}}/Q_{s_0}$. Additionally, like for the Bessel functions [113], from Eq. (5.17) $\sum_l |H_l^p(z^{(1)}, z^{(2)})|^2 = 1$ for any p, $z^{(1)}$, $z^{(2)}$. Meaning that the second harmonic effect $z^{(2)}$ redistributes the energy between different modes, modifying the shape of the mode spectrum by making some modes stronger and others weaker. Distortion of the mode spectrum by the longitudinal detuning is the origin of the effective impedance modification. An example for changes in the mode spectrum is demonstrated in Fig. 5.3 (top plot) for a moderately strong PEL $\Delta Q_{\text{max}}/Q_{s_0} = 0.5$. The weak distortion of the zero mode is evident from Eq. (5.17), because the sum becomes symmetric for $\pm n$ terms and odd terms cancel each other. The l-modes are no longer degenerate, the $l = 1, 2$ modes become weaker, and the $l = -1, -2$ modes become stronger, see Fig. 5.3 (top plot). In Fig. 5.3 (bottom plot), we consider two different frequencies and demonstrate how the mode spectrum at these frequencies is modified depending on the strength of the longitudinal detuning $\Delta Q_{\text{max}}/Q_{s_0}$.

After inserting Eq. (5.14) into Eq. (5.11), multiplying both sides by $e^{-jl\varphi}$ and integrating over φ, a single mode l is determined by

$$R_l(J_z) = jKg_0(J_z) \sum_{p=-\infty}^{\infty} Z_y^{\perp}(Q_p) H_l^{p^\dagger}(J_z) \sum_{l'=-\infty}^{\infty} \lambda_{l'}(p), \tag{5.20}$$

with $K = q^2 Q_{s_0}/(2Q_{y_0} E \eta T_0)$ (1/Ohm), where E is the energy and T_0 is the revolution period, $H_l^{p^\dagger}$ is the complex conjugate of H_l^p function defined in Eqs. (5.16, 5.17). This extends the Sacherer's integral equation [44]. Using the Laclare's approach [114], an expression for $\lambda_l(p_0)$ is obtained by multiplying both sides of Eq. (5.20) by $H_{p_0}^l \left[I_l(Q_{\text{coh}}) dJ_x dJ_y \right] r dr$ and integrating

$$\begin{aligned} \lambda_l(p_0) &= -jK \sum_{p=-\infty}^{\infty} \sum_{l'=-\infty}^{\infty} \lambda^{l'}(p) Z_y^{\perp}(Q_p) \\ &\times \int_0^{\infty} \left[I_l(Q_{\text{coh}}) dJ_x dJ_y \right] H_l^{p^\dagger}(r) H_l^{p_0}(r) g_0(r) r dr. \end{aligned} \tag{5.21}$$

Consequently, this general integral equation simultaneously includes Landau damping with transverse and longitudinal detuning. If the transverse detuning is negligible $\Delta Q_y^{\perp}(J_x, J_y) = 0$, the results of Eq. (23) in [72] are recovered. If the longitudinal detuning is negligible $\langle \Delta Q_y^{\parallel} \rangle_\varphi (J_z) = 0$, the results of the dispersion relation Eq. (1) in [75] are recovered. Thus, our results for the linear combination of transverse and longitudinal detuning are general and in the limiting cases converge to the known results. Equation (5.21) can be written in the matrix form, and the solutions to this eigenvalue
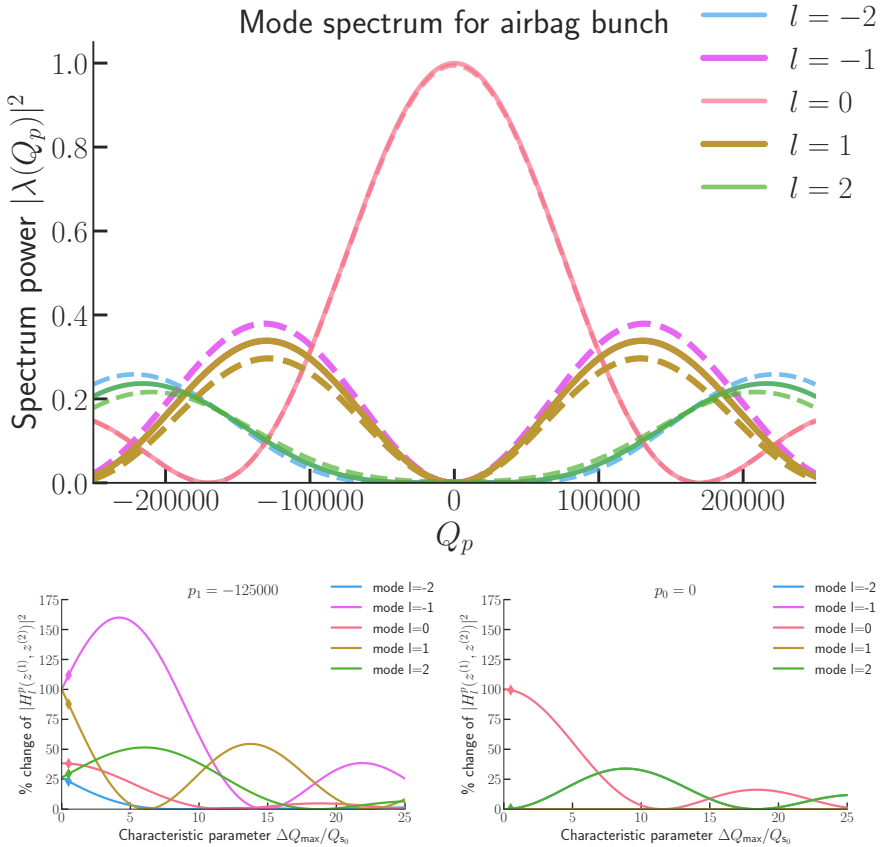
Figure 5.3: (top) Head-tail mode spectrum $|H_l^p(z^{(1)}, z^{(2)})|^2$ for an airbag bunch, unperturbed (solid lines) and with the effect of a PEL (dashed lines) for $\Delta Q_{\max}/Q_{s_0} = 0.5$. (bottom) Dependency of mode power spectrum on the PEL strength $\Delta Q_{\max}$ at points where modes $|l| = \{0, 1\}$ are near their maxima. Curves are obtained analytically from Eq. (5.15).

problem would be the coherent tune shifts and the eigenmodes. Dedicated Vlasov solvers are usually used to solve this type of an eigenvalue problem numerically [73], [115]. However, the present semi-analytical Vlasov solvers do not account for arbitrary longi-

tudinal detuning. Under the assumption of a narrow band impedance (see [72]) and only one excited azimuthal mode, we obtain the following dispersion relation:

$$\Delta Q^{-1} = \frac{1}{N_1} \int \frac{\frac{\partial \Psi_0}{\partial J_y} J_y |H_l^{p_0}(z^{(1)}, z^{(2)})|^2 \mathrm{d}J_z \mathrm{d}J_x \mathrm{d}J_y}{Q_{\mathrm{coh}} - Q_{y_0} - \langle \Delta Q_y^{\parallel} \rangle_\varphi(J_z) - \Delta Q_y^{\perp}(J_x, J_y) - l[Q_{s_0} + \langle \Delta Q_s \rangle_\varphi(J_z)]}, \quad (5.22)$$

where $N_1 = \int \frac{\partial \Psi_0}{\partial J_y} J_y |H_l^{p_0}(z^{(1)}, z^{(2)})|^2 \mathrm{d}J_x \mathrm{d}J_y \mathrm{d}J_z$ is the normalisation found from no Landau damping case. ΔQ is the coherent tune shift in the absence of Landau damping ($\langle \Delta Q_y^{\parallel} \rangle_\varphi(J_z) = \Delta Q_y^{\perp}(J_x, J_y) = \langle \Delta Q_s \rangle_\varphi(J_z) = 0$). Q_{coh} is the coherent tune in the presence of Landau damping. This case corresponds to the static component of the tune shifts being zero, but the normalisation N_1 is still affected by the dynamic component of the tune shift $z^{(2)}$ via $H_{p_0}^l$ function.

Linear chromaticity $\xi^{(1)}$ is a special case of the longitudinal detuning that has no static component and, thus, no Landau damping. In this case the effective impedance changes and the mode spectrum modification is a shift by the chromatic frequency $Q_{y_0} \xi^{(1)}/\eta$. In Eq. (5.23), no assumptions about the machine impedance and the arguments of the H-function are necessary for the case of the transverse detuning only.

If we assume a small first argument $z^{(1)} \ll 1$ [Eq. (5.18)] of the H-function in Eq. (5.17), this is a further assumption on the impedance, meaning that the frequency of the narrow band impedance (shifted by the chromatic frequency) is much smaller than the spread of frequencies in the bunch. Additionally, we assume a small second argument $z^{(2)} \ll 1$ (Eq. (5.19)) such that $J_0(z^{(2)}) \approx 1$ and other weight functions in Eq. (5.17) are approximately zero — the head-tail mode spectrum is unperturbed by the longitudinal detuning. The dispersion relation simplifies to

$$\Delta Q^{-1} = \frac{1}{N_2} \int \frac{\frac{\partial \Psi_0}{\partial J_y} J_y J_z^{|l|} \mathrm{d}J_x \mathrm{d}J_y \mathrm{d}J_z}{Q_{\mathrm{coh}} - Q_{y_0} - \langle \Delta Q_y^{\parallel} \rangle_\varphi(J_z) - \Delta Q_y^{\perp}(J_x, J_y) - l[Q_{s_0} + \langle \Delta Q_s \rangle_\varphi(J_z)]}, \quad (5.23)$$

where $N_2 = \iiint \frac{\partial \Psi_0}{\partial J_y} J_y J_z^{|l|} \mathrm{d}J_x \mathrm{d}J_y \mathrm{d}J_z$. This corresponds to Eq. (1, 2) of [75] if we set either the longitudinal $\Delta Q_y^{\parallel}$ or the transverse detuning $\Delta Q_y^{\perp}$ to zero. Our results are valid for arbitrary distributions $\Psi_0 = f_0(J_x, J_y) g_0(J_z)$, account for the dynamic part of the longitudinal detuning $\Delta Q_y^{\parallel}(J_z, \varphi)$ and quantify the head-tail mode spectrum distortion by the longitudinal detuning.

6 Numerical studies: Head-tail mode zero

The majority of the numerical results presented in this chapter are published by the author in [111] and in [79]. In this chapter, the rigid mode kick model reconstructs the stability boundaries in the simulations. This model corresponds to a constant wake force acting on the beam [a delta-function impedance $Z_y^\perp \propto \delta_D(Q)$] [73]. Therefore, it drives a rigid mode oscillations with a specific coherent tune shift, corresponding to the zero head-tail mode. A similar method was described and employed in a proof-of-principle experiment in [85] using a transverse feedback system (as an antidamper) in the LHC study and it agreed with the known stability boundaries for LO.

6.1 Rigid mode kick method

The rigid mode of bunch oscillations is driven in the simulations by the following kick:

$$\Delta y' = \Im \Delta Q \overline{y'} + \Re \Delta Q \overline{y}/\hat{\beta}_y, \qquad (6.1)$$

where $\overline{y}$, $\overline{y'}$ are the beam offset and its derivative; $\Re \Delta Q$, $\Im \Delta Q$ are real and imaginary parts of the coherent tune shift caused by the kick in the absence of Landau damping; $\hat{\beta}_y$ is the average beta function of the ring. The present implementation of the rigid mode kick is only for the zero linear chromaticity $\xi^{(1)} = 0$ case. Thus, the parameter $z^{(1)} = 0$. Using a weak longitudinal detuning $\Delta Q_{\max}/Q_{s_0} \ll 1$, we ensure that the underlying assumptions of the dispersion relation Eq. (5.23) are fulfilled.

In the simulations, 2D scans over the complex coherent tune shift are performed. All 2D scans are made with the same beam and machine parameters using 10^5 macroparticles over 10^5 turns ($\gtrsim 150$ synchrotron periods), only changing the source of the detuning (a PEL, a DC EL, LO, an RFQ). In this section bunch particle distribution is Gaussian transversely and longitudinally. Separating this 2D plane into a stable and an unstable areas results in the reconstruction of the stability boundaries. We reconstruct stability boundaries from the simulation data by identifying all points (on the coherent tune shift complex plane) with exponentially growing beam offset and extrapolating their growth rates to the zero growth rate isoline — obtained stability boundaries are defined using the same criterion as the analytical ones.

In the simulations the instability develops from the numerical noise. The instability growth rate is determined by an exponential fit to the envelope of beam offset evolution.
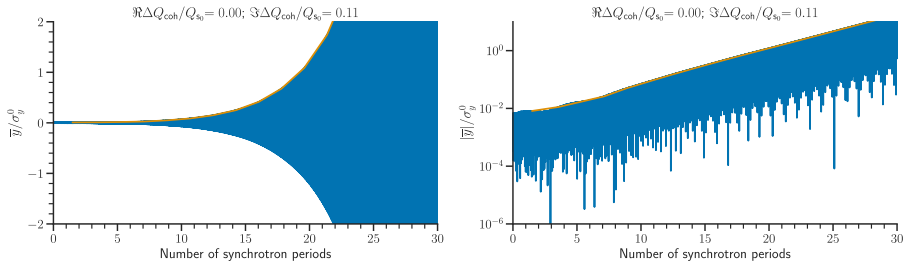
Figure 6.1: Example of simulation results over several synchrotron periods. Simulations were performed with the rigid mode kick set to produce the coherent tune shift 0.11 in the absence of Landau damping. Beam offset $\overline{y}$ normalised by the beam size at turn 0 σ_y^0 is displayed (blue) in the normal scale on the left and in the logarithmic scale on the right). The envelope of the beam oscillations is fitted to an exponential function (orange).

An example of the simulated data and of an exponential fit is presented in Fig. 6.1. An example of reconstruction of the stability boundary procedure is demonstrated in Fig. 6.2.

The tracking code PyHEADTAIL [98] is employed for the simulations. The implementations of LO and of an RFQ are identical to [72], both a DC EL and a PEL are implemented as slice-by-slice localized kicks. For a DC EL, each particle of the ion beam receives a kick from the field of a transversely Gaussian electron beam, with a constant longitudinal profile. For a PEL, the electromagnetic field of the electron beam is transversely homogeneous, and the kick amplitude is modulated along the bunch length matching the ion beam profile.

6.2 Probing stability diagram with a rigid mode kick

First, our particle tracking simulations verify that a tune shift from a PEL leads to Landau damping. Then we compare a PEL to the other means of Landau damping (LO, an RFQ, a DC EL) using the same simulation framework, the same criteria for beam stability and the same rms tune spread from all four devices. Finally, we demonstrate the stability boundary from a combination of longitudinal detuning and transverse detuning, using a PEL and LO as an example. These simulation results are used to verify our analytical results from Section 5 and specifically the dispersion relation Eq. (5.23).
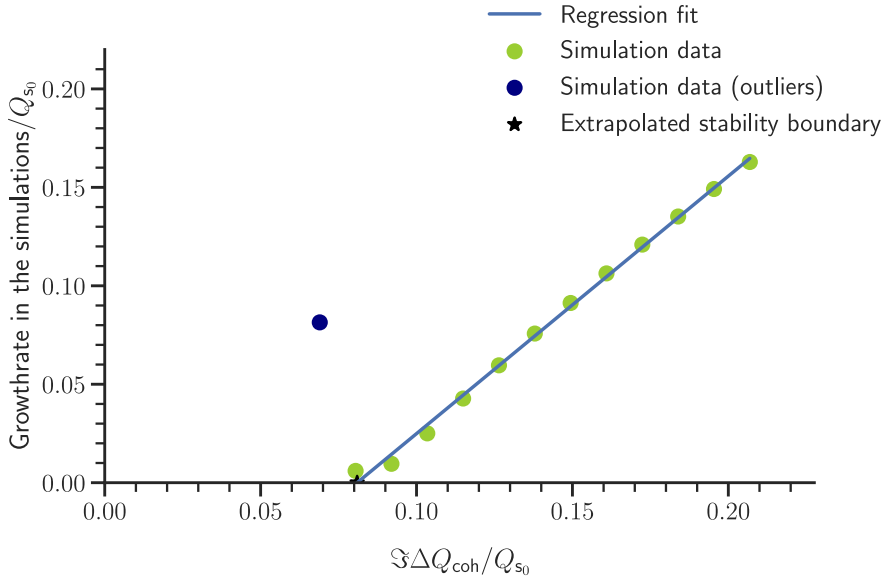
Figure 6.2: The growth rate observed in the simulations (green dots) is plotted as a function of the imaginary part of the coherent tune shift in the absence of Landau damping. In this example simulations, PEL strength was nonzero. Both axes are normalised by the synchrotron tune. With the Random Sample Consensus algorithm (RANSAC) regression algorithms outlier points are identified (navy-blue points) and the linear regression fit (blue line) is plotted. The intersection of it and the zero growth rate is an extrapolated stability boundary estimation (black star).

6.2.1 Stability boundaries from either longitudinal or transverse detuning

Figure 6.3 (top) compares simulated (green histograms) tune distributions for LO (yellow), a DC EL (red), a PEL (blue), and an RFQ (light-blue) to the corresponding analytical distributions (coloured histograms). The vertical and horizontal tune spreads and the complex coherent tune shift axes in Fig. 6.3 are normalised by the rms betatron tune spread ΔQ_{rms}. Using this normalisation allows to compare various tune spreads from a PEL, LO, a DC EL and an RFQ.

Figure 6.3 (bottom) shows the reconstructed stability areas (solid green lines) of all four devices together with the analytical results from Eq. (5.23) (colored lines). For equal rms tune spreads, the stability area is roughly the same. An RFQ and LO tend to
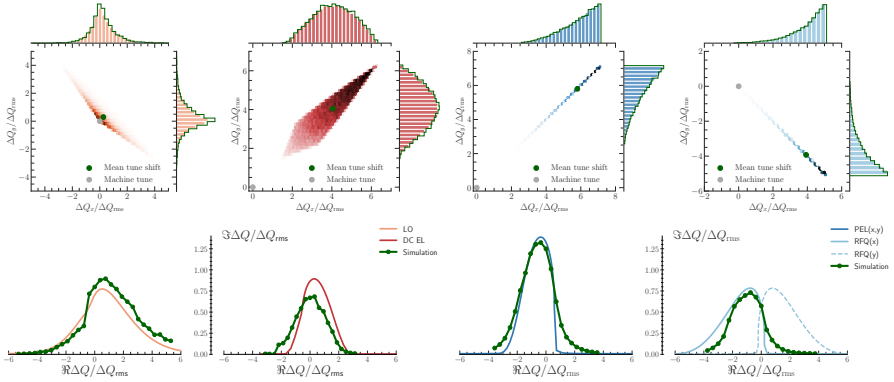
Figure 6.3: (top) Incoherent tune spreads and average tune shifts (green dot). Left to right: LO (yellow), a DC EL (red), a PEL (dark-blue), an RFQ (light-blue). (bottom) Stability boundaries for the head-tail mode $l = 0$ from Eq. (5.23) compared to the results of the simulation scans with the rigid mode kick, Eq. (6.1).

have a wider stability boundary. This is attributed to larger tails in the tune distribution for LO and an RFQ. Tune shifts from a PEL are the same in the vertical and the horizontal planes, but not for an RFQ. Thus, a PEL, contrary to an RFQ, ensures the same stability area in both the horizontal and the vertical planes. An RFQ would require a two-family scheme or a combination with LO (see [71]) because the instability coherent tune shift is typically similar in both planes.

Figure 6.3 (bottom right) illustrates a near-perfect agreement with analytical stability boundaries for the weak longitudinal detuning. Furthermore, comparisons with Landau damping with the transverse detuning reveal that the stable area is roughly the same for equal rms tune spreads. As a rule of thumb, ΔQ_{rms} defines the stability boundary 'height', meaning that the fastest instability that is damped has a growth rate roughly equal to the rms tune spread $\approx \Delta Q_{rms}$. The full tune spread $\Delta Q_{full} \approx (4 \ldots 6)\Delta Q_{rms}$ determines the 'width' of the stability boundary. The shape of the stability boundary is related to the incoherent tune distribution.

In Fig. 6.4 analytical estimations are compared with our simulation results for the transverse Gaussian distribution and a round electron beam for DC EL for several values of the transverse beam size ratio $r = \sigma_{e_\perp}/\sigma_{x_0,y_0} = \{0.7, 1.0, 1.4, 1.8\}$. Similar ratios were considered only analytically in [77]. Therefore, our simulation results confirm that a DC EL has a possibility to slightly adjust the stability boundary depending on this ratio.
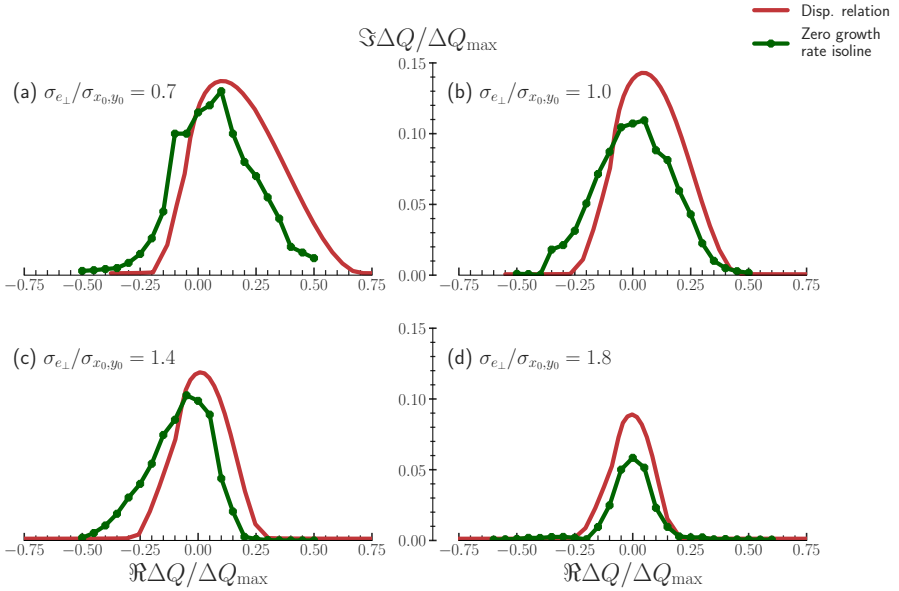
Figure 6.4: DC EL stability diagrams from Eq. (5.23) (red lines) for the head-tail mode $l = 0$ depending on the electron to ion rms beam transverse size ratio $r = \sigma_{e_\perp}/\sigma_{x_0,y_0}$. It is compared to the results of simulation scans (green lines) with the rigid mode kick (defined in Eq. (6.1)).

6.2.2 Stability boundaries from a combination of DC EL and LO in the FCC-hh

In this section the results of [79] are briefly summarised with the focus on the reconstruction of stability boundaries. In [79] the author estimated stability boundaries for FCC-hh from a combination of LO and a DC EL. This is a combination of two different sources of transverse detuning. An earlier version of the stability boundary reconstruction method was used in [79].

For the estimation of the stability boundary from tracking simulations two methods are employed. The first method was employed throughout this section and described in detail in Section 6.1. The second one is only different in how it separates the complex plane of $\Re\Delta Q$, $\Im\Delta Q$ into a stable and unstable regions. It is applying a score function to the offset and emittance evolution for each pair of $\Re\Delta Q$, $\Im\Delta Q$. If the beam offset exceeds a threshold value (5 μm) and the offset envelope fits an exponential or emittance exceeds 10% of its initial value, we consider a beam unstable for the complex coherent tune shift
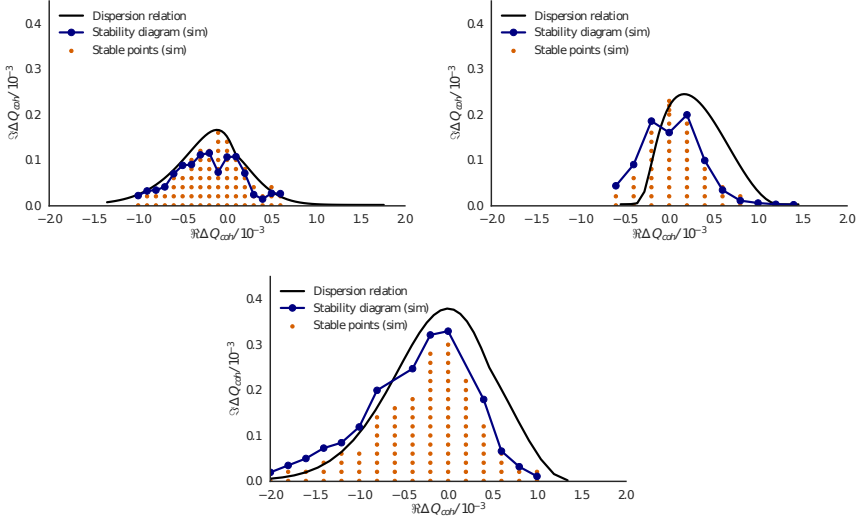
Figure 6.5: Stability boundaries obtained from the simulation with zero chromaticity $\xi^{(1)} = 0$ and only mode $l = 0$ excited by the rigid mode kick Eq. (6.1). On the left, LHC-like LO are the only source of detuning. On the right, a DC EL with $\Delta Q_e = 2 \times 10^{-3}$ is the only source of detuning. On the bottom, a combination of these LO with this DC EL is presented. The stability boundary of Eq. 5.23 is shown in black colour. The results of the first reconstruction methods in dark blue colour. And the results (stable area) of the second reconstruction methods are shown as orange dots.

$\Re\Delta Q, \Im\Delta Q$. Otherwise, the beam is considered stable and from the set of the stable points stability boundary is visualised.

Figure 6.5 demonstrates results of particle tracking simulations and our stability boundary reconstruction methods. The axes of this plot are not normalised, because Fig. 6.5 presents results for a specific machine. Three different cases are presented. First, on the left, the stability boundary only due to LO detuning. Second, on the right, the stability boundary only due to DC EL detuning. And lastly, on the bottom, the stability boundary from their combination is demonstrated.

For the LHC-like octupoles the stability boundary obtained from the simulations is predicted by the dispersion relation of Eq. 5.23. Both the score function (orange dots) and growth rate interpolation methods (blue dotted curve) show a good agreement between the two methods and with the analytical estimation. In the case of an electron lens the simulations predict a slightly shifted stability area. For the combination of an

electron lens and LHC-like octupoles we obtain a large stable area close to the analytical estimation of Eq. 5.23.

Overall we observe a good agreement between the simulated stability boundaries and the ones obtained from the dispersion relation. Additionally, one observes a clear benefit (in terms of enlargement of a stable area) to combining two different sources of transverse detuning with each other. This gives confidence in the dispersion relation Eq. (5.23) for FCC-hh conditions.

6.2.3 Stability boundaries from longitudinal and transverse detuning
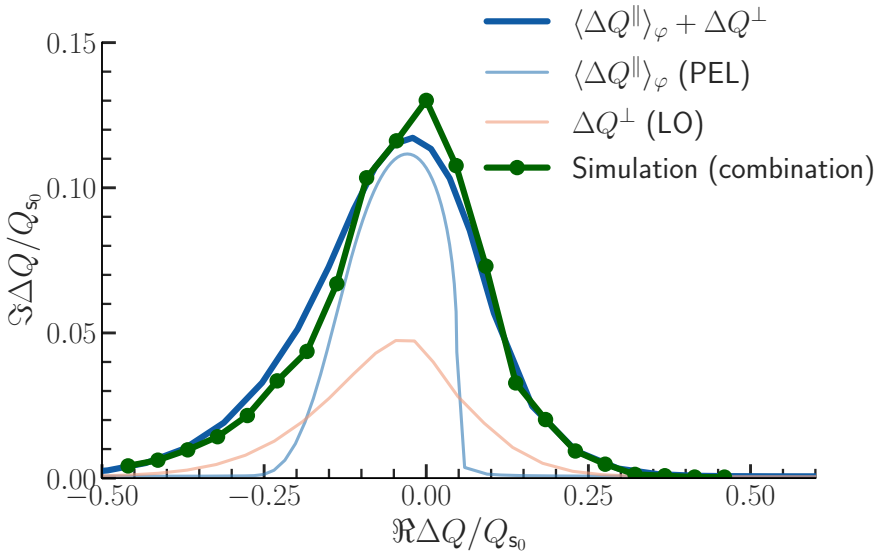

Figure 6.6: Stability diagrams for the head-tail mode $l = 0$ from Eq. (5.23) for LO (transverse detuning $\Delta Q_y^\perp(J_x, J_y)$, light-yellow line), for a PEL (longitudinal detuning $\langle \Delta Q_y^\parallel(J_z) \rangle_\varphi$, light-blue line), and for the related combination (dark-blue line). The corresponding simulation results for the device combination is shown by the green curve.

In this work, the dispersion relations are generalised to include both transverse and longitudinal detuning (see Chapter 5). To the best of our knowledge, this situation was not treated analytically in the literature before. In this section, the results of Chapter 5 are confirmed by particle tracking simulations.
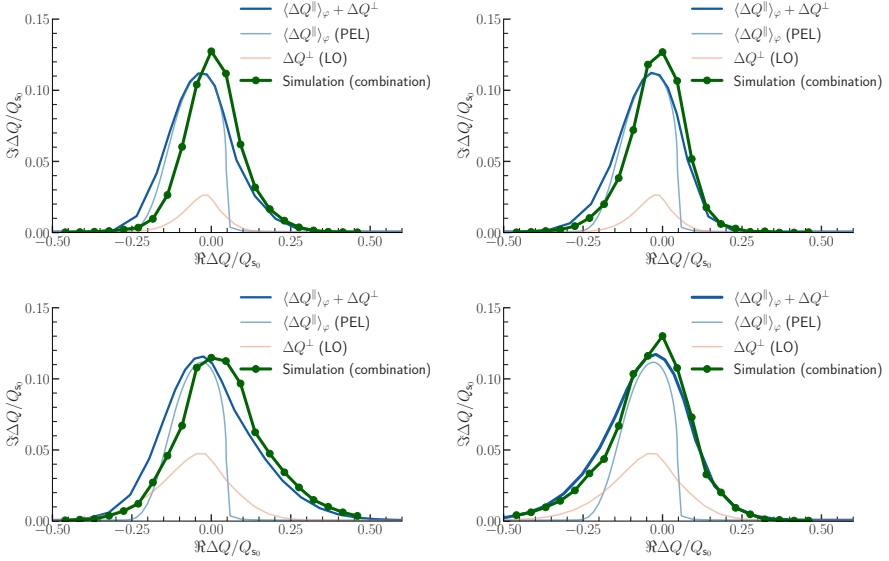
Figure 6.7: Stability boundaries for combinations of a PEL with LO. Simulations (green) are compared to analytical estimations (blue and yellow). The strength of PEL is kept constant for all four subfigures. The strength and polarity of LO are varied in the following way: (top left) weak LO ($\approx .45$ of the maximal tune spread) with opposite polarity; (top right) weak LO; (bottom left) LO strengths (1.0 of the maximal tune spread) matches Fig. 6.6 but the polarity is switched; (bottom right) LO parameters match Fig. 6.6.

Figure 6.6 shows Landau damping from a combination of a PEL and LO from the results of the simulation scans (green) and from the dispersion relation Eq. (5.23) (dark-blue). The light-blue and the light-yellow lines show the stability diagram from the dispersion relation for the cases with a PEL only and LO only. For both devices, the same settings as in Fig. 6.3 are applied. The stability boundary (if compared to a PEL one only) increases in the tails and becomes wider. This device combination helps to mitigate instabilities for a broader range of real coherent tune shifts $\Re\Delta Q_{\text{coh}}$ but not the instabilities with a higher growth rate $\Im\Delta Q_{\text{coh}}$. In a comparison with the LO only case, the device combination mitigates the instabilities with the nearly doubled growth rate, and in the similar range for the real coherent tune shifts.

Figure 6.7 compares combinations of a PEL with LO for different strength and polarity of LO. The results presented in these figures match our analytical calculations. Combin-

ing a PEL with LO increases the stability boundary in all presented cases. The stability boundary is increased in terms of stabilised real coherent tune shifts.

In summary, in this Chapter we have demonstrated Landau damping from several sources of longitudinal and transverse detuning. The coherent properties of longitudinal and transverse detuning were compared to each other and to the analytical estimations presented in Chapter 5. New findings of Chapter 5 for a combination of transverse and longitudinal detuning have been confirmed with particle tracking simulation approach. For this, a combination of a PEL and LO was used. This combination is a possible option to mitigate transverse instabilities in SIS100.

7 Numerical studies: Nonzero head-tail modes

The majority of the numerical results presented in this chapter are published by the author in [111]. Some additional results are presented here either to support the conclusions of [111] or to provide more details on the methods.

7.1 Resistive wall impedance model

With the modes from Section 6.1 we can only consider head-tail mode zero. In order to investigate the Landau damping of higher order head-tail modes we will use a resistive wall impedance model (see Subsection 2.3.5). The resistive wall impedance of the beam pipe is one of the major sources of impedance and is present in many synchrotrons. The value of the chromaticity determines which head-tail mode is the most unstable (with a fastest growth rate). We will scan different chromaticities to find several head-tail
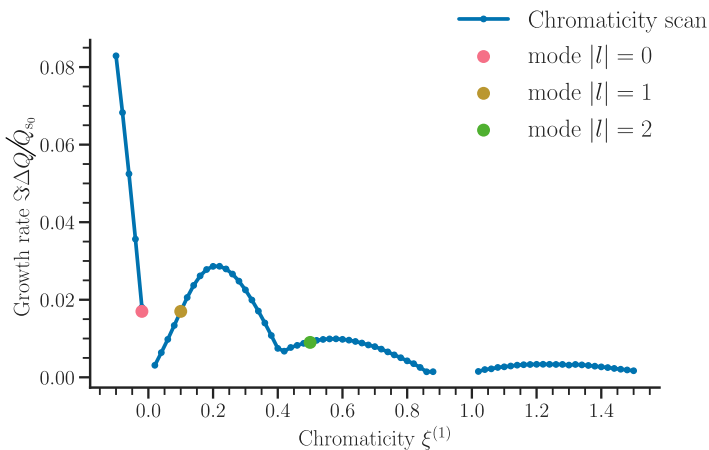
Figure 7.1: Scan of the head-tail instability growth rate vs (linear) chromaticity. Each point on the plot corresponds to a tracking simulation.

$\xi^{(1)}$	l	$\Re\Delta Q_{\text{inst}}/Q_{s_0}$	$\Im\Delta Q_{\text{inst}}/Q_{s_0}$	Machine Parameters	
-0.02	0	-0.530	0.017	η	3.45×10^{-4}
0.1	-1	-0.052	0.017	Q_{s_0}	1.74×10^{-3}
0.5	-2	-0.017	0.009	$N_{\text{macro}}/N_{\text{turns}}$	$10^5/10^5$

Table 7.1: Simulation and machine parameters for the wakefield driven instability simulations. The coherent tune shifts are for the case with no Landau damping.

instabilities of different order. Then, the instabilities with similar growth rates will be chosen to study Landau damping of higher order head-tail modes.

Figure 7.1 displays a simulation scan of transverse instability for different chromaticity values. All other beam and machine parameters are kept constant. The slip factor η is positive, meaning that the beam energy is above the transition energy. The simulations were performed for over 150 synchrotron periods. We observe a high growth rate for negative chromaticity values, corresponding to mode $l = 0$. For positive chromaticities, $\xi^{(1)} < 0.4$ we observe mode $|l| = 1$. When $0.4 < \xi^{(1)} < 0.8$ the mode $|l| = 2$ is observed. The beam is stable for zero chromaticity $\xi^{(1)} = 0$. This plot represents the convolution between the beam coupling impedance and the head-tail mode spectrum.

This section investigates the Landau damping of wakefield driven instabilities from a PEL, with the focus on nonzero head-tail modes. Thresholds of the instability suppression of a PEL are compared with the ones for LO, a DC EL and an RFQ. The resistive wall impedance $Z_y^\perp \propto 1/\sqrt{Q_p}$, relevant for many hadron accelerators (e.g. [42], [79]), is used in this section.

Relevant machine and beam parameters for the simulation results of this section are summarised in Table 7.1. The bunch distribution Gaussian transversely and longitudinally. A linear RF bucket is used in the simulations, thus the synchrotron frequency detuning is not taken into account. We identify several linear chromaticity settings where the head-tail modes $l = \{0, -1, -2\}$ are unstable. The instability coherent tune shifts and chromaticity settings are given in Table 7.1. Frequency spectra and characteristic intrabunch motion of these instabilities are illustrated in Fig. 7.2.

The mode spectra maxima are near the related synchrotron sidebands, indicating the azimuthal mode number l for each mode. A characteristic head-tail pattern with the $|l|$ number of nodes in the offset trace plots is observed. Each instability has an exponential growth of the transverse offset. The instability parameters are chosen to be well below the threshold of the Transverse Mode Coupling Instability (TMCI), an instability due to coupling between different modes.

7.2 Landau damping of wakefield driven head-tail instabilities

Our particle tracking simulation results (solid lines) for Landau damping of head-tail modes $l = \{0, -1, -2\}$ are demonstrated in Figs. 7.3, 7.4, 7.5, where we compare it to
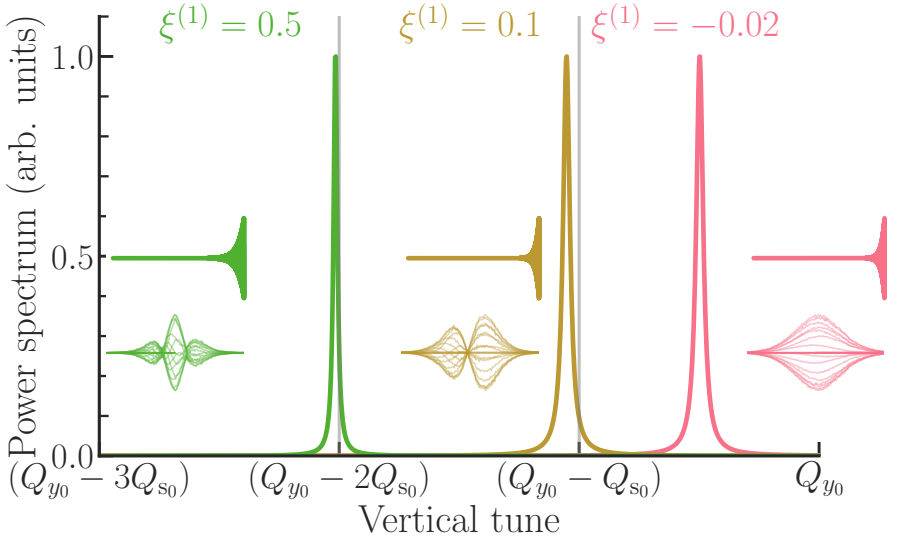
Figure 7.2: Spectra and the trace plots of the centroid motion for head-tail instabilities for three head-tail modes $l = 0$ (red lines), $l = -1$ (yellow lines), $l = -2$ (green lines) observed in the simulations. These are the instabilities when both the longitudinal and the transverse detuning are zero.
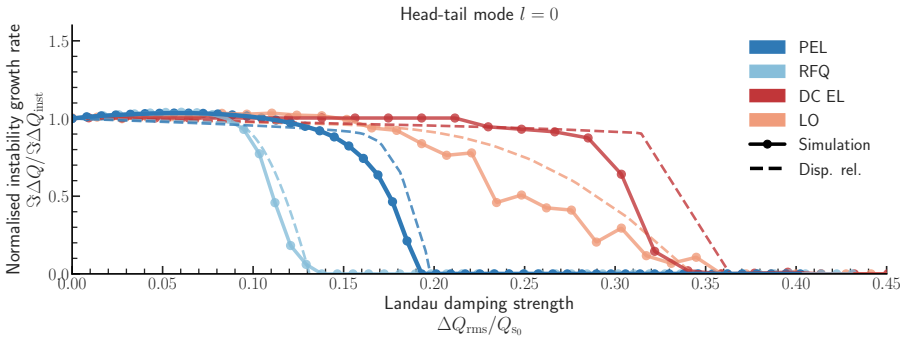

Figure 7.3: Instability growth rate (in simulations) dependency on the strength of Landau damping $\Delta Q_{\mathrm{rms}}/Q_{\mathrm{s_0}}$ for head-tail mode $l = 0$. A PEL (dark-blue), LO (yellow), a DC EL (red), an RFQ (light-blue) simulation results are compared with respective dispersion relations Eq. (5.23).
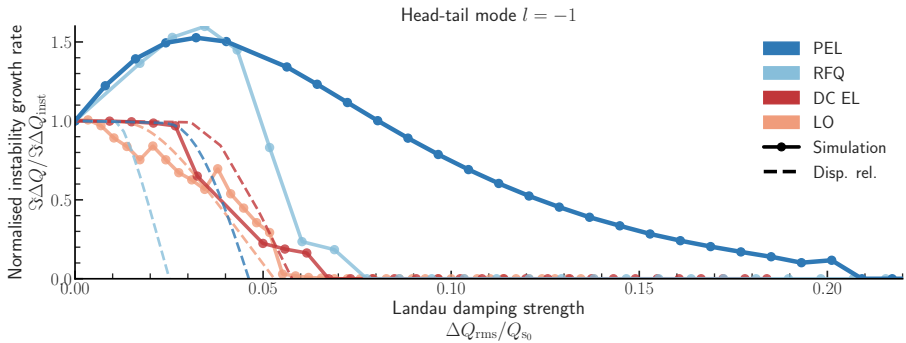
Figure 7.4: Instability growth rate (in simulations) dependency on the strength of Landau damping $\Delta Q_\text{rms}/Q_{s_0}$ for head-tail mode $l = -1$. A PEL (dark-blue), LO (yellow), a DC EL (red), an RFQ (light-blue) simulation results are compared with respective dispersion relations Eq. (5.23).

Figure 7.5: Instability growth rate (in simulations) dependency on the strength of Landau damping $\Delta Q_\text{rms}/Q_{s_0}$ for head-tail mode $l = -2$. A PEL (dark-blue), LO (yellow), a DC EL (red), an RFQ (light-blue) simulation results are compared with respective dispersion relations Eq. (5.23).
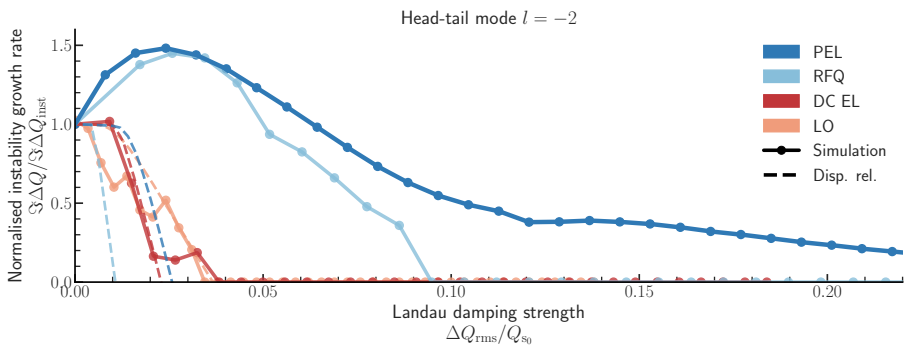
the analytical predictions (dashed lines) of Eq. (5.23). It does not account for the effective impedance modification by the longitudinal detuning. Therefore, if this effect is significant for the head-tail modes of a Gaussian bunch, we will observe a disagreement between Eq. (5.23) and the simulation results. Also, four betatron frequency detuning devices are compared to each other: a PEL (dark-blue), an RFQ (light-blue), a DC EL (red), LO (yellow). For our particle tracking scans, we iteratively increase the strength of Landau damping for each identified head-tail mode setting from Table 7.1. The strength of Landau damping is expressed by the rms betatron tune spread ΔQ_{rms} to allow a comparison between the devices. It is normalised by the synchrotron tune Q_{s_0}. Because this is proportional to the scaling parameter of the betatron phase factor from Eq. (5.10). The instability growth rate is normalised by its value in the absence of betatron frequency detuning $\Im \Delta Q_{\mathrm{inst}}$ (see Table 7.1).

The simulation results for the head-tail mode $l = 0$ are presented in Fig. 7.3. One observes a good agreement with Eq. (5.23) both for the stability threshold and for the evolution of the instability growth rate. No significant effective impedance modification due to the longitudinal detuning (a PEL, an RFQ) is observed for the zero head-tail mode.

Figures 7.4, 7.5 demonstrate particle tracking results for head-tail modes $l = \{-1, -2\}$. For the transverse detuning (LO, a DC EL) the threshold for the instability suppression agrees with the dispersion relation Eq. (5.23). For the longitudinal detuning (a PEL, an RFQ), in the simulation the threshold of the instability suppression is higher than expected from Eq. (5.23). For example, for a PEL the threshold of $\Delta Q_{\mathrm{rms}}/Q_{s_0} \approx 0.2$ is observed in the simulation, whereas analytically we expect a lower value $\Delta Q_{\mathrm{rms}}/Q_{s_0} \approx 0.05$. This indicates that there is a destabilising effect from a PEL and an RFQ for the head-tail modes $l = \{-1, -2\}$. In Section 5 this was identified as the effective impedance modification due to the longitudinal detuning. The stronger effective impedance modification for nonzero head-tail modes was already indicated by Fig. 5.3. In contrast, transverse detuning from LO or a DC EL agrees with the dispersion relation Eq. (5.23) regardless of the head-tail mode number and its longitudinal structure.

The interplay between the effective impedance modification and Landau damping for the head-tail mode $l = -1$ is illustrated in Fig. 7.6. The same instability parameters as in Fig. 7.4 were used. This illustrates two effects: first, stability boundary (solid and dashed lines for Eqs. (5.22, 5.23) respectively) is increasing due to Landau damping; second, the instability coherent tune shift from Eq. (5.21) gets further away from this boundary due to the effective impedance modification. In the calculation we used airbag bunch head-tail mode spectrum as an approximation. In Fig. 7.6 two PEL rms tune spread values are presented. First, at $\Delta Q_{\mathrm{rms}}/Q_{s_0} = 0.05$ (magenta colour), is the stability threshold estimated from Eqs. (5.22, 5.23). In this situation, the instability coherent tune shift, without the head-tail mode spectrum modification by a PEL, lies inside the stability boundary. Unlike the coherent tune shift from Eq. (5.21) which account for head-tail mode modification. New stability threshold (cyan colour) is then at the PEL rms tune spread of $\Delta Q_{\mathrm{rms}}/Q_{s_0} = 0.07$. In this situation the effective impedance modifica-
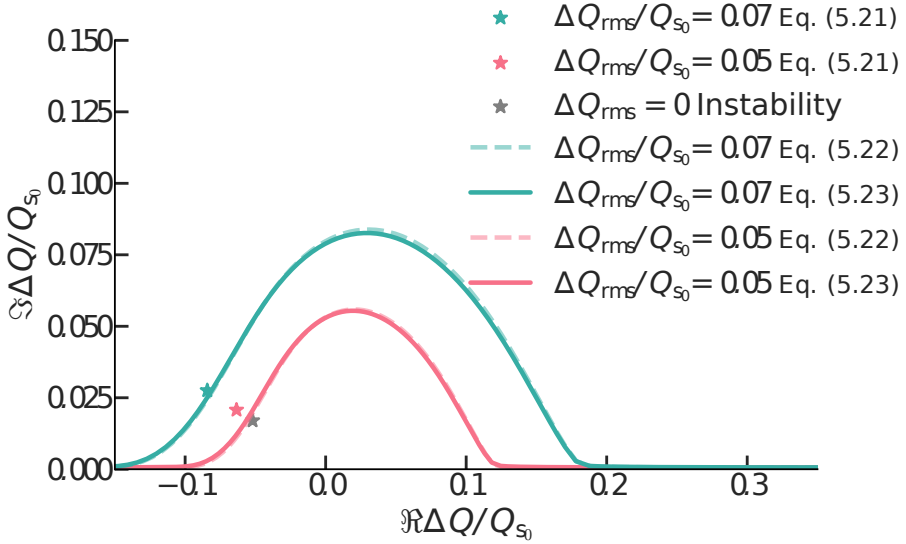
Figure 7.6: Stability boundaries for several PEL strengths for the mode $l = -1$ (solid lines) from Eqs. (5.22, 5.23) and respective coherent tune shifts of the instability (dots) from Eq. (5.21). Machine and beam parameters are the same as in Fig. 7.4. Two Landau damping strength $\Delta Q_{\mathrm{rms}}/Q_{s_0} = \{0.05, 0.07\}$ are considered (magenta and cyan colours respectively).

tion, illustrated as a shift of the coherent frequency, is $\approx 86\%$. At the same PEL strength, albeit for the head-tail mode $l = 0$ it is $\approx 1\%$. The instability suppression threshold for the head-tail mode $l = -1$ in the simulation is significantly higher at $\Delta Q_{\mathrm{rms}}/Q_{s_0} \approx 0.2$. This discrepancy could be due to several approximations that were made. First, we approximated the head-tail mode spectrum with the one of an airbag bunch. Second, dispersion relations Eqs. (5.22, 5.23) were derived for a delta-function like narrow band impedance. However, the resistive wall impedance is inversely proportional to the frequency $\propto 1/\sqrt{Q_p}$. It has a delta-function like behaviour only approximately.

7.3 Stability boundaries from a combination of a PEL and the transverse detuning

A combination of transverse and longitudinal detuning can also be studied using the wakefield driven instability.
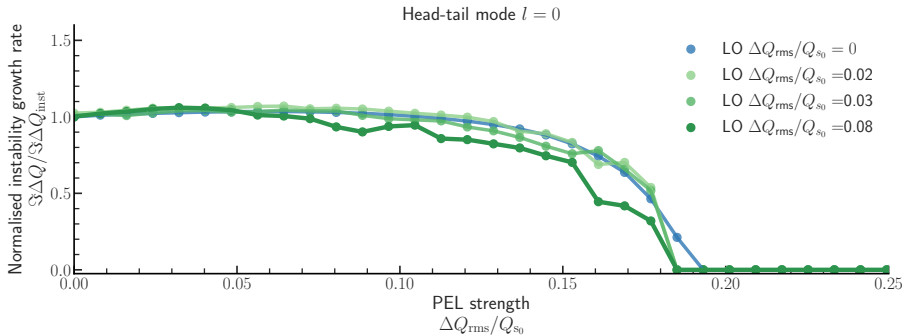
Figure 7.7: Landau damping of head-tail mode $l = 0$ with a combination of a PEL and LO in the simulations. The growth rate of the instability is plotted against the strength of a PEL, expressed as the rms tune spread normalised by the synchrotron tune. Landau damping from only a PEL (blue) is compared to its combination with several LO for several strength of the LO (green curves).

In Fig. 7.7 the influence of combining a PEL with LO on Landau damping of head-tail mode $l = 0$ is demonstrated. For the $l = 0$ mode coherent tune shift (see Table 7.1), the threshold for instability suppression stays constant for different strength of LO. Therefore, for this particular instability there is no benefit in adding LO to a PEL.

Figure 7.8 demonstrates Landau damping of head-tail mode $l = -1$ for several combinations of a PEL and LO. The effective impedance modification comes solely from the dynamic part of the longitudinal detuning (see Eqs. (5.10, 5.16)). Landau damping in this case is improved, like in the case of zero head-tail mode in Fig. 6.6. Similarly to the case of only longitudinal detuning in Fig. 7.4, 7.5, with increasing rms tune spread the beam is stabilised. Figure 7.8 demonstrates that it could be beneficial to combine a PEL with LO for Landau damping of higher-order head-tail modes. However, the effective impedance modification should be carefully taken into account.

One of the questions that was left open in Chapter 5 is a combination of transverse and longitudinal detuning in a single device. This would mean that the tune shifts due to this device are expressed as $\Delta Q(J_x, J_y, J_z, \varphi)$ and Eqs.(5.22, 5.23) are no longer valid. This tune shift can be achieved practically by pulsing the current of a DC EL with a transversely nonlinear electron beam (Gaussian-like distribution, for example). Such a device is a combination of a PEL and a DC EL.

Figure 7.9 demonstrates particle tracking simulation results for this hypothetical device in comparison to a DC EL, a PEL, LO and an RFQ. Beam and machine parameters close to that of Table 7.1 were used in the simulations. The results for a transversely Gaussian PEL are demonstrated in green.
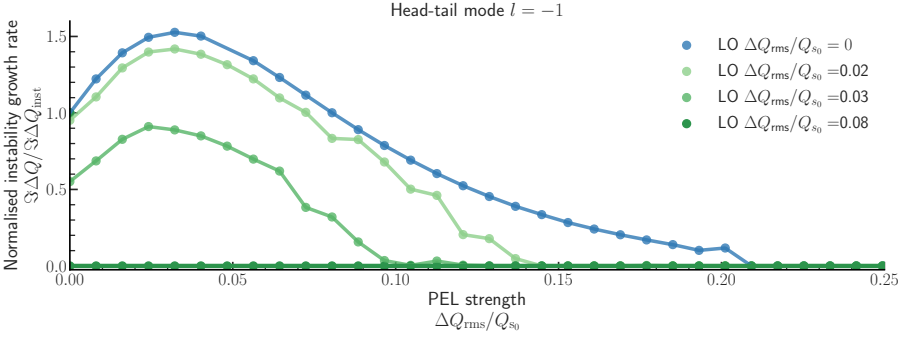
7.3 Stability boundaries from a combination of a PEL and the transverse detuning   91

Figure 7.8: Landau damping of head-tail mode $l = -1$ with a combination of a PEL and LO in the simulations. The growth rate of the instability is plotted against the strength of a PEL, expressed as the rms tune spread normalised by the synchrotron tune. Landau damping from only a PEL (blue) is compared to its combination with LO for several strengths of the LO (green curves).
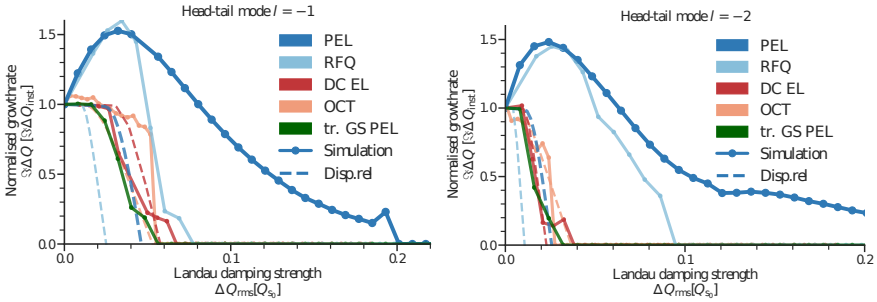

Figure 7.9: Instability growth rate (in simulations) dependency on the strength of Landau damping $\Delta Q_{\mathrm{rms}}/Q_{s_0}$ for head-tail mode $l = -1$ (left) and $l = -2$ (right). A PEL with homogeneous transverse distribution of electron beam(dark-blue), LO (yellow), a DC EL (red), an RFQ (light-blue), a PEL with Gaussian transverse distribution of electron beam results are compared with respective dispersion relations Eq. (5.23).

From these results, we can preliminary conclude that a PEL with an electron beam with a Gaussian transverse distribution has approximately the same threshold as a DC EL. No destabilising or stabilising effect on the effective impedance is observed. This can be, preliminary, explained due to a modification of B-function (see Eq. (5.10)). For a PEL with homogeneous transverse distribution of electrons, $B(J_z, \varphi)$, all particles with a longitudinal amplitude J_z have the same dynamic part of the tune shift. On the other hand, for an electron beam with a Gaussian transverse distribution, $B(J_x, J_y, J_z, \varphi)$, all of the particles with a longitudinal amplitude J_z have a different dynamic part of the tune shift. The resulting difference in dynamic tunes between particles then is presumably negligible.

8 Conclusions and Outlook

The PEL as a source of the longitudinal detuning has been introduced. Its effects on transverse beam stability have been demonstrated. A Vlasov formalism was used to derive new dispersion relations Eqs. (5.22, 5.23) for a linear combination of the transverse and the longitudinal detuning. There are two distinct effects of the PEL (or other longitudinal detuning) on the transverse beam stability: Landau damping due to the static component of the detuning; and the head-tail mode distortion due to the dynamic component of the detuning, see Eq. (5.5).

The head-tail mode distortion is the origin of the effective impedance modification [72], as it is explained in Chapter 5, see Fig. 5.3 and Eqs. (5.10, 5.17). In contrast, for a transverse detuning there is no effective impedance modification and only Landau damping is affected. These analytical results were confirmed for a Gaussian bunch with particle tracking in Chapters 6, 7 for three different head-tail modes and compared to the stability boundaries of LO, a DC EL, an RFQ.

The betatron phase factor was demonstrated to vary along the bunch in the presence of the longitudinal detuning, see Eq. (5.10) and Fig. 5.1. This variation relates the PEL dynamic longitudinal detuning to the dynamic longitudinal detuning due to higher-order chromaticity [72] and the RFQ [71].

Figure 5.3 displays how the head-tail mode spectrum is affected depending on the strength of the longitudinal detuning from a PEL. The sum in Eq. (5.17) describes the head-tail modes in the presence of the longitudinal detuning; a similar sum representation exists for any longitudinal detuning.

The ratio $\Delta Q_{\mathrm{max}}/Q_{s_0}$ determines the strength of the effective impedance modification by the longitudinal detuning. In the weak regime $\Delta Q_{\mathrm{max}}/Q_{s_0} \lesssim 1$, only the zero head-tail mode is described well by the dispersion relation Eq. (5.23), see Fig. 7.3. The rigid mode kick model was shown to reconstruct the shape and the magnitude of the stability boundaries, see Fig. 6.3. For the zero head-tail mode, Landau damping either with transverse or longitudinal detuning is equally effective for a given rms tune spread ΔQ_{rms}, see Fig. 6.3. The simulation results for the zero head-tail mode (see Fig. 6.4) indicate that with a DC EL it is possible to adjust the stability boundary by changing the electron to ion beam size ratio.

The nonzero head-tail modes are described by Eqs. (5.21, 5.22) which include the effective impedance modification, leading to the instability amplification, see Figs. 5.3, 7.4. This is a significant effect for nonzero modes, neglected by Eq. (5.23). The instability becomes stronger because some modes are getting weaker and other modes are amplified; see Fig. 5.3. For the nonzero head-tail modes Landau damping with longitudinal detuning requires rms tune spreads ΔQ_{rms} up to 2-5 times larger than

predicted by the dispersion relation Eq. (5.23) due to the destabilising effect of the effective impedance modification (see Figs. 7.4, 7.5). Landau damping with transverse detuning, on the contrary, does not have this effect and is described by the dispersion relation Eq. (5.23).

In the strong lens regime $\Delta Q_{\mathrm{max}}/Q_{s_0} \gg 1$, the instability is shifted towards higher-order modes with a smaller growth rate, see Fig. 5.3. This is the regime foreseen for a PEL in the SIS100 as a space-charge compensation device [35]. Due to the large mode spectrum modification by PEL, expressions of Eq. (5.21, 5.22) should be used instead of Eq. (5.23). Landau damping is stronger for a larger rms tune spread. Therefore, both Landau damping and the effective impedance modification from a PEL are stabilising in this regime.

The complex interplay between a PEL and space-charge is beyond the scope of the present work. In [116], the feasibility of Landau damping with a DC EL in space-charge dominated beams was demonstrated. For a PEL, the same argumentation should be valid for the static component of the detuning; while the dynamic component of the detuning should lead to a weaker head-tail instability, see Fig. 5.3 (bottom).

Combinations of transverse and longitudinal detuning devices are expected in several hadron accelerators. SIS100 is foreseen [52] to have both, a PEL and LO. For the LHC, a combination of LO and an RFQ was recently proposed [76]. We have derived new integral equations Eqs. (5.20, 5.21) and dispersion relations Eqs. (5.22, 5.23) for the combinations of transverse and longitudinal detuning and for arbitrary bunch profiles. Those dispersion relations are an extension of Eq. (31) in [72], where the transverse detuning is not included. Our dispersion relation Eq. (5.22) simplifies to Eq. (5.23) for a situation with the assumptions discussed at the end of Section 5. Finally, our dispersion relation Eq. (5.23) reduces to the Eqs. (1, 2) from [75] for either longitudinal or transverse detuning. Stability boundaries due to a PEL, LO and their combination are given and verified with simulation results, see Figs. 6.3, 6.6. A transversely nonlinear PEL is not covered in this contribution, see Section 5, Eq. (5.11) and discussion therein. One can presume that Landau damping will stay approximately the same for equivalent rms tune spreads regardless of whether the lens is pulsed. However, the effective impedance modification of head-tail modes is not trivial in this case. Nonlinear synchrotron oscillations were not taken into account in this contribution but could be relevant for SIS100 operation with longer bunches.

Additionally, SIS18 experiments on coherent beam stability of coasting (unbunched) beam were performed during two dedicated beam time slots. During the experiments, an existing SIS18 electron cooler was used as a DC EL. Using this electron cooler as a PEL is not possible. $^{40}\mathrm{Ar}^{18+}$ and $^{40}\mathrm{Ar}^{10+}$ beams were used with the highest available intensity. First, with $^{40}\mathrm{Ar}^{18+}$ an instability was observed and reproduced for a specific (linear) chromaticity. Then it was demonstrated that this instability can be suppressed by increasing the current of a DC EL. Second, with $^{40}\mathrm{Ar}^{10+}$ beam, two different instabilities were observed and reproduced for different currents of a DC EL. The observed instabilities in both cases are suspected to be two-stream instabilities.

These experiments need to be repeated when a PEL prototype and higher beam intensities will be available in the SIS18. Suppose the two-stream instability was caused by a DC EL. In that case, its threshold needs to be studied for the parameters of PEL prototype. This is a potential limiting factor for the electron beam current in a single PEL. A potential cure of the instability, if caused by a PEL, is increasing the strength of the magnetic field in the main solenoid of the lens. These studies with the prototype lens are also necessary to understand the complex interaction with space charge and possible incoherent losses.

In summary, we presented an analytical description of Landau damping due to a linear combination of transverse and longitudinal detuning. Coherent properties of longitudinal detuning and transverse detuning, and Landau damping due to four devices (PEL, DC EL, LO, RFQ), were compared in detail. The feasibility of a DC EL for Landau damping was demonstrated experimentally. Additionally, a potential limiting factor for a DC EL and for a PEL in SIS18/SIS100 operation was discussed. The application of a PEL in different settings for Landau damping was demonstrated. We showed that the effective impedance due to longitudinal detuning significantly affects the beam stability, especially for nonzero head-tail modes. The results from analytical considerations are verified using particle tracking simulations.

Lists

List of Figures

List of Tables

List of Acronyms

AC   Alternating current

APPA   Atomic, Plasma Physics and Applications

BNL   Brookhaven National Laboratory, Upton NY

BPM   Beam position monitor

CBM   Compressed barionic matter

CERN   European Organization for Nuclear Research

DC EL   DC Electron Lens

DC   Direct current

DCCT   Direct-current current transformer

ERL   Energy Recovery Linac

FAIR   Facility for Antiproton and Ion Research in Europe GmbH

FCC-hh   Future Circular Collider (hadron-hadron option)

FEL   Free Electron Laser

FFAG   Fixed Field Alternating Gradient accelerator

FODO   Focusing - drift space - Defocusing - drift space

FNAL   Fermi National Accelerator Laboratory, Batavia IL

GSI	Helmholtzzentrum für Schwerionenforschung GmbH
IPM	Ionisation Profile Monitor
LHC	Large Hadron Collider
LO	Landau Octupoles
NUSTAR	Nuclear Structure, Astrophysics and Reactions
NuPECC	The Nuclear Physics European Collaboration Committee
KV	Kapchinskij-Vladimirskij
PANDA	Antiproton Anihilation at Darmstadt
PEL	Pulsed Electron Lens
PS	Proton Synchrotron
P.V.	Principal value
RANSAC	Random Sample Consensus algorithm
RFQ	Radio Frequency Quadrupole Cavity
RF	Radio Frequency
RHIC	Relativistic Heavy Ion Collider
SIS100	Schwerionensynchrotron 100 (ger. for heavy ion synchrotron 100)
SIS18	Schwerionensynchrotron 18 (ger. for heavy ion synchrotron 18)
SPS	Super Proton Synchrotron
Super-FRS	Superconducting Fragment Separator
TEMF	Institute for Accelerator Science and Electromagnetic fields
TMCI	Transverse Mode Coupling Instability
TU Darmstadt	Technische Universität Darmstadt
UNILAC	Universal Linear Accelerator
fft	Fast Fourier transform

linac   Linear Accelerator

p-linac   Proton Linear Accelerator

rms   Root Mean Squared

Nomenclature

$\psi_{\hat{\beta}_{x,y}}(s)$ Horizontal and vertical betatron phase advance

$\alpha_c^{(n)}$ Higher order momentum compaction factor

α_c Momentum compaction factor (linear)

$\eta, \eta^{(1)}$ Slip factor (linear)

$\eta^{(n)}$ Higher order slip factor

γ_t Relativistic gamma for the transition energy

$\hat{\alpha}_{x,y}$ Twiss alpha function

$\hat{\beta}_z$ Longitudinal (Twiss) beta function

$\hat{\beta}_{x,y}$ Twiss beta function

$\hat{\gamma}_{x,y}$ Twiss gamma function

Ω_s Synchrotron frequency

ψ_s Synchronous phase

$\xi, \xi^{(1)}$ Linear chromaticity

$\xi^{(2)}$ 2nd order chromaticity

$\xi^{(n)}$ nth order chromaticity

$B\rho$ Beam rigidity

C Accelerator circumference

E_{inj} Injection energy

f_{rev} Revolution frequency

h_{RF} RF harmonic

$K_x(s)$	Horizontal focusing function
$K_y(s)$	Vertical focusing function
$Q'_{x,y}$	Not normalised linear chromaticity
Q_{s,s_0}	Synchrotron tune
Q_{x_0,y_0}	Horizontal and vertical betatron tune
R	Effective radius of the accelerator
V_0	Maximum RF cavity voltage
V_{RF}	RF Voltage
$\lambda(\omega)$	Beam oscillation mode
ω_0	Angular revolution frequency
ϕ	Longitudinal phase
$\psi_{\hat{\beta}_{x,y}}$	Betatron phase (horizontal, vertical)
σ_z	rms bunch length
τ	Arrival time
$\theta_{\hat{\beta}_{x,y}}$	Betatron phase offset
ε_z	Longitudinal (geometrical) rms emittance
$\varepsilon_{x,y}$	Transverse (geometrical) rms emittance
$A_{x,y}$	Horizontal and vertical particle amplitudes
E_0	Reference particle energy
N_{cycle}	Intensity in ions per cycle
p_0	Reference particle momentum
q	Charge of the reference particle
$r_\perp$	Transverse distance to the reference particle trajectory
v_0	Reference particle velocity

$w_{x,y}(s)$ Horizontal and vertical envelope functions

Z Charge number of the ion

Ψ Distribution function (in phase space)

R_l Radial function of the mode l

δ Particle momentum deviation from the reference particle

$\theta_{x,y}$ Angle variable, conjugate variable to action-variable

φ Longitudinal angle variable

$\vec{X}(s)$ 6D vector of particle coordinates in phase space

J_z Longitudinal action variable

$J_{x,y}$ Action-variables, invariant of motion

p_0 Projection of particle momentum on y-axis

p_x Projection of particle momentum on x-axis

s Location in the accelerator

x' Horizontal particle momentum in the moving frame

x Horizontal particle coordinate in the moving frame

y' Vertical particle momentum in the moving frame

y Vertical particle coordinate in the moving frame

z Longitudinal particle coordinate in the moving frame

β_e Relativistic beta of electrons in electron cooler

$\Delta Q_{\max}$ Maximal betatron tune shift due to electron lens

σ_e Rms electron beam size

$\sigma_{e_{\parallel}}$ Electron current pulse rms length

$\sigma_{e_{\perp}}$ Transverse rms electron beam size

B_{gun} Magnetic field on the electron gun

Nomenclature   **107**

B_{int} Magnetic field in the interaction region

$f_{\text{exp}} = \frac{B_{\text{gun}}}{B_{\text{int}}}$ Adiabatic expansion factor

I_{max} Maximal current of the electron beam

j_e Electron current density

U_e Electron kinetic energy in electron cooler

χ Betatron phase factor for linear chromaticity

$\Delta Q^{\parallel}$ Longitudinal detuning, betatron tune shift with longitudinal coordinates

$\Delta Q^{\perp}$ Transverse detuning, betatron tune shift with transverse amplitudes

ΔQ_{coh} Coherent tune shift

$\Delta Q_{x,y}$ Betatron tune shift

Δ_y Maximum vertical amplitude

ϵ Order of the perturbation

$\Im x$ Imaginary part of some complex quantity x

λ_l Dipolar moment of the head-tail mode l

$\mathcal{H}$ Hamiltonian of longitudinal and transverse particle motion

$\mathcal{H}_{\parallel}$ Hamiltonian of the longitudinal motion

$\mathcal{H}_{\text{PEL}}$ PEL interaction part of the Hamiltonian

$\mathcal{H}_{\text{wake}}$ Wakefield interaction part of the Hamiltonian

$\Psi_1(J_x, \theta_x, J_y, \theta_y, J_z, \varphi, t)$ Perturbation part of the distribution function

$\Re x$ Real part of some complex quantity x

A_l Amplitude of oscillations of mode l

$a_{xx,xy,yx,yy}$ Octupole detuning coefficients

$B(J_z, \varphi)$ Generalised betatron phase factor

B'_u Gradient of the magnetic field

H_l^p	Airbag bunch head-tail modes
$H_l^{p^\dagger}$	Complex conjugate of airbag bunch head-tail modes
L	Length of the reference particle orbit
$N, N_{\text{particles}}$	Number of particles in a beam
$N_{\text{m.p.}}$	Number of macroparticles
$N_{\text{per slice}}$	Number of macroparticles per slice
N_{slices}	Number of slices
O_3	Strength of the octupole magnets
T_0	Revolution period
V_0	Maximal RF voltage
v_i	Speed of the particle
$\mathscr{H}_\perp$	Hamiltonian of the transverse motion
ϵ_0	Permittivity of the free space
μ_0	Permeability of the free space
c	Speed of light
e	Elementary electric charge
m_e	Mass of the electron
m_p	Mass of the proton
q	Electric charge
r_e	Classical electron radius
r_p	Classical proton radius
$\Delta\vec{p}$	Momentum change due to the wakefield
$\Delta\vec{p}_\perp$	(Transverse projection) momentum change due to the wakefield
δ_{skin}	Skin depth

ρ Conductivity of the beam pipe material

b Radius of the beam pipe

L Length of the beam pipe

M_m mth multipole moment of the source particle

W'_m Longitudinal wake function of azimuthal m

W_m Transverse wake function of azimuthal m

$Z_m^{\parallel}$ Longitudinal beam coupling impedance of the azimuth m

$Z_m^{\perp}$ Transverse beam coupling impedance of the azimuth m

Z_{eff} Effective impedance

Z_{machine} Machine (beam coupling) impedance

Bibliography

[1] S. Chatrchyan, V. Khachatryan, A. M. Sirunyan, *et al.*, "Observation of a new boson at a mass of 125 GeV with the CMS experiment at the LHC", *Physics Letters, Section B: Nuclear, Elementary Particle and High-Energy Physics*, vol. 716, no. 1, pp. 30–61, 2012. doi: 10.1016/j.physletb.2012.08.021 (cit. on p. 1).

[2] G. Aad, T. Abajyan, B. Abbott, *et al.*, "Observation of a new particle in the search for the Standard Model Higgs boson with the ATLAS detector at the LHC", *Physics Letters, Section B: Nuclear, Elementary Particle and High-Energy Physics*, vol. 716, no. 1, pp. 1–29, 2012. doi: 10.1016/j.physletb.2012.08.020 (cit. on p. 1).

[3] G. W. Bennett, B. Bousquet, H. N. Brown, *et al.*, "Final report of the E821 muon anomalous magnetic moment measurement at BNL", *Physical Review D*, vol. 73, no. 7, p. 072 003, Apr. 2006. doi: 10.1103/PhysRevD.73.072003 (cit. on p. 1).

[4] T. Albahri, A. Anastasi, K. Badgley, *et al.*, "Beam dynamics corrections to the Run-1 measurement of the muon anomalous magnetic moment at Fermilab", *Physical Review Accelerators and Beams*, vol. 24, no. 4, p. 044 002, Apr. 2021. doi: 10.1103/PhysRevAccelBeams.24.044002 (cit. on p. 1).

[5] T. Albahri, A. Anastasi, K. Badgley, *et al.*, "Magnetic-field measurement and analysis for the Muon $g-2$ Experiment at Fermilab", *Physical Review A*, vol. 103, no. 4, p. 042 208, Apr. 2021. doi: 10.1103/PhysRevA.103.042208 (cit. on p. 1).

[6] T. Albahri, A. Anastasi, A. Anisenkov, *et al.*, "Measurement of the anomalous precession frequency of the muon in the Fermilab Muon $g-2$ Experiment", *Physical Review D*, vol. 103, no. 7, p. 072 002, Apr. 2021. doi: 10.1103/PhysRevD.103.072002 (cit. on p. 1).

[7] B. Abi, T. Albahri, S. Al-Kilani, *et al.*, "Measurement of the Positive Muon Anomalous Magnetic Moment to 0.46 ppm", *Physical Review Letters*, vol. 126, no. 14, p. 141 801, Apr. 2021. doi: 10.1103/PhysRevLett.126.141801 (cit. on p. 1).

[8] T. Aoyama, N. Asmussen, M. Benayoun, *et al.*, "The anomalous magnetic moment of the muon in the Standard Model", *Physics Reports*, vol. 887, pp. 1–166, Dec. 2020. doi: 10.1016/j.physrep.2020.07.006 (cit. on p. 1).

[9] A. W. Chao and W. Chou, *Reviews of Accelerator Science and Technology, Volume 4: Accelerator Applications in Industry and the Environment*. WORLD SCIENTIFIC, Feb. 2012. doi: 10.1142/8380 (cit. on p. 1).

[10]   A. W. Chao and W. Chou, *Reviews of Accelerator Science and Technology, Volume 2: Medical Applications of Accelerators*. WORLD SCIENTIFIC, Dec. 2009. doi: 10.1142/7676 (cit. on p. 1).

[11]   R. Wideröe, "Über ein neues Prinzip zur Herstellung hoher Spannungen", *Archiv für Elektrotechnik*, vol. 21, no. 4, pp. 387–406, Jul. 1928. doi: 10.1007/BF01656341 (cit. on p. 1).

[12]   G. Ising, "Prinzip Einer Methode Zur Herstellung Von Kanalstrahlen Hoher Voltzahl", *Arkiv för matematik, astronomi och fysik*, vol. 18, no. 30, pp. 1–4, 1924 (cit. on p. 1).

[13]   E. O. Lawrence and M. S. Livingston, "The Production of High Speed Protons Without the Use of High Voltages", *Physical Review*, vol. 38, no. 4, pp. 834–834, Aug. 1931. doi: 10.1103/PhysRev.38.834 (cit. on p. 1).

[14]   D. W. Kerst and R. Serber, "Electronic Orbits in the Induction Accelerator", *Physical Review*, vol. 60, no. 1, pp. 53–58, Jul. 1941. doi: 10.1103/PhysRev.60.53 (cit. on p. 1).

[15]   D. W. Kerst, "The Acceleration of Electrons by Magnetic Induction", *Physical Review*, vol. 60, no. 1, pp. 47–53, Jul. 1941. doi: 10.1103/PhysRev.60.47 (cit. on p. 1).

[16]   P. Senger, "Astrophysics in the Laboratory—The CBM Experiment at FAIR", *Particles*, vol. 3, no. 2, pp. 320–335, Apr. 2020. doi: 10.3390/particles3020024 (cit. on pp. 1, 4).

[17]   P. Senger, "Probing dense QCD matter in the laboratory—The CBM experiment at FAIR", *Physica Scripta*, vol. 95, no. 7, p. 074 003, Jul. 2020. doi: 10.1088/1402-4896/ab8c14 (cit. on pp. 1, 4).

[18]   E. M. McMillan, "The Synchrotron—A Proposed High Energy Particle Accelerator", *Physical Review*, vol. 68, no. 5-6, pp. 143–144, Sep. 1945. doi: 10.1103/PhysRev.68.143 (cit. on p. 1).

[19]   E. D. Courant, M. S. Livingston, and H. S. Snyder, "The Strong-Focusing Synchroton—A New High Energy Accelerator", *Physical Review*, vol. 88, no. 5, pp. 1190–1196, Dec. 1952. doi: 10.1103/PhysRev.88.1190 (cit. on p. 1).

[20]   E. Courant and H. Snyder, "Theory of the alternating-gradient synchrotron", *Annals of Physics*, vol. 3, no. 1, pp. 1–48, Jan. 1958. doi: 10.1016/0003-4916(58)90012-5 (cit. on p. 1).

[21]   G. K. O'Neill, "Storage-Ring Synchrotron: Device for High-Energy Physics Research", *Physical Review*, vol. 102, no. 5, pp. 1418–1419, Jun. 1956. doi: 10.1103/PhysRev.102.1418 (cit. on p. 2).

[22]   D. W. Kerst, F. T. Cole, H. R. Crane, L. W. Jones, L. J. Laslett, T. Ohkawa, A. M. Sessler, K. R. Symon, K. M. Terwilliger, and N. V. Nilsen, "Attainment of Very High Energy by Means of Intersecting Beams of Particles", *Physical Review*, vol. 102, no. 2, pp. 590–591, Apr. 1956. doi: 10.1103/PhysRev.102.590 (cit. on p. 2).

[23]   V. Shiltsev and F. Zimmermann, "Modern and future colliders", *Reviews of Modern Physics*, vol. 93, no. 1, p. 015 006, Mar. 2021. doi: 10.1103/RevModPhys.93.015006 (cit. on p. 2).

[24]   M. Tigner, "A possible apparatus for electron clashing-beam experiments", *Il Nuovo Cimento*, vol. 37, no. 3, pp. 1228–1231, Jun. 1965. doi: 10.1007/BF02773204 (cit. on p. 2).

[25]   S. M. Gruner, D. Bilderback, I. Bazarov, K. Finkelstein, G. Krafft, L. Merminga, H. Padamsee, Q. Shen, C. Sinclair, and M. Tigner, "Energy recovery linacs as synchrotron radiation sources (invited)", *Review of Scientific Instruments*, vol. 73, no. 3, pp. 1402–1406, Mar. 2002. doi: 10.1063/1.1420754 (cit. on p. 2).

[26]   H. Motz, "Applications of the Radiation from Fast Electron Beams", *Journal of Applied Physics*, vol. 22, no. 5, pp. 527–535, May 1951. doi: 10.1063/1.1700002 (cit. on p. 2).

[27]   K. R. Symon, D. W. Kerst, L. W. Jones, L. J. Laslett, and K. M. Terwilliger, "Fixed-Field Alternating-Gradient Particle Accelerators", *Physical Review*, vol. 103, no. 6, pp. 1837–1859, Sep. 1956. doi: 10.1103/PhysRev.103.1837 (cit. on p. 2).

[28]   T. Ohkawa, "Two Beam Fixed Field Alternating Gradient Accelerator", *Review of Scientific Instruments*, vol. 29, no. 2, pp. 108–117, Feb. 1958. doi: 10.1063/1.1716114 (cit. on p. 2).

[29]   A. G. Ruggiero, "Brief History of FFAG Accelerators", Brookhaven National Laboratory, New York, Tech. Rep., 2006 (cit. on p. 2).

[30]   W. Barth, W. Bayer, L. Dahl, L. Groening, S. Richter, and S. Yaramyshev, "Upgrade program of the high current heavy ion UNILAC as an injector for FAIR", *Nuclear Instruments and Methods in Physics Research Section A: Accelerators, Spectrometers, Detectors and Associated Equipment*, vol. 577, no. 1-2, pp. 211–214, Jul. 2007. doi: 10.1016/j.nima.2007.02.054 (cit. on p. 2).

[31]   K. Blasche and B. Franczak, "The heavy ion synchrotron SIS", in *Proceedings of EPAC 1992*, 1992, pp. 9–13 (cit. on pp. 2, 4, 8).

[32]   P. Spiller, R. Balss, P. Bartolome, *et al.*, "The FAIR Heavy Ion Synchrotron SIS100", *Journal of Instrumentation*, vol. 15, no. 12, T12013–T12013, Dec. 2020. doi: 10.1088/1748-0221/15/12/T12013 (cit. on pp. 2, 4, 8).

[33]   "Facility for Antiproton and Ion Research in Europe GmbH." (2022), [Online]. Available: https://fair-center.eu/overview/accelerator%0A (cit. on p. 3).

[34] A. Oeftiger, O. Boine-Frankenheim, V. Chetvertkova, V. Kornilov, D. Rabusov, and S. Sorge, "Simulation study of the space charge limit in heavy-ion synchrotrons", *Physical Review Accelerators and Beams*, vol. 25, no. 5, p. 054 402, May 2022. doi: 10.1103/PhysRevAccelBeams.25.054402 (cit. on pp. 4, 5, 8, 41).

[35] O. Boine-Frankenheim and W. Stem, "Space charge compensation with pulsed electron lenses for intense ion beams in synchrotrons", *Nuclear Instruments and Methods in Physics Research Section A: Accelerators, Spectrometers, Detectors and Associated Equipment*, vol. 896, pp. 122–128, Jul. 2018. doi: 10.1016/j.nima.2018.04.014 (cit. on pp. 4, 5, 8, 47, 96).

[36] P. Spiller, M. Bai, J. Blaurock, *et al.*, "Status of the FAIR project", in *IPAC 2018 - 9th International Particle Accelerator Conference*, Vancouver, BC, Canada, 2018, pp. 63–68. doi: 10.18429/JACoW-IPAC2018-MOZGBF2 (cit. on pp. 4, 8).

[37] T. Stöhlker, V. Bagnoud, K. Blaum, *et al.*, "APPA at FAIR: From fundamental to applied research", *Nuclear Instruments and Methods in Physics Research Section B: Beam Interactions with Materials and Atoms*, vol. 365, pp. 680–685, Dec. 2015. doi: 10.1016/j.nimb.2015.07.077 (cit. on p. 4).

[38] T. Stöhlker, H. F. Beyer, A. Bräuning-Demian, *et al.*, "SPARC: The Stored Particle Atomic Research Collaboration At FAIR", in *AIP Conference Proceedings*, vol. 1336, 2011, pp. 132–137. doi: 10.1063/1.3586073 (cit. on p. 4).

[39] A. Herlert, "NUSTAR – The teenage years", *Hyperfine Interactions*, vol. 238, no. 1, p. 35, Nov. 2017. doi: 10.1007/s10751-017-1411-0 (cit. on p. 4).

[40] A. Belias, "FAIR status and the PANDA experiment", *Journal of Instrumentation*, vol. 15, no. 10, pp. C10001–C10001, Oct. 2020. doi: 10.1088/1748-0221/15/10/C10001 (cit. on p. 4).

[41] A. Bracco, "The NuPECC Long Range Plan 2017: Perspectives in Nuclear Physics", *Nuclear Physics News*, vol. 27, no. 3, pp. 3–4, Jul. 2017. doi: 10.1080/10619127.2017.1352311 (cit. on p. 4).

[42] E. Métral, T. Argyropoulos, H. Bartosik, *et al.*, "Beam Instabilities in Hadron Synchrotrons", *IEEE Transactions on Nuclear Science*, vol. 63, no. 2, pp. 1001–1050, Apr. 2016. doi: 10.1109/TNS.2015.2513752 (cit. on pp. 4, 32, 86).

[43] K. Y. Ng, *Physics of intensity dependent beam instabilities*. WORLD SCIENTIFIC, Dec. 2005, pp. 1–776. doi: 10.1142/5835 (cit. on pp. 4, 5, 13, 29, 31, 35, 38, 63, 65).

[44] F. J. Sacherer, "Methods for computing bunched beam instabilities", CERN, Geneva, Tech. Rep., 1972 (cit. on pp. 5, 72).

[45] I. Hofmann, *Space Charge Physics for Particle Accelerators* (Particle Acceleration and Detection). Cham: Springer International Publishing, 2017. doi: 10.1007/978-3-319-62157-9 (cit. on p. 5).

[46] A. V. Fedotov and I. Hofmann, "Half-integer resonance crossing in high-intensity rings", *Physical Review Special Topics - Accelerators and Beams*, vol. 5, no. 2, p. 024 202, Feb. 2002. doi: 10.1103/PhysRevSTAB.5.024202 (cit. on p. 5).

[47] F. J. Sacherer, "Bunch lengthening and microwave instability", *IEEE Transactions on Nuclear Science*, 1977. doi: 10.1109/TNS.1977.4328955 (cit. on p. 5).

[48] F. Zimmermann, "Review of single bunch instabilities driven by an electron cloud", *Physical Review Special Topics - Accelerators and Beams*, vol. 7, no. 12, p. 124 801, Dec. 2004. doi: 10.1103/PhysRevSTAB.7.124801 (cit. on pp. 5, 63).

[49] E. Mustafin, O. Boine-Frankenheim, I. Hofmann, H. Reich-Sprenger, and P. Spiller, "A theory of the beam loss-induced vacuum instability applied to the heavy-ion synchrotron SIS18", *Nuclear Instruments and Methods in Physics Research Section A: Accelerators, Spectrometers, Detectors and Associated Equipment*, vol. 510, no. 3, pp. 199–205, Sep. 2003. doi: 10.1016/S0168-9002(03)01811-4 (cit. on p. 5).

[50] V. Kornilov, A. Oeftiger, O. Boine-Frankenheim, V. Chetvertkova, S. Sorge, and P. Spiller, "Beam quality and beam loss predictions with space charge for SIS100", *Journal of Instrumentation*, vol. 15, no. 7, P07020–P07020, Jul. 2020. doi: 10.1088/1748-0221/15/07/P07020 (cit. on p. 5).

[51] D. Rabusov, A. Oeftiger, and O. Boine-Frankenheim, "Characterization and minimization of the half-integer stop band with space charge in a hadron synchrotron", *Nuclear Instruments and Methods in Physics Research Section A: Accelerators, Spectrometers, Detectors and Associated Equipment*, vol. 1040, p. 167 290, Oct. 2022. doi: 10.1016/j.nima.2022.167290 (cit. on pp. 5, 41).

[52] V. Kornilov and O. Boine-Frankenheim, "Intensity thresholds for transverse coherent instabilities during proton and heavy-ion operation in SIS100", *IPAC 2012 - International Particle Accelerator Conference 2012*, vol. 100, no. 2, pp. 2934–2936, 2012 (cit. on pp. 6, 8, 96).

[53] V. Kornilov, "SIS100 high-intensity beam dynamics", in *20th FAIR Machine Advisory Committee Meeting*, Darmstadt, 2018 (cit. on p. 6).

[54] V. Kornilov, "SIS100 beam dynamics and transverse feedback system", in *21st FAIR Machine Advisory Committee Meeting*, Darmstadt, May 2019 (cit. on p. 6).

[55] V. Kornilov, O. Boine-Frankenheim, and I. Hofmann, "Transverse Collective Instabilities in SIS 100", GSI Helmholtzzentrum, Darmstadt, Tech. Rep., Jun. 2008 (cit. on p. 6).

[56] V. Kornilov, "Coupling Impedances in SIS100", GSI Helmholtzzentrum, Darmstadt, Tech. Rep. 4, Feb. 2015, pp. 1–12 (cit. on p. 6).

Bibliography   **115**

[57] V. Kornilov, O. Boine-Frankenheim, and V. Kapin, "Coherent instability thresholds and dynamic aperture with octupoles and nonlinear space-charge in the SIS100 Synchrotron", in *IPAC 2010 - 1st International Particle Accelerator Conference*, 2010, pp. 1988–1990 (cit. on pp. 6, 8, 9).

[58] L. Landau, "On the vibrations of the electronic plasma", in *Collected Papers of L.D. Landau*, vol. 10, Elsevier, 1965, pp. 445–460. doi: 10.1016/B978-0-08-010586-4.50066-3 (cit. on pp. 6, 8, 37).

[59] S. Artikova, O. Boine-Frankenheim, O. Meusel, A. Oeftiger, D. Ondreka, K. Schulte-Urlichs, and P. Spiller, "Pulsed electron lenses for space charge compensation in the FAIR synchrotrons", *Journal of Instrumentation*, vol. 16, no. 03, P03044, Mar. 2021. doi: 10.1088/1748-0221/16/03/P03044 (cit. on pp. 7, 8, 47).

[60] E. Tsyganov, A. Taratin, and A. Zinchenko, "Compensation of space charge effect at beam-beam interactions in proton-proton colliders", State University of New York, New York, Tech. Rep., 1996 (cit. on p. 8).

[61] V. Shiltsev and D. Finley, "Electron compression of beam-beam footprint in the Tevatron", Fermi National Accelerator Laboratory (FNAL), Batavia, IL, Tech. Rep. August, Aug. 1997, pp. 1–10. doi: 10.2172/622560 (cit. on p. 8).

[62] V. Shiltsev, ""Electron Lens" to Compensate Bunch-to-Bunch Tune Spread in TEV33", Fermi National Accelerator Laboratory (FNAL), Batavia, IL, Tech. Rep. August, Oct. 1997, pp. 1–10. doi: 10.2172/575151 (cit. on p. 8).

[63] V. Shiltsev, V. Danilov, D. Finley, and A. Sery, "Considerations on compensation of beam-beam effects in the Tevatron with electron beams", *Physical Review Special Topics - Accelerators and Beams*, vol. 2, no. 7, p. 071001, Jul. 1999. doi: 10.1103/PhysRevSTAB.2.071001 (cit. on p. 8).

[64] V. Shiltsev, K. Bishofberger, V. Kamerdzhiev, *et al.*, "Tevatron electron lenses: Design and operation", *Physical Review Special Topics - Accelerators and Beams*, vol. 11, no. 10, p. 103501, Oct. 2008. doi: 10.1103/PhysRevSTAB.11.103501 (cit. on p. 8).

[65] V. Shiltsev, Y. Alexahin, K. Bishofberger, V. Kamerdzhiev, V. Parkhomchuk, V. Reva, N. Solyak, D. Wildman, X.-L. Zhang, and F. Zimmermann, "Experimental studies of compensation of beam–beam effects with Tevatron electron lenses", *New Journal of Physics*, vol. 10, no. 4, p. 043042, Apr. 2008. doi: 10.1088/1367-2630/10/4/043042 (cit. on p. 8).

[66] W. Fischer, X. Gu, Z. Altinbas, *et al.*, "Operational Head-on Beam-Beam Compensation with Electron Lenses in the Relativistic Heavy Ion Collider", *Physical Review Letters*, vol. 115, no. 26, p. 264801, Dec. 2015. doi: 10.1103/PhysRevLett.115.264801 (cit. on p. 8).

[67] G. Stancari, A. Valishev, G. Annala, G. Kuznetsov, V. Shiltsev, D. A. Still, and L. G. Vorobiev, "Collimation with Hollow Electron Beams", *Physical Review Letters*, vol. 107, no. 8, p. 084 802, Aug. 2011. doi: 10.1103/PhysRevLett.107.084802 (cit. on p. 8).

[68] A. Burov, G. Foster, and V. Shiltsev, "Space-charge compensation in proton boosters", in *PACS2001. Proceedings of the 2001 Particle Accelerator Conference (Cat. No.01CH37268)*, vol. 4, IEEE, 2001, pp. 2896–2898. doi: 10.1109/PAC.2001.987947 (cit. on p. 8).

[69] X. Buffat, D. Amorim, S. Antipov, G. Arduini, and N. Biancacci, "Transverse Instabilities", in *9th LHC Operations Evian Workshop*, 2019, pp. 233–243 (cit. on p. 8).

[70] E. Métral, "General mitigation techniques for coherent beam instabilities in particle accelerators", *The European Physical Journal Plus*, vol. 123, pp. 1–23, 2022. doi: 10.1140/epjp/s13360-021-02264-4 (cit. on pp. 8, 36).

[71] M. Schenk, A. Grudiev, K. Li, and K. Papke, "Analysis of transverse beam stabilization with radio frequency quadrupoles", *Physical Review Accelerators and Beams*, vol. 20, no. 10, p. 104 402, Oct. 2017. doi: 10.1103/PhysRevAccelBeams.20.104402 (cit. on pp. 8, 9, 41, 78, 95).

[72] M. Schenk, X. Buffat, K. Li, and A. Maillard, "Vlasov description of the effects of nonlinear chromaticity on transverse coherent beam instabilities", *Physical Review Accelerators and Beams*, vol. 21, no. 8, p. 084 402, Aug. 2018. doi: 10.1103/PhysRevAccelBeams.21.084402 (cit. on pp. 8, 9, 41, 65, 67, 68, 71, 72, 74, 76, 95, 96).

[73] A. Burov, "Nested head-tail Vlasov solver", *Physical Review Special Topics - Accelerators and Beams*, vol. 17, no. 2, p. 021 007, Feb. 2014. doi: 10.1103/PhysRevSTAB.17.021007 (cit. on pp. 8, 73, 75).

[74] D. Möhl, "On Landau damping of dipole modes by non-linear space charge and octupoles", *Part. Accel.*, vol. 50, no. CERN-PS-95-08-DI, pp. 177–187, 1995 (cit. on p. 8).

[75] J. Scott Berg and F. Ruggiero, "Stability diagrams for Landau damping", in *Proceedings of the 1997 Particle Accelerator Conference (Cat. No.97CH36167)*, vol. 2, IEEE, 1998, pp. 1712–1714. doi: 10.1109/PAC.1997.750810 (cit. on pp. 8, 9, 72, 74, 96).

[76] A. Grudiev, "Radio frequency quadrupole for Landau damping in accelerators", *Physical Review Special Topics - Accelerators and Beams*, vol. 17, no. 1, p. 011 001, Jan. 2014. doi: 10.1103/PhysRevSTAB.17.011001 (cit. on pp. 8, 9, 96).

[77] V. Shiltsev, Y. Alexahin, A. Burov, and A. Valishev, "Landau Damping of Beam Instabilities by Electron Lenses", *Physical Review Letters*, vol. 119, no. 13, p. 134 802, Sep. 2017. doi: `10.1103/PhysRevLett.119.134802` (cit. on pp. 8, 9, 44, 78).

[78] J. Gareyte, J.-P. Koutchouk, and F. Ruggiero, "Landau damping dynamic aperture and octupole in LHC", CERN, Geneva, Tech. Rep. April 1997, 1997 (cit. on pp. 8, 9, 18).

[79] D. Astapovych, O. Boine-Frankenheim, V. Gubaidulin, V. Kornilov, U. Niedermayer, and D. Schulte, "Stability limits with Landau damping in the FCC-hh", *Journal of Instrumentation*, vol. 16, no. 01, P01013–P01013, Jan. 2021. doi: `10.1088/1748-0221/16/01/P01013` (cit. on pp. 8, 9, 75, 79, 86).

[80] M. Schenk, X. Buffat, L. R. Carver, R. De Maria, K. Li, and E. Métral, "Experimental stabilization of transverse collective instabilities in the LHC with second order chromaticity", *Physical Review Accelerators and Beams*, vol. 21, no. 8, p. 084 401, Aug. 2018. doi: `10.1103/PhysRevAccelBeams.21.084401` (cit. on pp. 9, 41).

[81] V. Kornilov and O. Boine-Frankenheim, "Landau damping due to octupoles of non-rigid head–tail modes", *Nuclear Instruments and Methods in Physics Research, Section A: Accelerators, Spectrometers, Detectors and Associated Equipment*, vol. 951, p. 163 042, 2020. doi: `10.1016/j.nima.2019.163042` (cit. on p. 10).

[82] M. Karliner and K. Popov, "Theory of a feedback to cure transverse mode coupling instability", *Nuclear Instruments and Methods in Physics Research, Section A: Accelerators, Spectrometers, Detectors and Associated Equipment*, vol. 537, no. 3, pp. 481–500, 2005. doi: `10.1016/j.nima.2004.08.068` (cit. on pp. 10, 36).

[83] N. Mounet, "The LHC Transverse Coupled-Bunch Instability", Ph.D. dissertation, EPFL, 2012, p. 226 (cit. on pp. 10, 18, 41, 42).

[84] E. Métral, "Imaginary tune split and repulsion single-bunch instability mechanism in the presence of a resistive transverse damper and its mitigation", *Physical Review Accelerators and Beams*, vol. 24, no. 4, p. 041 003, Apr. 2021. doi: `10.1103/PhysRevAccelBeams.24.041003` (cit. on p. 10).

[85] S. A. Antipov, D. Amorim, N. Biancacci, X. Buffat, E. Métral, N. Mounet, A. Oeftiger, and D. Valuch, "Proof-of-Principle Direct Measurement of Landau Damping Strength at the Large Hadron Collider with an Antidamper", *Physical Review Letters*, vol. 126, no. 16, p. 164 801, Apr. 2021. doi: `10.1103/PhysRevLett.126.164801` (cit. on pp. 11, 75).

[86] V. Kornilov, O. Boine-Frankenheim, and I. Hofmann, "Stability of transverse dipole modes in coasting ion beams with nonlinear space charge, octupoles, and chromaticity", *Physical Review Special Topics - Accelerators and Beams*, vol. 11, no. 1, p. 014 201, 2008. doi: 10.1103/PhysRevSTAB.11.014201 (cit. on p. 11).

[87] O. Boine-Frankenheim and O. Chorniy, "Stability of coherent synchrotron oscillations with space charge", *Physical Review Special Topics - Accelerators and Beams*, vol. 10, no. 10, p. 104 202, Oct. 2007. doi: 10.1103/PhysRevSTAB.10.104202 (cit. on p. 11).

[88] H. Wiedemann, *Particle Accelerator Physics* (Graduate Texts in Physics 4). Cham: Springer International Publishing, Jul. 2015, vol. 7. doi: 10.1007/978-3-319-18317-6 (cit. on pp. 13, 26).

[89] S.-Y. Lee, *Accelerator physics*. Singapore: World Scientific Publishing Co., 1999, p. 491 (cit. on p. 13).

[90] A. Wolski, *Beam Dynamics in High Energy Particle Accelerators*. Imperial College Press, 2014 (cit. on p. 13).

[91] A. W. Chao, K. H. Mess, M. Tigner, and F. Zimmermann, *Handbook of Accelerator Physics and Engineering*. WORLD SCIENTIFIC, May 2013, p. 847. doi: 10.1142/8543 (cit. on p. 13).

[92] A. W. Chao, *Physics of Collective Beam Instabilities in High Energy Accelerators*, M. Month, Ed. New York: John Wiley & Sons, Inc. All, 2000 (cit. on pp. 13, 29–31, 35, 38, 65–67, 70, 71).

[93] N. Mounet, "Landau damping in the transverse plane", CERN, Tech. Rep. 9, 2020, pp. 45–53. doi: https://doi.org/10.23732/CYRCP-2020-009.45 (cit. on pp. 30, 41, 65).

[94] J. H. Malmberg and C. B. Wharton, "Collisionless Damping of Electrostatic Plasma Waves", *Physical Review Letters*, vol. 13, no. 6, pp. 184–186, Aug. 1964. doi: 10.1103/PhysRevLett.13.184 (cit. on p. 37).

[95] V. K. Neil and A. M. Sessler, "Longitudinal Resistive Instabilities of Intense Coasting Beams in Particle Accelerators", *Review of Scientific Instruments*, vol. 36, no. 4, pp. 429–436, Apr. 1965. doi: 10.1063/1.1719594 (cit. on p. 38).

[96] L. J. Laslett, V. K. Neil, and A. M. Sessler, "Transverse Resistive Instabilities of Intense Coasting Beams in Particle Accelerators", *Review of Scientific Instruments*, vol. 36, no. 4, pp. 436–448, Apr. 1965. doi: 10.1063/1.1719595 (cit. on p. 38).

[97] E. D. Courant and A. M. Sessler, "Transverse Coherent Resistive Instabilities of Azimuthally Bunched Beams in Particle Accelerators", *Review of Scientific Instruments*, vol. 37, no. 11, pp. 1579–1588, Nov. 1966. doi: 10.1063/1.1720048 (cit. on p. 38).

[98] A. Oeftiger, "An Overview of PyHEADTAIL", CERN, Geneva, Tech. Rep. CERN-ACC-NOTE-2019-0013, Apr. 2019 (cit. on pp. 41, 76).

[99] G. Rumolo and F. Zimmermann, "Practical User Guide for HEADTAIL", CERN, Geneva, Tech. Rep., 2002, p. 31 (cit. on p. 41).

[100] I. Hofmann, A. Oeftiger, and O. Boine-Frankenheim, "Self-consistent long-term dynamics of space charge driven resonances in 2D and 3D", *Physical Review Accelerators and Beams*, vol. 24, no. 2, p. 024 201, Feb. 2021. doi: 10.1103/PhysRevAccelBeams.24.024201 (cit. on p. 41).

[101] N. Biancacci, E. Métral, and M. Migliorati, "Fast-slow mode coupling instability for coasting beams in the presence of detuning impedance", *Physical Review Accelerators and Beams*, vol. 23, no. 12, pp. 1–7, 2020. doi: 10.1103/PhysRevAccelBeams.23.124402 (cit. on p. 41).

[102] X. Buffat, "Transverse beams stability studies at the Large Hadron Collider", Ph.D. dissertation, EPFL, 2015 (cit. on p. 41).

[103] M. Bassetti and G. A. Erskine, "Closed Expression for the Electrical Field of a 2D Gaussian Charge", CERN, Tech. Rep., 1980, p. 6 (cit. on p. 44).

[104] M. A. Furman, "Compact Complex Expressions for the Electric Field of 2-D Elliptical Charge", *American Journal of Physics*, 1994 (cit. on p. 44).

[105] V. Kornilov and O. Boine-Frankenheim, "Transverse Instability of Coasting Beam in SIS18", GSI Helmholtzzentrum, Darmstadt, Tech. Rep., Dec. 2009 (cit. on pp. 47, 57–59, 61, 62).

[106] "SIS18 lattice". (2022), [Online]. Available: https://www.gsi.de/en/work/accelerator_operations/accelerators/heavy_ion_synchrotron_sis18/sis18_sections (cit. on p. 48).

[107] V. D. Shiltsev, *Electron Lenses for Super-Colliders* (Particle Acceleration and Detection). New York, NY: Springer New York, 2016, pp. 163–181. doi: 10.1007/978-1-4939-3317-4 (cit. on p. 50).

[108] M. Blaskiewicz, "Implications of the PSR Instability for the SNS", in *European Particle Accelerator Conference*, Vienna: JACoW, Jun. 2000, pp. 1110–1112 (cit. on p. 63).

[109] M. Blaskiewicz, "The fast loss electron proton instability", in *AIP Conference proceedings*, New York, 1999, pp. 321–330. doi: 10.1063/1.1303089 (cit. on p. 63).

[110] D. Neuffer, E. Colton, D. Fitzgerald, T. Hardek, R. Hutson, R. Macek, M. Plum, H. Thiessen, and T.-S. Wang, "Observations of a fast transverse instability in the PSR", *Nuclear Instruments and Methods in Physics Research Section A: Accelerators, Spectrometers, Detectors and Associated Equipment*, vol. 321, no. 1-2, pp. 1–12, Sep. 1992. doi: 10.1016/0168-9002(92)90371-A (cit. on p. 63).

[111] V. Gubaidulin, V. Kornilov, O. Boine-Frankenheim, and E. Métral, "Landau damping of transverse head-tail instabilities with a pulsed electron lens in hadron synchrotrons", *Physical Review Accelerators and Beams*, vol. 25, no. 8, p. 084 401, Aug. 2022. doi: 10.1103/PhysRevAccelBeams.25.084401 (cit. on pp. 65, 75, 85).

[112] M. Blaskiewicz and V. H. Ranjbar, "Transverse Beam Transfer Functions Via the Vlasov Equation", in *Proceedings of PAC2013*, Pasadena, 2013, pp. 2–4 (cit. on p. 67).

[113] F. W. J. Olver, A. B. Olde Daalhuis, D. W. Lozier, B. I. Schneider, R. F. Boisvert, C. W. Clark, B. R. Miller, B. V. Saunders, H. S. Cohl, and M. A. McClain. "Digital Library of Mathematical Functions". (2021), [Online]. Available: http://dlmf.nist.gov/ (cit. on pp. 71, 72).

[114] J. Laclare, "CERN Accelerator School: Advanced Accelerator Physics", CERN, Geneva, Tech. Rep., 1987, pp. 264–325 (cit. on p. 72).

[115] E. Métral and M. Migliorati, "Longitudinal and transverse mode coupling instability: Vlasov solvers and tracking codes", *Physical Review Accelerators and Beams*, vol. 23, no. 7, p. 071 001, Jul. 2020. doi: 10.1103/PhysRevAccelBeams.23.071001 (cit. on p. 73).

[116] Y. Alexahin, A. Burov, and V. Shiltsev, "Landau Damping with Electron Lenses in Space-Charge Dominated Beams", *Journal of Instrumentation*, vol. 16, no. 03, P03046, Mar. 2021. doi: 10.1088/1748-0221/16/03/P03046 (cit. on p. 96).